Inclusions, Porosity, and Fatigue of AlSi10Mg Parts Produced by Selective Laser Melting

Submitted in partial fulfillment of the requirements for

the degree of

Doctor of Philosophy

in

Materials Science and Engineering

Ming Tang

B.S., Materials Science and Engineering, Beihang University
M.S., Materials Science and Engineering, Carnegie Mellon University

Carnegie Mellon University
Pittsburgh, PA

April 2017

Acknowledgements

I feel extremely fortunate to have the opportunity to pursue my Ph.D. education in the Department of Materials Science and Engineering at Carnegie Mellon University. I could have never been so close to the degree without help and support from many people throughout my 5-year joyful journey in Pittsburgh.

First and foremost, I would like to thank my advisor, Professor P. Chris Pistorius, for always being a shining example of his dedication to work, continuous optimism, care for the students, and an amazing sense of humor. I am forever grateful to him for shaping me with a critical thinking attitude, as well as offering freedom and flexibility on the research direction, which enables me being self-motivated all the time. Furthermore, it is really enjoyable for me to attend the annual New Year party in Pistorius' house, which makes me feel very much welcomed in this country. It is a truly amazing privilege to learn from him at this early stage of my career and life.

I would like to extend my gratitude to the committee members, Professor Anthony D. Rollett, Professor Bryan Webler, and Dr. Cagatay Yanar (from Arconic) for their insightful comments and valuable suggestions, which remarkably improved my thesis work. I will always remember the critical comments from Professor Rollett on my 100-page overview document, as well as his willingness to provide time and suggestions for discussion, considering how busy he is. I also need to thank Professor Webler for his guidance and comments on the mechanical tests, and valuable support for using Thermo-Calc. I am grateful for the numerous forms of support received from Dr. Cagatay Yanar, including valuable suggestions, prompt sample builds, and many helpful tests. I appreciate the funding support from RAMP (Research for Advanced Manufacturing in Pennsylvania program) for this project.

I must also thank the industrial partners at Arconic, who provide numerous suggestions and practical perspectives. I sincerely appreciate John Siemon, Jaakko Suni, and Robert Speer, for helpful suggestions and encouragement during the monthly meeting. Polishing a soft metal like aluminum is not easy, and I greatly appreciate Alexis Pleva for showing us around in the metallography lab at Arconic and offering most helpful and practical suggestions. Also special thanks to David Heard, Jason Brem, and Gongyao Wang, for their plentiful help with mechanical experiments, particularly time-consuming fatigue tests during the RAMP project.

Pistorius' group has always been a fun and pleasant place to work in, with a lot of laugher and great memories. I am grateful for all the past and current members: Hyeon Jeong Cho, Wen Li, Jia Tan, Megha Jampani, Jorge Gibson, Karina Assis, Farzin Fatollahi-Fard, Dai Tang, Stephano Papadopoli Tonelli Piva, Mauro Elias Ferreira, Deepoo Kumar, Abhishek Bhansali, David Gildemeister, Xuewei Lyu, Jie Dang, and Yining He. Thank you all for your willingness to share your expertise and happy time we had together in Pittsburgh!

I owe many thanks to the world-class MSE staff at CMU, and your kindness makes my stay wonderful. I would like to sincerely thank Roxann Martin Eckman for providing me with a good environment and facilities to complete this thesis work. I also want to thank Bill Pingitore, you are so knowledgeable and always being nice, and thank you for your kind help on many specific but important experimental work. I would like to also acknowledge Jeanna Pekarcik, Suzy Smith, Kelly Rockenstein, and Angela Pusateri for being so patient every time I walked into your offices with various questions. I also need to thank Adam Wise and Tom Nuhfer for their help regarding characterization tests. I owe special thanks to Larry Hayhurst at the machine shop who always did a fantastic work regarding various sample requirements and helped a lot on my research progress. I need to acknowledge Professor Jack Beuth in the Department of Mechanical Engineering for his insightful suggestions on the work of porosity prediction, Ross Cunningham and Samikshya Subedi for their valuable help on 3D reconstruction, Dai Tang for plentiful guidance on automatic feature analysis by SEM, and David Sapiro for his kind help with tension and compression tests. I acknowledge use of the Materials Characterization Facility at Carnegie Mellon University supported by Grant MCF-677785.

Although no words in the world can ever fully express it, I must give my deep and sincere gratitude to my parents and grandparents, currently on the other side of the globe. Without your unconditional love and support, I would not be where I am today. Last but not least, I would also like to thank my wife, Qinyuan Liu, for always being understanding and encouraging through the best and worst of times.

Abstract

Additive manufacturing (AM) has experienced remarkable growth in the past decade with applications in both rapid prototyping and rapid manufacturing for functional end-usable parts. As one of the most promising AM processes, selective laser melting (SLM) can be used to fabricate metal products line by line and layer upon layer within a powder bed system. Such process allows the building of parts with customized shapes, which brings higher design flexibility than traditional casting and wrought manufacturing. In this work, AlSi10Mg powder is chosen as the raw material for producing parts by SLM, since aluminum alloys are widely used in automotive and aerospace industries thanks to an excellent combination of low density and competitive mechanical properties.

However, there remain multiple drawbacks which limit further applications of aluminum parts produced by SLM: lack of prediction of solidification microstructure, few studies on fatigue properties, and cost and time caused by the limited production rate. All these issues were studied in this work and summarized as follows:

Rapid movement of the melt pool (at a speed around 1 m/s) in SLM of metal powder directly implies rapid solidification. In this research, the length scale of the as-built microstructure of parts built with the alloy AlSi10Mg was measured and compared with the well-known relationship between cell size and cooling rate. Cooling rates during solidification were estimated using the Rosenthal equation. It was found that the solidification structure is the expected cellular combination of silicon with α-aluminum. The dependence of the measured cell spacing on the calculated cooling rate follows the well-established relationship for aluminum alloys. The implication is that cell spacing can be manipulated by changing the heat input. Microscopy of polished sections through particles of the metal powder used to build the parts showed that the particles have a dendritic-eutectic structure; the dendrite arm spacings in metal powder particles of different diameters were measured and also agree with literature correlations, showing the expected increase in secondary dendrite arm spacing with increasing particle diameter.

It is well-known that the fatigue behavior of cast aluminum alloy parts is largely determined by the internal defects, particularly pores and inclusions, such as oxides. This study shows that such imperfections are also present in AlSi10Mg parts produced by SLM, and serve as sites for failure initiation. The effect of hatch spacing and building orientation on tensile and fatigue

properties was tested. Similar defects were found both on polished cross-sections and on fracture surfaces. The results imply that the oxide-driven pores dominate the fatigue resistance of the samples in this work. The larger oxide particles which are associated with the crack initiation likely form by oxidation of metal vapor during part manufacture.

Residual porosity in parts produced by SLM mainly results from lack-of-fusion, entrapped gas, pores left in powder, evaporation of elements, and collapse of key-holes. Lack-of-fusion porosity is caused by the the insufficient overlap of melt pools in powder bed fusion and is particularly detrimental to fatigue performance due to the stress concentration at the sharp edges of the pores. The third part of this work deals with predicting lack-of-fusion porosity quantitatively by a geometrically-based model and designing processing parameters for build rate improvement without introducing porosity. The inputs into the simulation are hatch spacing, layer thickness, melt-pool cross-sectional area, and hatch rotation angle. Comparison with several data sets from the literature shows that the simulations correctly predict process conditions at which lack-of-fusion porosity becomes apparent, as well as the rate at which porosity increases with changes in process conditions such as beam speed, layer thickness, and hatch spacing. Relative to the default processing parameters provided by the manufacturer, the build rate can be improved by adjusting hatch spacing and layer thickness, and increasing the platform temperature. The simulations also show that the volume fraction of lack-of-fusion porosity is independent of hatch rotation angle. A unique combination of zero rotation and half hatch spacing as the beam offset between adjacent layers is proposed for build rate optimization.

Table of content

List of Tables

List of Figures

List of Symbols

Symbol	Description of Symbols
Rosenthal equation	
P	total beam power
Q	power absorbed by the part
η	absorptivity, given by Q/P
V	beam travel velocity
T	local temperature
T_0	plate/preheating temperature
ξ	distance from the beam position along the travel direction
r	radial distance from the beam position
ρ	density
C	heat capacity
k	thermal conductivity
α	thermal diffusivity, given by $k/\rho C$
Solidification concepts	
C_0	average solute composition in the alloy
C_s	composition in the solid at the solidification front
C_L	composition in the liquid at the solidification front
k	partition coefficient ($k=C_S/C_L$)
f_s	mass fraction of solid phase
G	thermal gradient
R	growth rate
λ	cell size (during cellular growth)
λ_1 or DAS	primary dendrite arm spacing
λ_2 or $SDAS$	secondary dendrite arm spacing
$\dot{T}$	local cooling rate
$T_{solidus}$	solidus temperature

$T_{liquidus}$	liquidus temperature
$D_{particle}$	diameter of powder particles

Melt-pool dimensions

W	melt-pool width
D	melt-pool depth
L_{total}	melt-pool length
R	cap height
L^*	depth of the overlap between adjacent melt pools
A	cross-sectional melt-pool area perpendicular to laser scan direction

Deposition parameters

H	hatch spacing
L	layer thickness
θ	hatch rotation angle
BO	beam offset
ε	unmelted volume fraction of an as-built part
ρ_{part}	predicted density of an as-built part
ρ_{true}	true density of full dense material
n_{melt}	number of times each volume in the part is melted

Mechanical properties

R_p or YS	yield strength
R_m or UTS	tensile strength
e_f	tensile elongation
σ_a	stress amplitude
σ_{min}	minimum stress
σ_{max}	maximum stress
R_{stress}	stress ratio ($=\sigma_{min}/\sigma_{max}$)
QI	quality index

n	work-hardening exponent
θ	work-hardening rate
ε_p	true plastic strain

1 Introduction

1.1 Selective laser melting

Over the past decade, 3D printing, also known as additive manufacturing (AM), has attracted increasing interest and been widely studied in both academia and industry. Much work has been performed on AM technology with published outcomes including ISO and ASTM standards [1]–[5], review papers [6]–[13], books [14]–[16], special AM journal issues [17] and roadmap reports [18]–[22]. Compared to the conventional manufacturing methods, AM offers the advantages of customized geometry without wasting materials or increasing cost.

Among all metal AM techniques, selective laser melting (SLM) is most commonly used, and can be applied across all application ranges, from 3D prototype to low volume industrial production. In SLM, a thin layer of metal powder is distributed on a platform and selectively fused by a moving laser beam in an inert gas atmosphere. After scanning one layer, the platform is lowered by one layer thickness and another layer of powder is spread on the previously solidified top surface. This coating-melting and layer-upon-layer deposition process is repeated to build a solid three-dimensional component. Figure 1 graphically shows a front view of main components inside an SLM machine. Figure 2 demonstrates detailed (but schematic) view of melt-pool movement when building AlSi10Mg alloy parts by an EOS M280 metal printer, as studied in this work. The black lines represent the melt-pool fusion boundaries with size and shape calculated by the Rosenthal equation [23][1] based on the processing parameters in Table 1. As illustrated in Figure 2, hatch spacing is the lateral distance between adjacent laser tracks in the same layer, and layer thickness is the vertical movement of the substrate after selectively fusing one powder layer.

[1] The principles and limitations of the Rosenthal equation are discussed later.

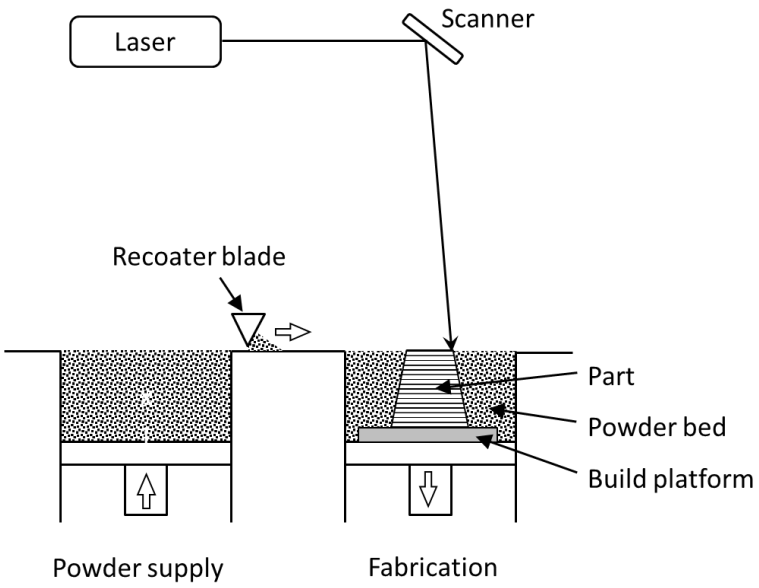

Figure 1. Schematic of SLM process and main components inside an SLM machine. Adapted from Frazier [7].

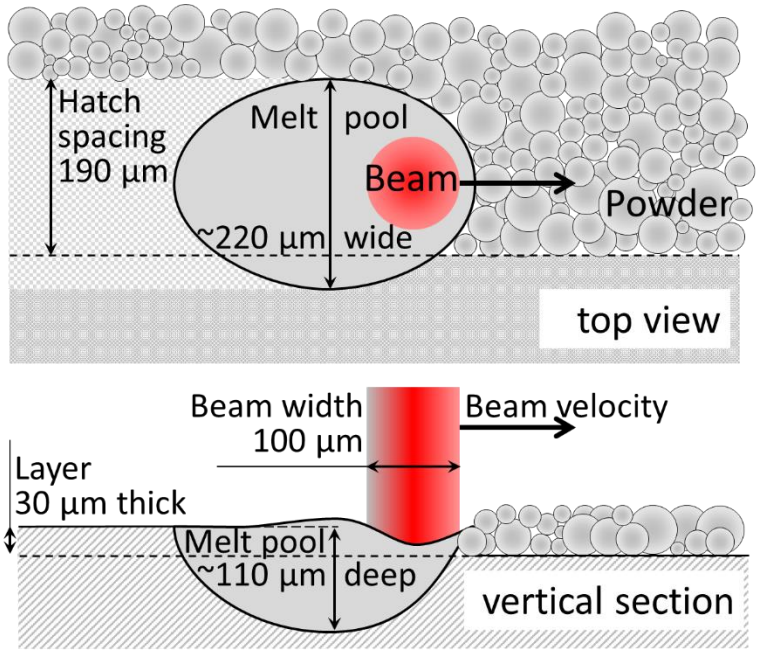

Figure 2. Schematic of beam scanning in the powder bed system. Values refer to standard conditions for AlSi10Mg/EOS as studied in this project (see Table 1)

Table 1. Typical processing conditions for producing AlSi10Mg parts, using an EOS M280 laser sintering system

Laser Power	370 W
Laser scanning speed	1.3 m/s
Layer thickness	30 µm
Beam diameter	0.1 mm
Hatch spacing	0.19 mm

In order to test the feasibility and consistency of SLM machines in fabricating metal parts, multiple alloys have been used by other researchers in manufacturing, including TiAl6V4, IN718, 316 Stainless steel, and AlSi10Mg, to fabricate parts and test these for mechanical properties [7], [8]. The focus in this work is in particular on AlSi10Mg, with the chemical composition of unused powder and as-built component tested by ICP (inductively coupled plasma) analysis at Arconic Technology Center and shown in Table 2.

Compared to other alloy systems, aluminum alloys have a competitive combination of low density, high thermal conductivity, good mechanical properties and fluidity, and are consequently widely employed in automotive and aerospace industries [24]. Among all aluminum alloys, AlSi10Mg is selected based on its high fluidity, low shrinkage, good weldability and high corrosion resistance [25], [26]. The two major alloying elements in the alloy are silicon and magnesium. The 10wt% silicon provides high fluidity from the near-eutectic composition (see the Al-Si binary phase diagram in Figure 3). The smaller addition of magnesium is to introduce Mg_2Si for precipitation hardening, and more importantly in this study, to disrupt alumina oxide film by forming spinel ($MgAl_2O_4$) [27]. However, aluminum alloys also have disadvantageous properties for manufacturing by laser applications, mainly caused by high thermal conductivity, high reflectivity and oxides [28]. Although reflectivity was reported as a problem, the results of this work indicate that the laser absorptivity is in fact similar for aluminum alloys and other alloys used for SLM (as summarized in Table 13).

In this project, the AlSi10Mg powder was supplied by EOS and had been produced by inert gas atomization, which is a dominant method for producing metal and pre-alloyed powder. The powder composition is close to that of A360 casting aluminum alloy (9.5%Si, 0.5%Mg and Fe less than 1.5%) [26].

Table 2. Chemical compositions of AlSi10Mg powder provided by EOS and cylinder part built in this work.

Element	Weight percentage		
	Powder	Part	EOS datasheet [29]
Si	10.6	10.2	9.0-11.0
Mg	0.38	0.35	0.20-0.45
Fe	0.15	0.15	≤ 0.55
Ti	< 0.01	< 0.01	≤ 0.15
Zn	< 0.01	< 0.01	≤ 0.10
Mn	< 0.01	0.01	≤ 0.45
Cu	0.01	< 0.01	≤ 0.05
Al	balance	balance	balance

1.2 Rapid solidification

Rapid movement of the melt pool (at a speed around 1 m/s) in selective laser melting of metal powder directly implies rapid solidification, and hence yielding fine microstructures. Assessing phases and microstructure is important to control mechanical properties of parts produced by additive manufacturing, and hence was studied as part of this project.

1.2.1 Solidification range

Binary Al-Si alloy is first considered to give insights into solidification behavior. To predict the solidification temperature range, equilibrium conditions and Scheil solidification conditions are applied. The major difference between these two models is the assumption regarding the solid phases: infinite diffusivity for equilibrium solidification and no solid-state diffusion in the Scheil model. Solidification of an Al-10Si binary alloy is first considered, with main assumptions and equations summarized in Table 3, where C_0 is the average solute composition in the alloy (*i.e.* C_0 equals to 10% for Si in Al-10Si), C_s is the composition in the solid at the solidification front, k is the partition coefficient ($k=C_S/C_L$), and f_s is the mass fraction of the solid phase. Figure 3 shows the phase diagram for Al-10Si in the whole range and eutectic Al-rich range, which gives a temperature difference from liquidus to eutectic temperature around 18K.

Table 3. Major assumptions and equations used in analytical models

Model	Equilibrium (lever rule)	Scheil [30]
Solid diffusion	complete	no
Liquid diffusion	complete	complete
Equation	$C_S = kC_0/[(1-f_S)+kf_S]$	$C_S = kC_0(1-f_S)^{k-1}$

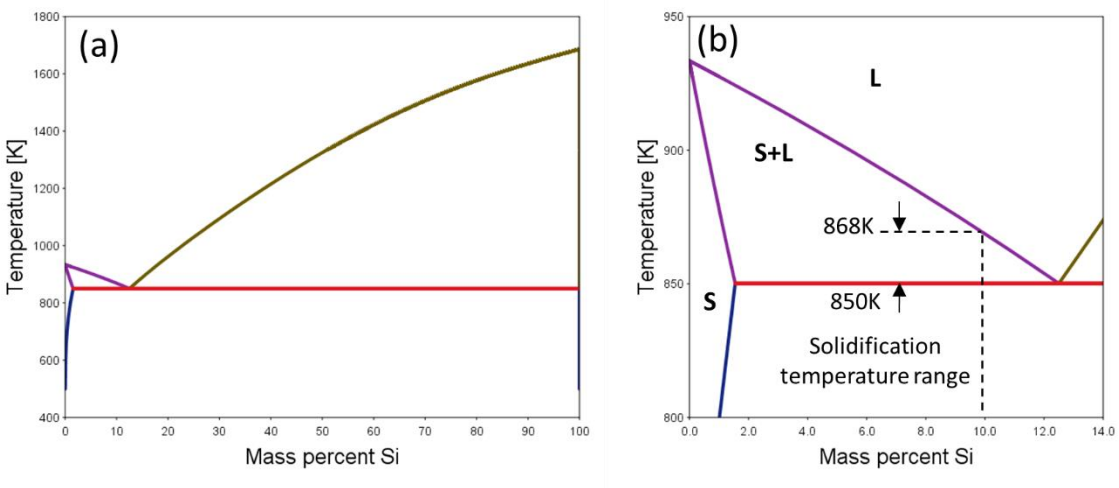

Figure 3. Aluminum-Silicon binary phase diagram, calculated with Thermo-Calc and TCAL4 database.

The solidification behavior of AlSi10Mg alloy was calculated with Thermo-Calc, using the TCAL4 database and the powder composition listed in Table 2. Figure 4 shows predicted possible phases and their mass fractions under equilibrium and Scheil conditions. Both conditions result in the same liquidus temperature of 867K (594°C) (as expected) and similar solidification ranges (27 K and 36 K), which are larger than 18K in the binary system. This wider solidification range indicates that the presence of minor alloying elements is important for understanding the solidification behavior of AlSi10Mg alloy and cannot be ignored. For Scheil solidification, Mg_2Si is predicted to form upon final solidification (whereas under equilibrium conditions, Mg_2Si would form below the solidus temperature). Mg is not present in any intermetallic phases upon solidification under equilibrium conditions, indicating that Mg is mainly dissolved into α-aluminum (considering near zero solubility of Mg in the other solid phase - silicon). For solidification during laser sintering, the actual solidification range would likely be somewhat wider than this, because of the undercooling associated with rapid solidification. Another difference was that – as shown later – the only phases evident in the as-built parts were α-aluminum and Si.

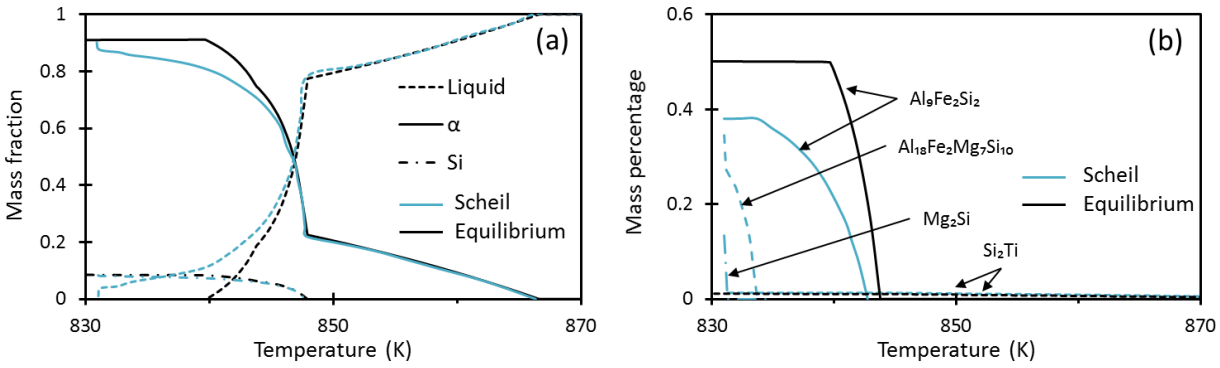

Figure 4. Predicted solidification of AlSi10Mg alloy, for (a) major phases and (b) minor phases. Black lines refer to equilibrium conditions, and blue lines represent Scheil solidification.

In addition to the solidification range and phases, it is useful to know the phase compositions under equilibrium, particularly dissolved Si in α-Al, which could act as barriers to dislocation movement and offer solid solution strengthening. Figure 5 illustrates the solubility of constituents in phases under the equilibrium condition: Si has a maximum solubility of 1.65wt% at the eutectic temperature (850K), and Al has zero solid solubility in silicon at any temperature (also supported by the phase diagram in Figure 3a and Murray et al. [31]). However, the solubility of Si in Al can be extended beyond the equilibrium limit when involving high cooling rates [32], which is also observed in additive manufactured AlSi10Mg alloy in this work and will be discussed later.

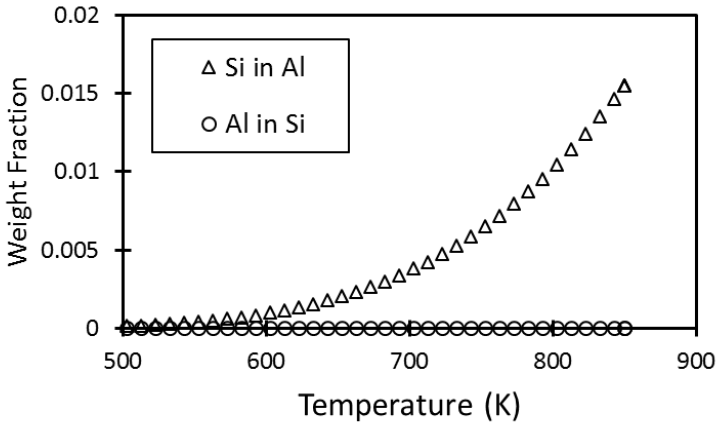

Figure 5. Solubility of constituents in phases in the binary Al-10Si alloy; calculated with Thermo-Calc and TCAL4 database.

Table 4 below lists the equilibrium partition coefficients at 866K (just below the liquidus temperature) for the three main constituents: Si, Mg, and Fe. To calculate these, the concentration of each component in the solid and liquid phases at 866K were estimated with Thermo-Calc, and the concentration ratio between solid and liquid was taken as the partition coefficient. For all these elements, the partition coefficient is less than 1, and hence the solute will tend to accumulate in the liquid phase. In this case of a hypo-eutectic alloy solidifying under Scheil conditions, such segregation will continue until maximum solubility at a eutectic temperature in the liquid phase is reached.

Table 4. Solid-liquid partition coefficients for various elements in the AlSi10Mg alloy at 866K, predicted by equilibrium calculations in Thermo-Calc with the composition of the unused powder from Table 2.

Element	Partition coefficient
Si	0.116
Mg	0.195
Fe	0.006

1.2.2 Solidification microstructure and cooling rate

Figure 6(a) below demonstrates a typical solidification map, which is applicable for all alloy systems. For a given alloy, the interface morphology during solidification process, including planar, cellular, dendritic and equiaxed, is largely determined by the thermal gradient (*G*, unit: °C/m) and growth rate (*R*, unit: m/s). Figure 6(b) reveals the possible suppression of dendrite at a high solidification rate, which could explain the lack of dendritic solidification microstructure in AM parts [33]. Figure 6(c) illustrates primary and secondary dendrite arm spacings in directional solidification. Figure 6(d) shows the dependence of the dendrite arm spacing on cooling rate, which can be expressed by the following exponential function:

$$\lambda_1 = a\dot{T}^{-n} \qquad \text{Equation 1}$$

where λ_1 is the primary dendrite arm spacing (or cell size λ during cellular growth), $\dot{T}$ is the local cooling rate, and *a* and *n* are proportional constants. The exponent (*n* in Equation 1) falls in the range between 0.32 and 0.38, based on 28 alloys with a cellular microstructure and 21 alloys with dendritic solidification [34]. The dependence of secondary dendrite arm spacing on cooling

rate follows a similar exponential relationship and constant *n* (typically around 0.33) can be observed [34].

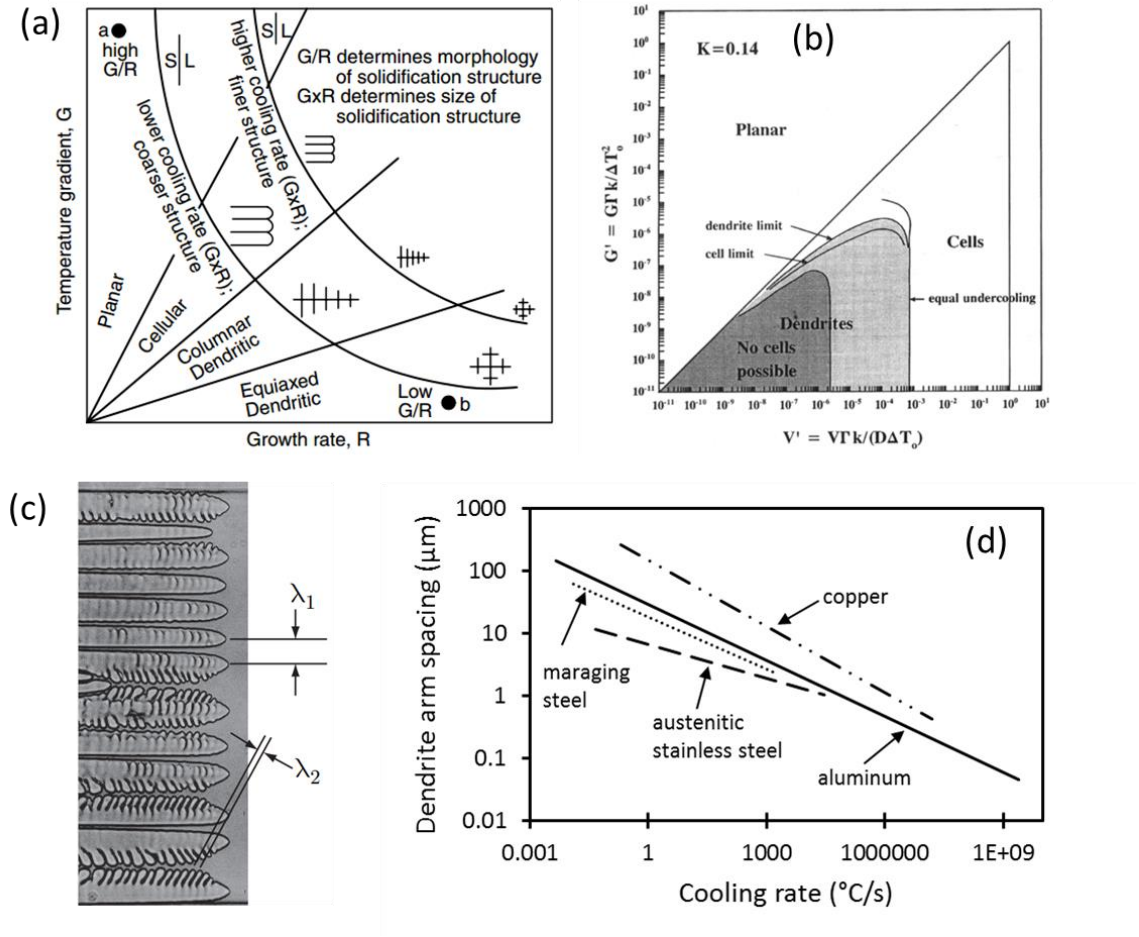

Figure 6. Solidification map, microstructure and its dependence on cooling rate. (a) Effect of temperature gradient *G* and growth rate *R* on the morphology and scale of solidification microstructure [35]. (b) Suppression of dendrites at high solidification rates [33]. (c) Illustration of primary dendrite arm spacing (λ_1 or *DAS*) and secondary dendrite arm spacing (λ_2 or *SDAS*) [36]. (d) Correlation between cooling rate and dendrite arm spacing for various alloy systems [37].

In the direction of beam travel during SLM, the solidification rate is equal to the laser scanning speed (1.3 m/s in this case). This high solidification rate is also associated with fast cooling (of the order of 10^6 K/s through the solidification range), as quantified later. At such high solidification

rates, a cellular microstructure is expected: from work on laser remelting of aluminum alloys surfaces, cellular structures are expected for solidification rates greater than 0.2 m/s, for near-eutectic Al-Si alloys [38].

1.2.3 Effect of heat treatment on Al-Si alloy

Heat treatment is widely applied for cast aluminum alloys to alter microstructure and hence improve physical properties and mechanical performance. During heat treatment of Al-Si and Al-Si-Mg alloys, multiple metallurgical processes can occur simultaneously and potentially affect the physical properties: 1) precipitation of silicon and Mg_2Si from the over-saturated matrix, 2) spheroidization and coarsening of the silicon phase, and 3) dissolution of some precipitates due to the higher solubility limits at an increased temperature [39]–[42]. As electrical conductivity is sensitive to dissolved elements and relatively easy to measure, it is useful to quantify the dissolved constituents for aluminum alloys [43]. Among the possible processes during heat treatment, precipitation, spheroidization, and coarsening of silicon particles increase and dissolution decreases the conductivity, since the electrons would be scattered more effectively by silicon in solution and silicon-aluminum interfaces [40]. Mülazımoğlu et al. [40] investigated the electrical conductivity change of Al-10%Si-0.3%Mg alloy (with similar composition to AlSi10Mg used in this work) after different periods of heat treatment at 540°C; as shown in Figure 7. The authors identified three stages, with stage I controlled by the precipitation of silicon and Mg_2Si, stage II by both dissolution of precipitates and spheroidization process, and finally coarsening of silicon particles in stage III. Similarly, based on the heat treatment temperature (300°C) and time (2h) for AlSi10Mg in this work, we may expect a significant increase in electrical conductivity mainly caused by the precipitation of Si.

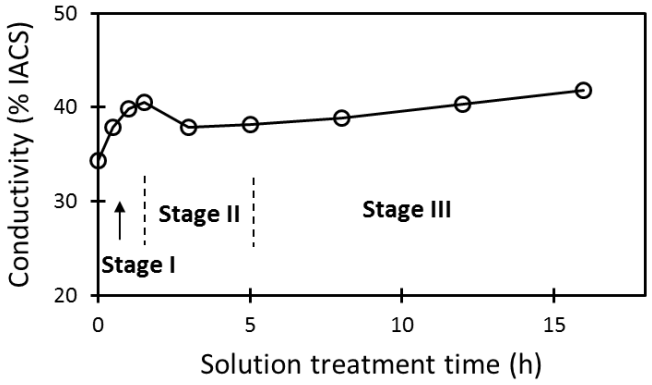

Figure 7. Electrical conductivity change of as-cast Al-10%Si-0.3%Mg alloy as a function of heat treatment time. Heat treatment temperature is 540°C. Adapted from Mülazımoğlu et al. [40]

As for cast aluminum alloys, heat treatment is also commonly used in the post-processing for additive manufactured products. In this work, after fabricating AlSi10Mg parts and before removing from the baseplate, an annealing heat treatment at 300°C for 2 hours is recommended by the machine vendor (EOS) to remove the residual stress induced by the rapid cooling during the laser scanning [29]. Multiple papers have reported the applications of various heat treatments for additive manufactured AlSi10Mg parts, in order to modify solidification microstructure and enhance mechanical properties [44]–[47]. Li et al. [44] investigated the effect of the solution and artificial aging heat temperatures on the morphology and fraction of phases, solid solution and tensile properties. They measured the peak shift in XRD spectra to quantify the concentration of Si in solution and found that 8.9 at% of Si was dissolved in Al matrix in the as-built condition, decreased rapidly during heat treatment at 500°C, and further reduced after artificial aging at 180°C. Si phase was originally in a fibrous network form in as-built parts and precipitated out of solution and spheroidized into particles during heat treatment. Brandl et al. [45] studied the effect of T6 heat treatment (heat treatment with artificial aging) on the fatigue resistance of printed AlSi10Mg parts, and they found that this heat treatment could significantly improve the fatigue life by at least an order of magnitude as compared to the as-built components. The enhancement of the fatigue life by the heat treatment could be attributed to the higher strength [48], as illustrated later in Figure 80. Fiocchi et al. [46] investigated the effect of annealing temperatures (263°C, 294°C, 320°C) on microstructure evolution of AlSi10Mg alloy and applied DSC (differential

scanning calorimetry) to distinguish two exothermic phenomena during heating: Mg_2Si precipitation at 226°C and Si precipitation at 295°C.

1.3 Mechanical behavior of aluminum alloy

1.3.1 Mechanical behavior of AlSi10Mg/SLM

Although metal additive manufacturing has unique advantages of flexible geometric design and less material lost, full utilization of these benefits requires predictable mechanical properties. Previous work on the microstructure and mechanical properties of parts built from AlSi10Mg focused on the effect of powder properties [49], [50], internal porosity of parts [51]–[53], crystallographic texture [28], tensile properties[54], [55], surface roughness [56], hardness [57] and creep behavior [55]. Mechanical properties of AlSi10Mg alloys reported in the literature are summarized in Table 5, including AlSi10Mg parts produced by SLM and die-cast A360 parts.

There has been limited work on fatigue performance [45], [58]. Brandl et al. [45] reported that platform temperature, build direction and heat treatment (peak-hardening) all affected the fatigue life of AlSi10Mg parts produced by SLM, with heat treatment having the largest effect (by improving the strength [48]). Maskery et al. [58] also found that heat treatment (heat treatment for 1 hour at 520°C, followed by artificial aging for 6 hours at 160°C) significantly improved the ductility and fatigue performance of AlSi10Mg parts built by SLM (without subsequent machining), although heat treatment caused some loss of strength. Siddique et al. [59] reported that increasing the base temperature (to 200°C) during selective laser melting (of a slightly different alloy, AlSi12) decreased residual stress, eliminated large pores and decreased scatter in fatigue results, but causing lower static strength and lower average fatigue strength.

Table 5. Summary of mechanical properties of AlSi10Mg alloys reported in the literature, including results for selective laser melting (AlSi10Mg) and die casting (A360). P is laser power, V laser scanning speed, R_p yield strength, R_m tensile strength, and e_f tensile elongation

Reference *SLM- AlSi10Mg*	**Machine**	***P* (W)**	***V* (mm/s)**	**Heat treatment**	**Orientation***	**R_p (MPa)**	**R_m (MPa)**	**e_f (%)**
This work	EOS M280	370	1300	300°C for 2h	*Z* *XY*	180 182	287 285	14.3 17.9
[60]	EOS M270	195	800	shot-peened + 300°C for 2h	*Z* *XY*	231 ± 3 243 ± 7	329 ± 2 330 ± 3	4.1 ± 0.2 6.2 ± 0.3
[54]	(-)	(-)	1000	300°C for 2h	*Z* *XY*	168.8 169	272.8 267	8.2 9.1
[55]	Concept laser M2	175	1025	(-)	*Z* *XY*	232 ± 9 252 ± 17	319 ± 42 339 ± 37	1.1 ± 0.4 1.3 ± 0.8
[45]	Trumpf TrumaForm LF130	250	500	as-built as-built 300°C preheating 300°C preheating T6 T6 300°C preheating, plus T6 300°C preheating, plus T6	*Z* *XY* *Z* *XY* *Z* *XY* *Z* *XY*	(-) (-) (-) (-) (-) (-) (-) (-)	353 282 270 250 353 343 341 353	(-) (-) (-) (-) (-) (-) (-) (-)
[29]	EOS M280	(-)	(-)	as-built 300°C for 2h	*Z* *XY* *Z* *XY*	240 ± 10 270 ± 10 230 ± 15 230 ± 15	460 ± 20 460 ± 20 350 ± 10 345 ± 10	6 ± 2 9 ± 2 11 ± 2 12 ± 2
	EOS M270	(-)	(-)	as-built	*Z* *XY*	230 ± 10 275 ± 10	405 ± 20 445 ± 20	3.5 ± 2 6.5 ± 2

Reference	**Machine**	***P* (W)**	***V* (mm/s)**	**Heat treatment** 300°C for 2h	**Orientation*** *Z* *XY*	**R_p (MPa)** 220 ± 10 225 ± 10	**R_m (MPa)** 325 ± 20 335 ± 20	**e_f (%)** 7 ± 2 11 ± 2
[58]	Renishaw AM250	200	571	as-built 520°C for 1h + 160°C for 6h	(-) (-)	(-) (-)	330 ± 10 294 ± 4	1.4±0.3 3.9 ± 0.5
[61]	Concept laser M1	200	1400	(-)	*Z* *XY*	(-) (-)	396 ± 8 391 ± 6	3.5 ± 0.6 5.6 ± 0.4
[24]	Concept laser M1	200	1400	as-built 175°C for 2h	*XY* *XY*	(-) (-)	396 ± 8 399 ± 7	3.5 ± 0.6 3.3 ± 0.4
Die cast A360								
[62] [63] [64]	(-) (-) (-)	(-) (-) (-)	(-) (-) (-)	as-cast as-cast as-cast	(-) (-) (-)	165 165 165	315 315 315	3.5 5 4

Z: the long axis direction of specimen is along the build direction;
XY: the long axis direction of the specimen is perpendicular to the build direction [2].

1.3.2 Anisotropy of AlSi10Mg/SLM

It is well known that the mechanical properties of both wrought and cast products are not the same for different test orientations relative to the rolling or solidification directions [65]; examples of alloys with such anisotropic behavior are steels [66], [67], aluminum alloys [68], [69] and titanium alloys [70]. Directionality in these alloys is mainly attributed to crystallographic texture and to the alignment of structural discontinuities, including pores, inclusions and second-phase particles [65].

Anisotropic properties are also observed in additively manufactured (AM) products, with properties varying with sample orientation relative to the build direction [2], [6], [7], [12], [71], [72]. Figure 8 illustrates the orientation notation for cylinders built by powder bed fusion: "*Z*" cylinders have their long axis parallel to the build direction (*Z*); the long axis is within the *XY* plane (parallel to the powder spreading direction) for "*XY"* samples. The mechanical properties are often found to differ between *XY*-oriented and *Z*-oriented samples.

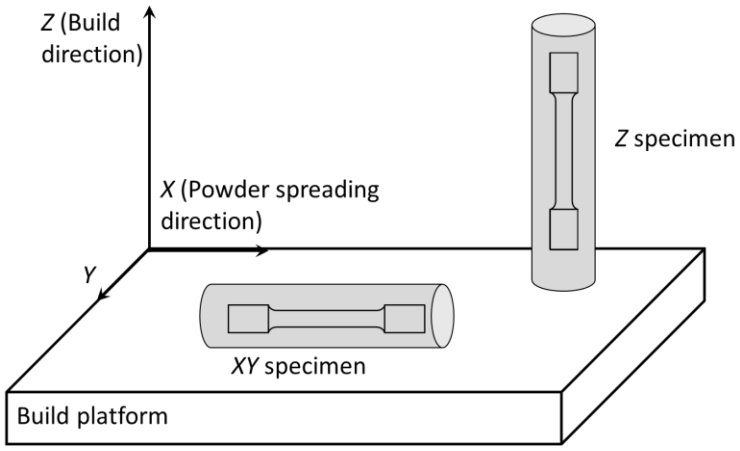

Figure 8. Schematic of *Z* and *XY* samples with respect to the build orientation [2].

The line-by-line and layer-upon-layer fashion in which these parts are built can cause directional variation and heterogeneity of the grain structure and structural discontinuities; these variations can be expected to affect macroscopic mechanical behavior. Several recent projects aimed to understand and control such anisotropy in printed products: Frazier [7] found that AM fabricated titanium alloys do exhibit anisotropy in both microstructure and mechanical properties;

the *Z*-direction was generally weakest and in particular had lower ductility. At least in some cases, such directionality was controlled by lack-of-fusion pores, of which the long axes parallel the scanning path in each layer and hence are perpendicular to the build direction [11], [73]. However, Carroll et al. [71] showed an effect of solidification microstructure, with lower ductility of *XY* samples; this was ascribed to the orientation of columnar prior-β grains parallel to the build direction (*Z*).

Only a few published studies deal with the anisotropy of mechanical properties of additively manufactured aluminum alloy [29], [54], [55], [60], [74], [75]. Figure 9 provides a summary of the reported directionality of the mechanical properties of AlSi10Mg samples fabricated by laser powder bed fusion; the figure compares mechanical properties for *XY* samples with those of *Z* samples. The figure shows that in most cases properties are rather similar, with the most common difference that *XY* samples have higher ductility (shown as tensile elongation in Figure 9).

Crystallographic texture in AlSi10Mg is not expected to contribute strongly to such differences; because the grains grow in the <100> direction during solidification, and the melt pool is slightly elongated in the beam scanning direction, a <100> fiber texture is expected along the scanning direction, but this is disrupted by rotation of the scanning direction in successive layers, as used in the parts considered in this work; a weak cube texture in the build direction is expected [28]. The assumption of a weak effect of crystallographic texture is supported by the absence of a significant difference in elastic modulus of *XY* and *Z*-oriented samples in most of the previously reported results (Figure 9). In this work, the possible anisotropic effect of the locally coarser microstructure in the heat-affected zone (melt-pool boundaries) was examined, for dense samples.

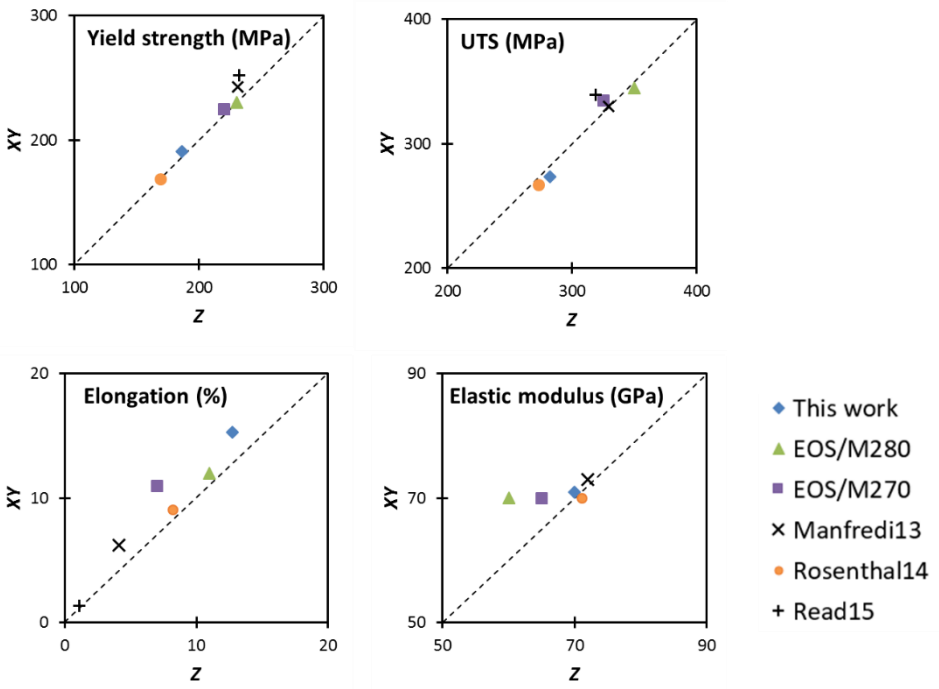

Figure 9. A summary of reported mechanical properties of SLM fabricated AlSi10Mg products [29], [54], [55], [60], [74], [75]. Experimental data for "this work" is from samples built with a standard hatch spacing of 0.19mm (group B and E in Table 19). Data points from EOS datasheets are for AlSi10Mg samples after stress relief at 300°C for 2 hours (as also used in this work).

1.3.3 Work hardening behavior

Work hardening, also known as strain hardening, is a common industrial process to strengthen alloys that do not respond to heat treatment [65]. It occurs as a result of dislocation multiplication during plastic deformation. To better understand the work hardening characteristics mathematically, two relationships were used to fit the experimental tensile flow curve: the Hollomon equation and the Kocks–Mecking (KM) work hardening expression [76]–[79]. The Hollomon equation [77] is a simple power law:

$$\sigma = C\varepsilon_p{}^n \qquad \text{Equation 2}$$

where σ is the true stress, ε_p is the true plastic strain, C is the strength coefficient, and n is the strain-hardening exponent. If this expression holds throughout, the true uniform plastic strain ($\varepsilon_{u|H}$) in the tensile test would be equal to strain-hardening exponent [77]:

$$\varepsilon_{u|H} = n \qquad \text{Equation 3}$$

The Kocks-Mecking (KM) expression assumes a linear relationship between the work-hardening rate (θ) and true stress in stage III (shown later in Figure 60), as follows [78], [80]:

$$\theta = \frac{d\sigma}{d\varepsilon_p} = \theta_0 - K\sigma \qquad \text{Equation 4}$$

where θ is the work-hardening rate, θ_0 is the initial work-hardening rate (the extrapolated rate at zero strain), and K is the slope of the work-hardening curve. Integrating the Kocks-Mecking expression yields the Voce equation [81], [82] for the flow curve:

$$\sigma = \sigma_\infty - (\sigma_\infty - \sigma_0)exp\left(-K\varepsilon_p\right) \qquad \text{Equation 5}$$

where σ_∞ is saturation stress (where θ is zero), and σ_0 is the threshold stress at which plastic deformation starts. In this case, the true uniform plastic strain is as follows:

$$\varepsilon_{u|KM} = -\frac{1}{K} ln\left[\frac{\sigma_\infty}{(K+1)(\sigma_\infty - \sigma_0)}\right] \qquad \text{Equation 6}$$

In this work, the Hollomon and Kocks-Mecking/Voce expressions were used to fit the experimental flow curves of AlSi10Mg parts and compared with literature results for cast aluminum alloy A357 (7%Si, 0.6%Mg) [76].

1.3.4 Fatigue performance of A356/A360

The extensive work on the fatigue behavior of cast aluminum alloys also provides useful insights into the factors which can be expected to control fatigue of SLM parts. Most reported results are for the casting alloy A356, which contains about 7%Si [26]. The fatigue resistance of cast aluminum alloys was reported to be controlled by microstructural defects, typically the largest porosity [83]–[85], and sometimes oxide films [86]. Other microstructural factors which can affect fatigue life include secondary dendrite arm spacing (λ_2 or *SDAS*) or cellular spacing (λ), grain size (including modification by Sr), second-phase particles, intermetallic inclusions, and oxide inclusions (casting dross) [26], [84], [87].

Fatigue failures practically initiate at the surface because of a significant effect of the features at the surface, such as surface roughness, stress raisers at the surface and residual stress [65]. The sample preparation process, including surface finishes by various machining procedures, can also appreciably affect fatigue lives [65]. Additionally, the environmental factors could contribute to the degradation of fatigue performance. Stewart [88] found that the fatigue life of low-alloy steel

is highest in a vacuum, intermediate in dry moist laboratory air, and lowest in moist laboratory air. Piascik and Gangloff [89], [90] investigated the fatigue life of 2090 alloys (aluminum with around 2.7wt% Cu and 2.2wt% Li) under different environment conditions and found that hydrogen embrittlement could explain the environmental fatigue cracking of the alloy in humid air and water vapor, and surface oxide has little effect on intrinsic crack propagation rate. To eliminate the potential uncertainty of these surface factors, all samples in this work were machined to the identical surface finishing as per ASTM standard E466 [91] and fatigue tests were performed at the same ambient temperature and humidity.

1.3.5 Fatigue life prediction

Apart from studying the defects on the fracture surface, it is also of great interest to predict the fatigue life quantitatively. The most widely known theory on predicted fatigue life was proposed by Murakami and Usuki [92], [93] and $\sqrt{\text{Area}}$ was used as a geometrical parameter for expressing the crack growth and estimate the fatigue life of steels. Moreover, they stated that the fatigue crack would be initiated by the largest and critical defect, which is at the tail of the defect size distribution.

Practically, to establish the relationship between defect size distribution (from 2D plane) and fatigue cycles, one needs to (1) evaluate the size distribution of failure-initiating defects and (2) use a crack propagation model to correlate defect area to fatigue life [94], [95].

To estimate the largest values (upper tail) from a given distribution, Gnedenko [96] defined three types of largest extreme value distribution: Gumbel, Fréchet, and Weibull distribution, also known as type I, II and III extreme value distributions. In this work, the area of invidual pores was measured on the polished plane and converted to the equivalent circular diameter d_c:

$$d_c = \sqrt{\frac{4A_i}{\pi}} \qquad \text{Equation 7}$$

With the aid of software CumFreq [97], Gumbel and Fréchet distributions were used to fit the distributions of pore sizes, with probability functions as follows:

Gumbel $$P(d_{max} < d_c) = exp\{-Texp(-Ad_c^E + B)\} \qquad \text{Equation 8}$$

Fréchet $$P(d_{max} < d_c) = exp\left\{-T\left[(d_c - C)exp(\frac{B}{A})\right]^A\right\} \qquad \text{Equation 9}$$

where $P(d_{max}<d_c)$ is the probability that the maximum diameter (d_{max}) is smaller than d_c, A, B, C, E are parameters for the fitted distribution, and T is the scaling factor (also called return period by Murakami and Usuki [92]). T is taken as 1 when fitting Equation 8 and Equation 9 to the analyzed pore sizes from polished planes, and calculated with Equation 10 below when estimating the pore size distributions at the sample surface (by extrapolating the pore size distribution from a limited area to a bigger sample area):

$$T = \frac{S_{sample}}{S_{analysis}/n} \qquad \text{Equation 10}$$

where S_{sample} is the test area of fatigue sample (around 325mm^2 as per the sample dimension in Figure 12), $S_{analysis}$ is the area analyzed for the pore size distribution (around 15mm^2 in this work), and n is the number of pores found on $S_{analysis}$.

The next step is to link the pore size and fatigue life. Quantitative relationships between defect size and fatigue life distributions were also studied for cast Al-Si alloys, particularly A356 [94], [98]–[100]. The following equation was used to estimate the cycles at failure, based on the observation that the crack growth dominates the fatigue life, and using the Paris-Erdogan crack growth expression [94], [101]:

$$N_f = N_i + B\sigma_a^{-m} A_i^{\frac{2-m}{4}} \qquad \text{Equation 11}$$

where N_f is the cycles at the final failure, N_i refers to the cycles to initiate a crack, B and m are Paris-Erdogan constants, A_i is the area of failure-initiating flaw, and σ_a is the alternating amplitude stress. N_i can be taken as zero, since for cast aluminum parts with structural defects, cracks tend to grow from these flaws shortly after the first cycle [102], [103]. Literature on the fatigue of aluminum alloys suggest m between 3 to 4 [65], [86], [99], [104]. A m value of 4 gives an exponent value of -0.5 for defect area (A_i) and supports using $\sqrt{\text{Area}}$ as the geometrical parameter, as suggested by Murakami and Usuki [92].

Microstructural effects are not considered in this study because the samples can be regarded as precracked and failure initiation through slip planes could be a second-order effect [94]. Moreover, oxide inclusions were not taken into account due to their smaller size compared with the pores (observed in Figure 65 and Table 29 in Appendix B).

2 Hypotheses

In this work, the following ideas were tested:

1) The Rosenthal equation from conventional welding can be used to predict the melt-pool size and local cooling rate during SLM.
2) The well-established relationship between cooling rate and scale of solidification microstructure based on cast aluminum alloys is applicable to predict microstructure of AlSi10Mg parts and gas atomized powder from SLM.
3) Similar to the role of Al_2O_3 in cast aluminum alloys, alumina remains as defects inside AlSi10Mg alloy produced by SLM.
4) As with the dominant effect of pores on fatigue performance of cast aluminum alloys, the fatigue life of AlSi10Mg alloy produced by SLM is dictated by the internal residual pores and can be predicted by the pore size distribution.

3 Methodology

3.1 Experimental approach

3.1.1 Mechanical test design

The work here specifically studied the effect of porosity and building orientation on the tensile and fatigue behavior of AlSi10Mg parts produced by selective laser melting, testing the expected correlation between defects and fatigue. Building conditions were based on standard values recommended by the machine and powder supplier (see Table 1). Two experimental variables were tested: hatch spacing and sample orientation during building (see Table 6 and Table 7). The effect of build direction on fatigue life was examined by testing samples built along two directions: one with the long axis of cylinder samples aligned with the build direction, and the other with the long axis of the samples horizontal (perpendicular to the build direction); see Figure 8.

Table 6. Summary of building condition variables in this study.

Variable	#	Comments
Build direction	2	Notation: *XY* (radial build direction; sample lying horizontally), *Z* (built along long axis; "stand-up" orientation)
Hatch spacing (*H*)	3	standard *H* (0.19mm), larger *H* (0.22mm), smaller *H* (0.16mm)

Table 7. Summary of specimens built under different conditions

Group ID	Build direction	Hatch spacing (mm)
A	*XY*	0.16
B	*XY*	0.19
C	*XY*	0.22
D	*Z*	0.16
E	*Z*	0.19
F	*Z*	0.22

The overlap between melt pools is expected to affect defect formation; to study this, three hatch spacings were used: 0.16 mm, 0.19 mm (the default value as listed in Table 1) and 0.22 mm. For comparison, the melt-pool width under the building conditions used here is approximately 0.22 mm and the melt-pool depth is approximately 0.11 mm; see Figure 2.

Hatch spacing is expected to affect both porosity due to incomplete melting and the elimination of defects upon repeated remelting of the part during subsequent laser passes. Sufficient overlap of melt pools to avoid incomplete melting is obtained if the following geometric criterion holds (as will be explained later in the section on porosity prediction) [105]:

$$\left(\frac{H}{W}\right)^2 + \left(\frac{L}{D}\right)^2 \leq 1 \qquad \text{Equation 12}$$

where H is the hatch spacing, L is the layer thickness, W is the melt-pool width, and D is the melt-pool depth. Of the three hatch spacings used in this work (0.16, 0.19 and 0.22 mm), the two smaller spacings satisfied the criterion for full melting. While the largest hatch spacing did not satisfy the criterion, a geometric model (discussed later) predicted that unmelted material would be only 0.02% of the part volume (slightly outside the fully dense arc in Figure 10 below), and hence would not be expected to affect part density significantly. The principle and application of geometric model and processing map are discussed later.

Hatch spacing would also affect the number of times each volume in the part is melted (n_{melt}). Assuming that the melt-pool cross-section can be approximated as two half-ellipses with width W and total depth D, the remelting count is given by:

$$n_{melt} = (\pi/4)(W/H)(D/L) \qquad \text{Equation 13}$$

Based on this expression (derivation available from Equation 37 and Equation 38), the hatch spacings used in this work gave average melting counts of 4.0 (for H=0.16 mm), 3.3 (for H=0.19 mm) and 2.9 (for H=0.22 mm).

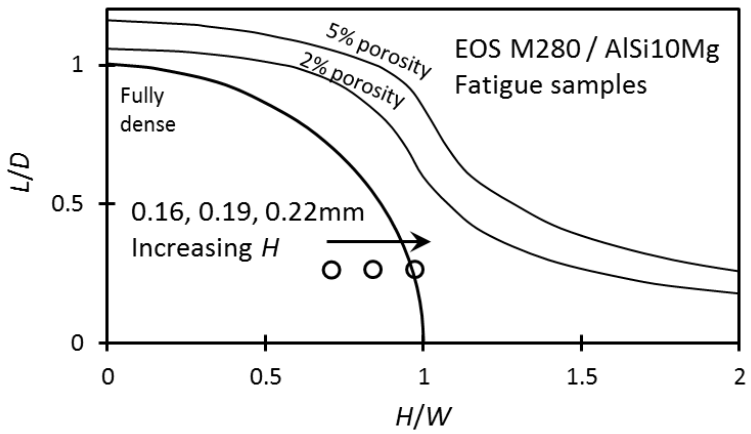

Figure 10. Processing map of three hatch spacings (relative to melt-pool dimensions); conditions within the circular arc would avoid lack-of-fusion porosity, corresponding to Equation 12.

3.1.2 Sample fabrication

All specimens were fabricated using an EOS M280 SLM machine at Arconic Technology Center. Figure 11 shows an as-built cylinder with a dimension of 100 mm length and 15.2 mm diameter.

Based on the two variables (three hatch spacings and two orientations), six groups of cylinders were fabricated, corresponding to the group ID in Table 7. Each group included ten specimens: 2 for tensile tests and 8 for fatigue tests (4 for each stress amplitude). Tensile and fatigue samples were built as cylinders and subsequently machined to the dimensions shown in Figure 12, with the maximum surface roughness of 63 micro-inches (R_a=1.6um). A stress-relief heat treatment (300°C for 2h [29]) was applied after building. Three additional *Z* specimens were built (one at each hatch spacing) for detailed study of microstructure without any heat treatment. Tensile tests were performed according to ASTM standard B557 [106]. Fatigue tests were performed under uniaxial tension according to ASTM standard E466 [91], using a frequency of 50 Hz and two stress amplitudes (80 and 100 MPa), at a stress ratio ($R_{stress}=\sigma_{min}/\sigma_{max}$) of 0.1. All fabrication, machining, and mechanical tests were performed at Arconic Technology Center.

Figure 11. As-built AlSi10Mg cylindrical rod.

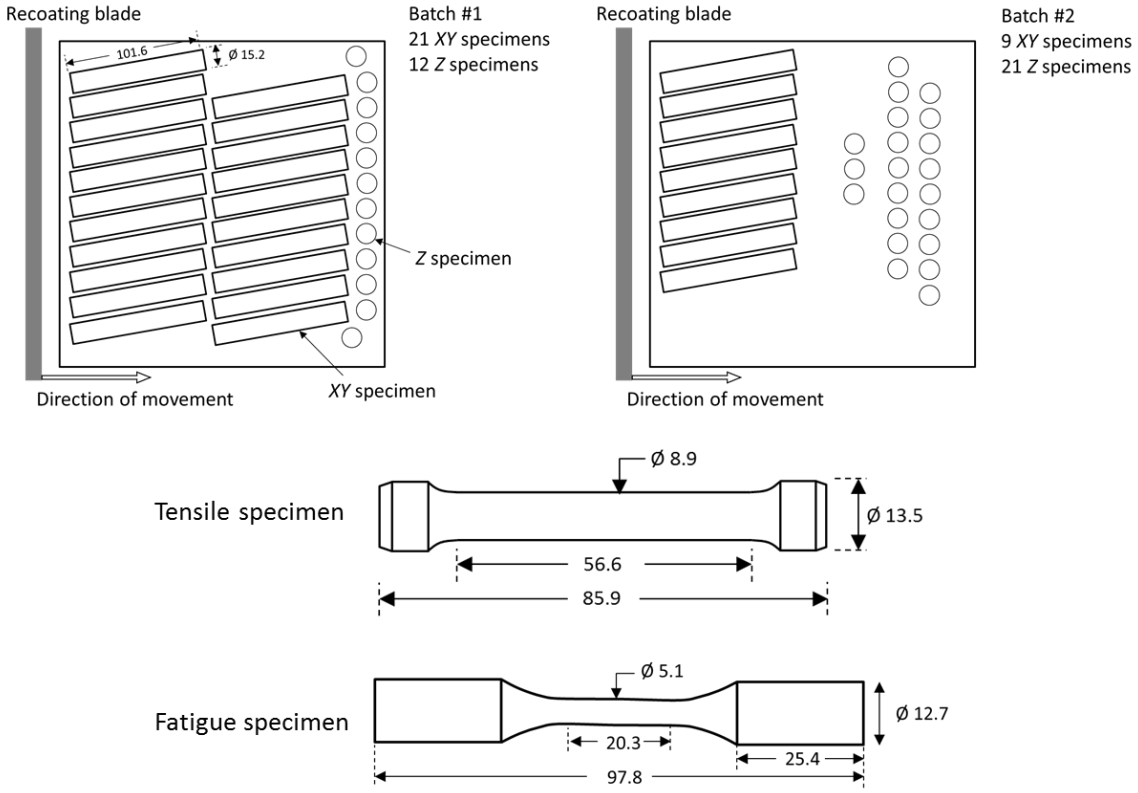

Figure 12. The layout of cylinders during building (two images at the top; plan view) and dimensions of tensile samples and fatigue samples (bottom) machined from as-built cylinders. Units are in mm.

3.1.3 Non-standard single bead specimens

In order to test the dependence of microstructural size on varying processing parameters, non-standard processing conditions were tested by carrying out single bead experiments, which represent the fundamental unit for producing multi-layered components [107]. Figure 13 shows the top view of a single bead track. All the single track experiments with various beam power/velocity combinations were designed by the CMU team (Sneha Narra and Jack Beuth, Department of Mechanical Engineering) in a RAMP project (The Research for Advanced Manufacturing in Pennsylvania program) and carried out on the EOS M280 machine at Arconic Technology Center. In this work, cooling rates were estimated with the Rosenthal equation (discussed later), using the effective power fitted by matching experimental melt-pool sizes. Processing conditions are summarized in Table 8, in which the first two cases are from the top surface and an internal cross-section of a cylinder specimen in this work, and last five cases are from single bead results.

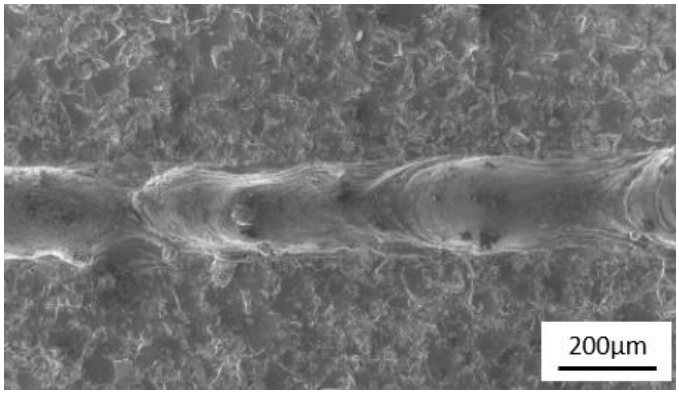

Figure 13. Top view of a three-layer single track with AlSi10Mg powder deposited on a 5083 substrate. Laser power is 370W and scanning speed is 0.2 m/s.

Table 8. Processing parameters for cylinders and single beads

Case No	Power (W)	Velocity(m/s)
1	370	1.3
2	360	1.0
3	100	0.2
4	200	1.4
5	300	0.8
6	370	0.4
7	370	1.4

3.1.4 Microstructure Characterization

The three additional cylinders were used for density measurement, total oxygen analysis, and microstructural characterization of internal cross-sections and of the surface of the last-deposited layer. Detailed quantification analysis on defects (porosity and oxide) will be illustrated in the following section. To study the microstructure, cylinders were sectioned and polished to a 0.04μm finish using colloidal silica. Polished sections were not etched for microanalysis and etched for revealing the fine cellular microstructure, by immersing in Keller's reagent (volume fraction: 1% HF, 1.5% HCl, 2.5% HNO_3, 95% H_2O) for 15 seconds [108], except shorter etching of 3 seconds applied to the samples used for the phase quantification on the polished plane.

Scanning electron microscopy with energy dispersive X-ray spectroscopy (SEM/EDS) was applied to find crack initiation points on the fracture surface after fatigue tests, to study the microstructures, and to perform microanalysis. Three locations were chosen for microstructural analysis: internal cross-sections, the surface of the last-deposited layer, and fatigue fracture surfaces. SEM/EDS was performed at a relatively low accelerating voltage of 5kV with the following two advantages. First, the lower voltage reduces the interactive volume between electron and sample and hence decreases the matrix effect during microanalysis. To ensure the accuracy of EDS analysis, the NIST simulation program DTSA-II (Jupiter version) [109] was used to model the detection of Si when the beam is placed in aluminum at various distances from a vertical boundary of Si. Figure 14 shows that the simulated Si peak height decreases rapidly from the beam center and is negligible at the distance of 0.15μm, which is much smaller than half the Si spacing observed from the polished section (around 1μm as shown in Figure 14). This confirmed that the EDS test performed at 5kV could give a reasonable estimate of the dissolved Si in α-Al without

interference from the fibrous Si. In Figure 14, EDS test locations were intentionally selected in a region with coarser cells in the vicinity of the melt-pool boundary.

The second advantage of applying a low voltage is a higher sensitivity for light elements in microanalysis [110], which is particularly helpful in this study for identifying the presence and estimating the amount of oxygen on the powder surface and inside the final part (as discussed later, oxides originate from the native oxide film on the powder and oxidation during part manufacture). To illustrate the effect of accelerating voltage, Figure 15 shows simulated EDS spectra (using the NIST DTSA-II [109]) of Al_2O_3 with different thicknesses on the Al-10Si alloy substrate, for accelerating voltages of 5 kV and 20 kV. The much great sensitivity for oxygen at the lower accelerating voltage is evident. Because of the much smaller interaction volume with the lower accelerating voltage, the oxygen peak is obvious at 5 kV even with a 3-4 nm thick film. This is the expected thickness of the native oxide film on the aluminum powder [111], with a mass mean diameter of 43μm, which is the size of the AlSi10Mg/EOS powder [60]).

Powder samples were examined in polished and unpolished form. For testing the relationship between microstructure and powder particle size, powder particles partially embedded in epoxy resin were polished, to allow the true diameter of the particles to be measured.

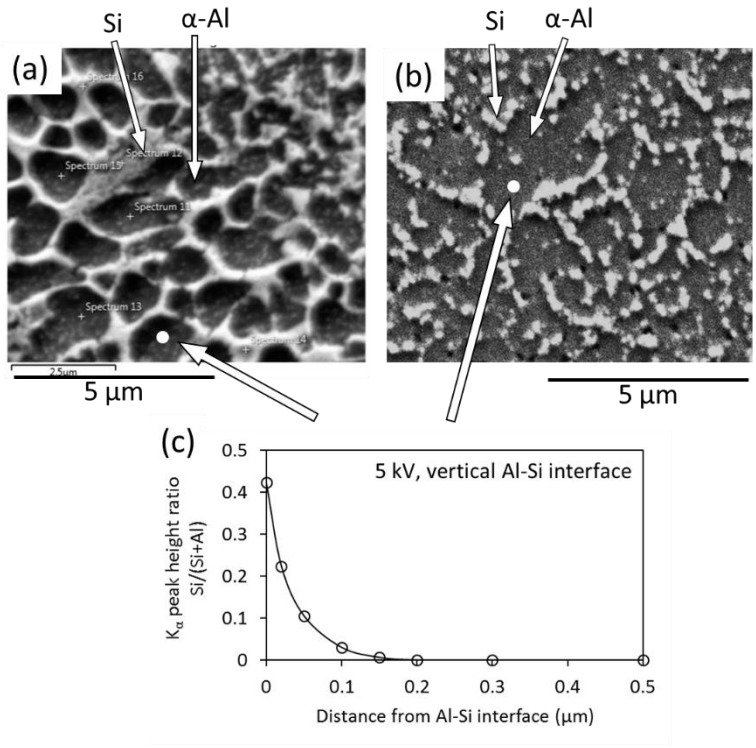

Figure 14. EDS test spots from polished *XY* plane of (a) as-built and (b) heat-treated samples. (c) is simulated *K*α peak height ratio for beam placed within Al and at various distances from a vertical boundary with Si; simulated with DTSA-II [109].

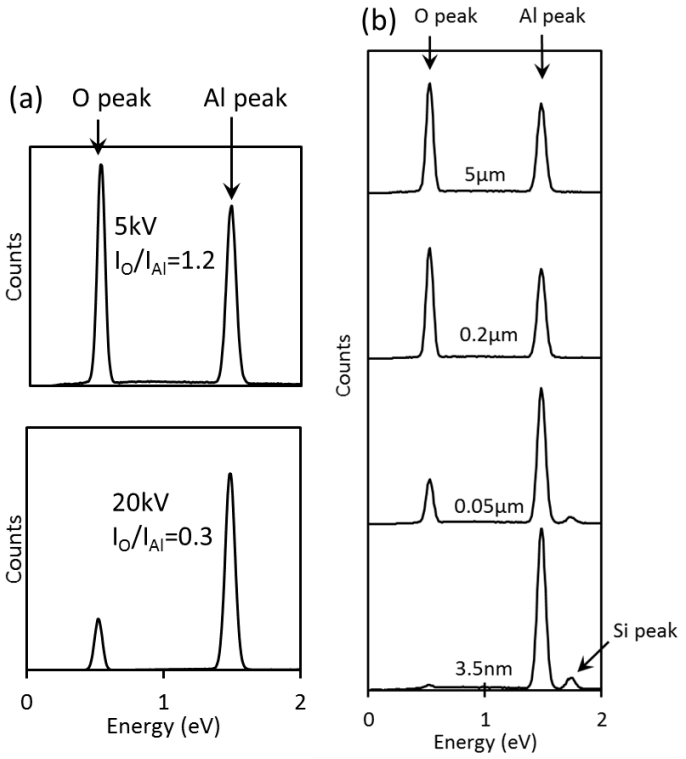

Figure 15. Simulated EDS spectra of Al_2O_3 (a) with infinite thickness, at lower and higher accelerating voltages (5 kV and 20 kV); (b) oxide films of various thicknesses on an Al-10Si substrate; 5 kV accelerating voltage.

3.1.5 Cell size measurement

Cell sizes were measured from backscattered electron images of polished planes which were perpendicular to the laser traveling direction and which contained the build direction. Care was taken to minimize distortion of the measured cell sizes by stereological effects. For built parts, the presence of a few small spherical gas pores allowed direct comparison of the apparent cell size on a polishing plane with the actual cell size visible at the surface of the pore; a few example are shown in Figure 16. Except for the narrow heat-affected zone (typically a few microns wide) at the edge of the melt pool, cell sizes appeared uniform within the melt pools and seem to be unaffected by reheating by subsequent laser melt passes. Cell sizes were also measured for non-standard processing conditions (that is, for combinations of laser power and speed which differed from the standard values, see Table 8) tested by Narra and Beuth [112].

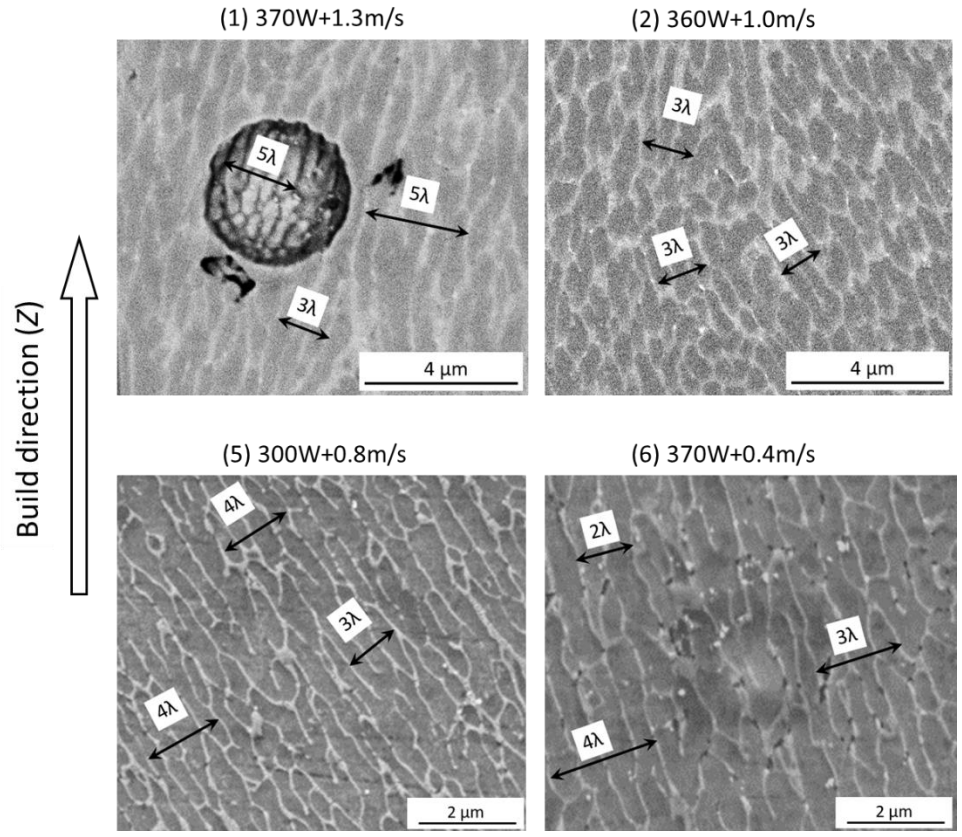

Figure 16. Example electron images of polished cross-sections of built parts and single beads, illustrating the procedure used to measure the cell size (λ). Arrows are shown spanning the width of a few cell spacings on the polished surface. The numbers in the round brackets correspond to the case numbers in Table 8. For sample 1 on the top left, cells are also visible within a gas pore, allowing measurement of cell size with less stereological uncertainty.

3.1.6 Electrical conductivity measurement

Electrical conductivity measurement intends to estimate the silicon concentration in solution and Si present as a separate phase, both decreasing the conductivity (relative to pure aluminum) but at different rates, with linear coefficients tabulated in Table 9. As-built and annealed cylinders (15mm diameter, at least 8mm long) were measured with a Hocking Electrical Conductivity Meter (Model Auto Sigma 3000 DL) with a probe size of 6.4mm diameter (0.25 inch). Both tests were conducted at Arconic, along the longitudinal direction of the cylinder, and at the same temperature of 24°C in the laboratory. The measured conductivity was expressed in the unit of %IACS, the conductivity relative to the International Annealed Copper Standard (IACS). The fundamental

measurement of electrical resistivity in μΩ·cm can be obtained by dividing 172.4 by the IACS number [113]. For simplicity, the alloy was considered as binary Al-10Si. Effects of temperature, other constituents (such as Mg), and phase morphology were not included.

Table 9. Average increase in resistivity (per wt%, μΩ·cm) of aluminum with additional Si [43].

In solution	As a separate phase
1.02	0.088

The quantitative effect of the dissolved Si on the electrical conductivity of the alloy can be first expressed as following:

$$R_{\text{alloy}} = R_{\text{Al}} + 1.02 \times W_{\text{in-solution}} + 0.088 \times W_{\text{separate phase}} \quad \text{Equation 14}$$

where R_{alloy} is the electrical resistivity of the alloy (converted from the measured electrical conductivity), R_{Al} is the electrical resistivity of the pure aluminum (taken as 2.65 μΩ·cm [43]), $W_{\text{in-solution}}$ and $W_{\text{separate phase}}$ are the weight percentages of dissolved Si and precipitated Si, and the two coefficients of 1.02 and 0.088 were taken from Table 9.

By using a mass balance and the relationship between %IACS and resistivity, Equation 14 can be rearranged to the following:

$$W_{\text{in-solution}} = \frac{185}{\sigma} - 2.84 - 0.094 \times W_{\text{all-Si}} \quad \text{Equation 15}$$

where σ is the measured electrical conductivity of the alloy as %IACS, and $W_{\text{all-Si}}$ is the weight percentage of total Si in the alloy. For the case of binary Al-10Si, Figure 17 is a plot of Equation 15.

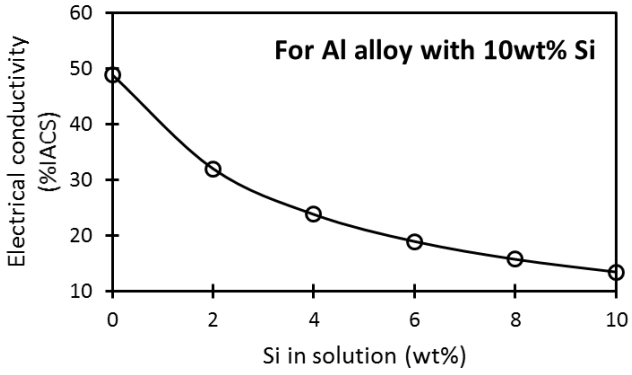

Figure 17. Correlation between measured electrical conductivity and the calculated weight percentage of dissolved Si.

3.1.7 Porosity characterization

Porosity is a key parameter which potentially affects the ductility and dominates the fatigue performance of metal parts if present. Multiple approaches were used to quantify the volume fraction and distribution of the porosity inside the additive manufactured AlSi10Mg specimens, including water displacement method (Archimedes principle), 2D SEM and 3D X-ray microtomography.

Archimedes method

Bulk density was measured by water displacement method (Archimedes principle) using part of the as-built cylinder (15mm diameter and at least 30mm long). The results were that all three hatch spacings resulted in part densities greater than 99% of the theoretical density of 2.68g/cm³ [29], in line with the expected limited or zero volume fraction of the unmelted material. Due to accompanied uncertainty from surface roughness with trapped gas when samples are immersed in the water, the bulk analysis provides the upper limit of the volume fraction of internal porosity.

Automatic feature analysis by SEM

Automatic feature analysis by SEM uses contrast in back-scattered electron image for feature detection and coupled EDS for composition analysis. This is a well-established technique in our group; previous applications of the method have been to nonmetallic inclusions in steel [114]. In this work, this approach was applied on the polished plane of as-built AlSi10Mg parts. To avoid the variation between locations and orientations, a *Z*-containing plane from the top of *Z*-oriented cylinders built with three distinct hatch spacings were sectioned and polished for analysis.

An FEI Quanta 600 SEM equipped with Oxford Instruments INCA (EDS analysis software) was applied with instrument conditions summarized in Table 10. 10kV accelerating voltage is used for a combination of better spatial resolution, sufficient contrast between features, less matrix distortion, and adequate overvoltage (for producing characteristic X-rays for element analysis) [115]. The brightness was calibrated at the boundary between mounted AlSi10Mg sample and epoxy, with brightness values of 200 (metal) and 30 (epoxy), respectively. The upper threshold of 190, which is slightly lower than the matrix brightness, was selected to isolate the detected features from the matrix. The polished section was scanned twice with different threshold values (as indicated in Table 10), one for oxide (150-190) and one for porosity (0-190). Figure 18 demonstrates that some oxide particles and pores are readily separated by the brightness threshold: oxide particles have a brighter appearance than pore due to a higher electron backscattering coefficient. Besides, the features were reaffirmed by the composition analysis: those with more than 15wt% oxygen were identified as oxide, since the distortion effect from matrix could be significant for small oxide particles, showing intermediate oxygen content (less than the theoretical 47wt% for Al_2O_3); a few examples are given in Figure 19. Usually, features with an area larger than 10μm² (or with an equivalent circular diameter larger than 3.60μm) were detected and analyzed. Homogeneity of features was not tested and only the overall composition was reported.

Table 10. Instrument conditions for feature analysis in Quanta 600 and INCA

Parameter	Value
Voltage	10 kV
Spot size	5.0
Image mode	BSE
Field size	512 × 448 pixels
Pixel size	1.0 μm
Magnification	500
Working distance	10 mm
Brightness & Contrast for calibration	30 for epoxy; 200 for matrix
Threshold	0-190 for porosity; 150-190 for oxide

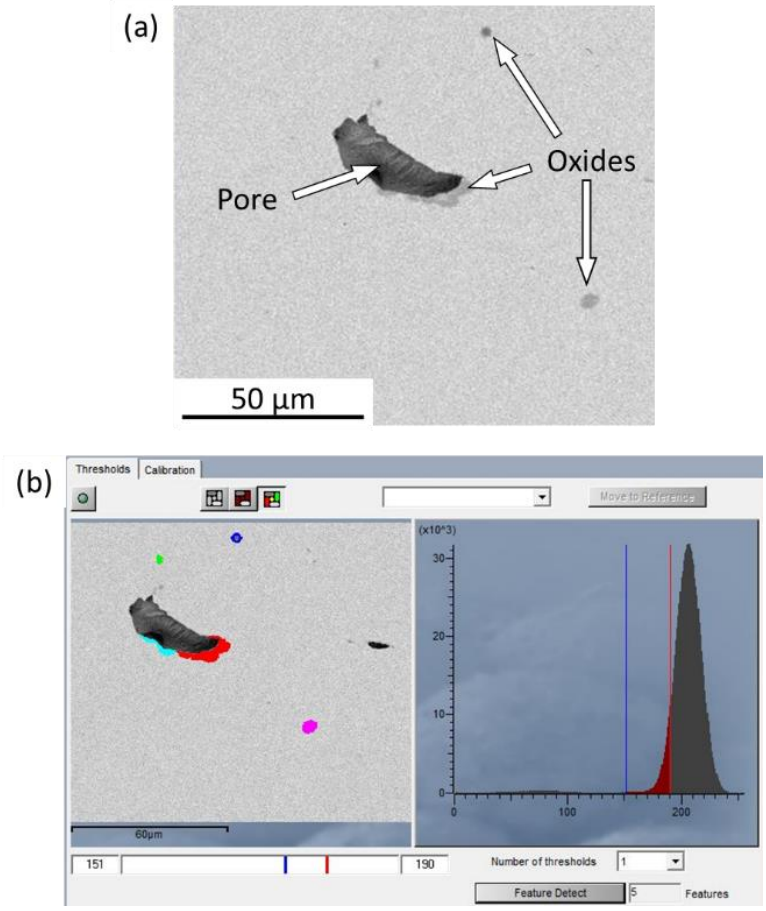

Figure 18. An example of feature detection with a threshold of 150 to 190 to distinguish oxide particles from the polished section and pores. (a) is the backscattered electron image and (b) shows part of the software interface in INCA.

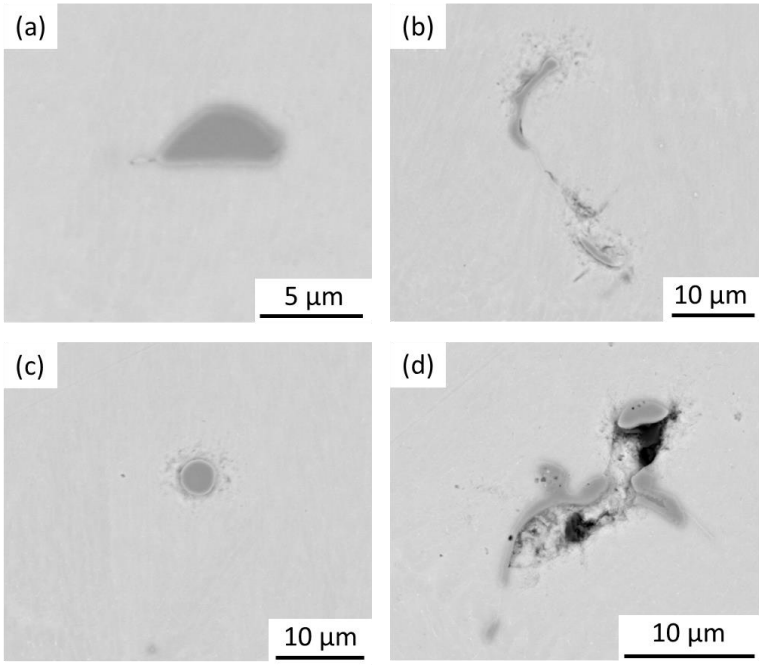

Figure 19. Examples of oxides with distortion effect from the matrix on EDS analysis. Typically, 15 to 35 wt% of oxygen was detected for these features, much lower than the theoretical 47wt% for pure Al_2O_3.

X-ray tomography

The last approach to quantify the residual porosity was X-ray CT (Computed Tomography) using synchrotron radiation, which has the capability of generating three-dimensional maps non-destructively, with many applications, such as spatial distribution of phases in solid, deformation (fatigue and fracture) and corrosion and environmental interactions [116]–[118]. In this study, synchrotron-based X-ray microtomography was performed at the 2-BM beamline of Advanced Photon Source at Argonne National Laboratory. This technique is particularly ideal for AM parts due to the high resolution with a voxel size (edge length) of 0.65µm and rapid acquisition times brought by the high brightness from synchrotron radiation [119]–[121]. Three prisms (square sections with 1.2mm side length and 20mm long) were machined from the as-built cylinders and scanned by x-ray operating at 60kV in monochromatic beam mode.

After scanning, tomographic image reconstruction was performed by TomoPy, a python-based software package developed by Advanced Photon Source staff [122]. Avizo 9 software was applied to segment and visualize internal defects, and calculate characteristics, including volume fraction, shape, and spatial resolution. Due to the similar atomic number and absorption

coefficients of oxide (Al_2O_3) and matrix (AlSi10Mg with α-Al and Si phases), these phases were not distinguishable, and only pores were included for analysis.

Figure 20 shows the reconstructed projection of the sample built with the standard hatch spacing (0.19mm) and pores marked with red are evident.

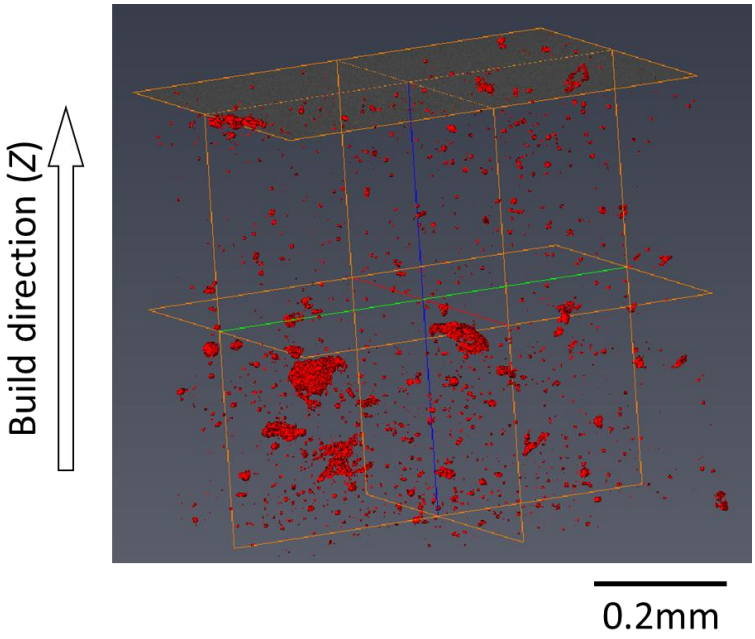

Figure 20. An example of reconstructed sample built with a standard hatch spacing of 0.19mm.

3.1.8 Oxide quantification

Because of the high affinity of aluminum to oxygen, alumina can be easily formed as an oxide film covering powder particles; the film may lead to common defects such as film or particles in aluminum alloy parts and could potentially contribute to fracture [86], [111], [123], [124]. Three approaches were applied to quantify the amount of oxygen in the as-built components, including overall concentration by inert-gas fusion, estimation from the oxide film surround the powder particles, and detailed oxide particle distributions by SEM/EDS (as described in the earlier section of Porosity characterization).

Bulk chemical analysis

Four pieces (10 mm length, 15.2 mm diameter) of the as-built cylinders fabricated with various hatch spacings were sent to Evans Analytical Group for total oxygen analysis by inert-gas fusion. The results are tabulated in Table 11. This showed that the total oxygen content is 370 parts per million (by mass) on average and increases with hatch spacing. Details regarding the effect of hatch spacing are discussed later.

Table 11. Bulk oxygen concentration evaluated by inert-gas fusion

Hatch spacing (mm)	Oxygen concentration (parts per million, by mass)
0.16	290
0.19	310, 410
0.22	460

Oxide film from powder particles

The native oxide film of the powder particles could be expected to be around 3-4 nm thick [111]. Using the reported powder size distribution [60], the expected total oxygen concentration in the parts would be 399 ppm, if the oxide film is assumed to be 3.5 nm thick alumina (density: 4.0 g/cm^3), and if all of this oxide is incorporated in the built part.

Results from oxide particle measurements on the polished plane are presented in the section of 4.3.2 Defect quantification.

3.2 Predicting heat flow

3.2.1 Introduction to Rosenthal equation

In order to better understand the physical phenomena during SLM, it is essential to estimate and predict the melt-pool dimension and thermal history of the melt pool.

The Rosenthal equation [23] was used to calculate approximate thermal profiles for the melt pool:

$$T = T_0 + \frac{Q}{2\pi r k}\exp\left[\frac{-V(\xi + R)}{2\alpha}\right] \qquad \text{Equation 16}$$

where T is the local temperature, T_0 is the plate temperature, Q is the power delivered into the part by the laser beam, $r=(\xi^2+y^2+z^2)^{1/2}$ is the radial distance from the beam position, ξ is the distance from the beam position along the travel direction, k is thermal conductivity, V is beam travel speed, and α is thermal diffusivity (given by $k/\rho C$, where ρ and C are the density and specific heat of the workpiece, respectively). The ξ, y and z directions are illustrated in Figure 21. The expression in the equation is the solution for the temperature distribution in a semi-infinite plate for a three-dimensional case. Limitations of the equation are discussed later.

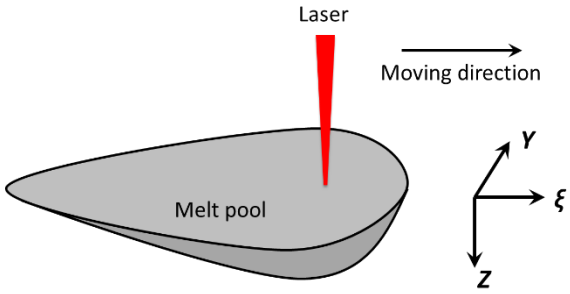

Figure 21. Coordinates for the melt pool. ξ aligns with the laser travel direction and Z is facing down and perpendicular to the top surface.

Relevant alloy properties of six alloy systems (used for comparison of reported melt-pools sizes with Rosenthal calculations) are listed in Table 12. Note that these are room-temperature properties. The Rosenthal equation uses temperature-independent properties; it was found that the properties at room temperature give the best agreement with observed melt-pool sizes for laser melting.

Table 12. Alloy properties used in the Rosenthal equation [125], [126]

Material	Absorptivity* (-)	Melting temperature** (K)	Thermal conductivity (W/m·K)	Density (kg/m^3)	Heat capacity (J/kg·K)
AlSi10Mg	0.32	849	110	2670	915
Maraging steel	0.35	1703	15	8000	450
Stainless steel	0.35	1678	14	7800	460
TiAl6V4	0.48	1913	6.7	4430	526
IN625	N/A	1593	10	8400	402
CoCr	N/A	1683	13	830	470

* Absorptivity here is the average value based on summarized results in Table 13.
** Melting temperature is taken as the average of liquidus and solidus temperatures.

3.2.2 Absorptivity

The absorptivity (η) is defined as the ratio of energy absorbed by the part to laser output energy (that is, $\eta=Q/P$). This parameter is critical for estimating the melt-pool size with a given beam power (P). For calculations on melt-pool dimensions in this work, the absorptivity was collected from literature values, as summarized in Table 13. These literature results were all for laser melting, with a wavelength of 1.06μm. The absorptivity values are for the interaction of the beam with the surface of the melt pool (not powder particles) since for the typical processing conditions the melt pool extends further (in the travel direction) than the beam radius (see Figure 2).

Table 13. Summary of absorptivity values from the literature.

Material	Absorptivity	Remarks	Reference
AlSi10Mg	0.22	Al	King et al. [127]
	0.3	AlSi10Mg	Weingarten et al. [53]
	0.3*	AlSi10Mg	Krishnan et al. [52]
	0.39*	AlSi10Mg	Thijs et al. [28]
	0.39*	AlSi10Mg	Tang et al. [105]
Steel	0.3	304L	Rai et al. [128]
	0.3	316L	Gusarov et al. [129], Masmoudi et al. [130]
	0.3	solid iron	Kruth et al. [131]
	0.33	316L	Khairallah and Anderson [132]
	0.36	solid iron	Yadroitsev et al. [107]
	0.4	316L	King et al. [133]
	0.4	316L	Aboulkhair et al. [51]
TiAl6V4	0.36	Ti	Verhaeghe et al. [134]
	0.44	TiAl6V4	Aboulkhair et al. [51]
	0.64	Ti	King et al. [127]

* Absorptivity was calculated from the Rosenthal equation using the experimentally measured melt-pool width: Krishnan et al. [52]: 156μm width at 180W laser power and 0.9m/s velocity; Thijs et al. [28]: 170μm width at 200W laser power and 1.4m/s velocity; Tang et al. [105]: 278μm width at 360W laser power and 1.0m/s velocity.

However, absorptivity is expected to be somewhat affected by factors such as processing parameters (*P* and *V*), melt-pool surface roughness and oxide coverage, and gas composition above the melt pool. Processing parameters are assumed to be primary factors [135], and dependence of absorptivity on *P* and *V* was estimated: the inputs are dimensions of single beads fabricated with different *P*-*V* combinations, from both non-standard AlSi10Mg single beads studied in this work and literature results [136]–[138]; the procedure was to adjust the value of the absorbed power ($Q=\eta P$) in the Rosenthal equation until the calculated single bead width matched the observed (experimental) results.

Differences in absorptivity would change the melt-pool size; all else being equal, a higher absorptivity would give a larger melt pool. An analytical expression indicates that the melt-pool width is approximately proportional to the square root of the absorbed power (Equation 20; also see the Appendix A for the derivation). This means that the melt-pool width would be approximately proportional to the square root of the absorptivity (all else being equal). Given this relationship, the average absorptivity values of Table 13 would give a good first estimate of melt-

pool size unless builds were made under extreme conditions (such as an excessive beam power and low speed, which could lead to key-holing and significantly higher absorptivity).

Figure 22 shows changes of absorptivity against beam power (left) and beam speed (right), which indicate that the absorptivity somewhat increases with a larger beam power and its correspondence to scan speed is weak. Consequently, the absorptivity used to calculate cooling rates for single beads built with non-standard parameters is varying, since the beam power experiences a large range from 100 to 370W (see Table 8). On the other hand, the absorptivity was assumed to be constant for predicting the density of parts built with processing parameters in Table 26, due to limited power change for each dataset.

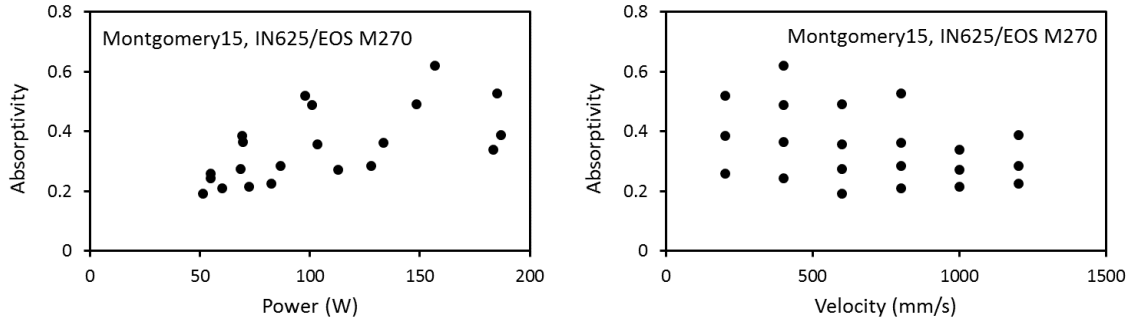

Figure 22. Absorptivity against beam power and velocity [136]. The absorptivity was estimated by fitting Q ($Q=\eta P$) in the Rosenthal equation to obtain a calculated melt-pool width same as the measured width of a single bead.

3.2.3 Validation of Rosenthal equation

The Rosenthal equation relies on several restrictive assumptions [23], [139], [140]. Notably, only conduction is considered, the heat of fusion is not included, thermal properties do not depend on temperature, and the calculation applies to remelting (no addition of powder). However, if the Rosenthal equation is not used to estimate temperatures inside the melt, and only to calculate temperatures in the part up to the boundary of the melt pool, the estimated melt-pool sizes have been found to be realistic and close to experimentally measured values, as shown below.

Within the melt pool, convective stirring decreases the temperature gradient and the analytical (Rosenthal) expression for temperature cannot be correct. However, outside the melt pool, conduction dominates and the analytical expression agrees with the true temperature. Similar melt-

pool sizes are observed with and without powder (discuss shortly), so conduction in the thin powder layer does not appear to affect heat transfer significantly. This conclusion is supported by the observation that semi-circular melt pools are experimentally observed in a cross-section perpendicular to the laser travel direction (see Figure 23), indicating uniform heat extraction under conduction control. Similar images of semi-circular melt-pool shapes were also found in the literature, including figure 2 in Thijs et al. [28], figure 24 in Yasa et al. [141], figure 7 in Manfredi et al. [142], figure 12 in Krishnan et al. [52], and figure 4 from Rosenthal et al. [54].

Use of the Rosenthal equation for selective laser melting conditions implies the assumption that the addition of powder does not change the melt-pool width and depth (although the cap height would change; see Figure 88). The limited data available on widths of melt pools for the same material - with and without powder - do indicate that the difference in melt pool (with and without powder) is small - see Figure 24 (c) and (d). In addition, Montgomery et al. [136] demonstrated that the cross-sectional sizes of IN625 single beads with 20μm powder addition and without powder appear to be almost indistinguishable from each other over a large region of *P*-*V* space (source power from 40 to 200W, beam velocity ranging from 0.2 to 1.2m/s).

Figure 24 shows that, while the melt-pool widths calculated with the Rosenthal equation were similar to the reported measurements, melt-pool cross-sectional areas from the Rosenthal equation were generally smaller (by around 30%) than the experimental results. This was especially the case for low energy densities (compared with standard powder-bed fusion conditions) and very high energy densities. Small energy densities imply small melt-pool sizes, which may invalidate the assumption that the incident beam does not interact with powder. Laser-powder interaction is expected to increase the absorptivity. On the other hand, with very large energy densities, heat transfer to the metal parts changes from the conduction mode to key-holing, in which case the presence of vapor inside the keyhole would increase the effective absorptivity and penetration depth [143]. The effect of a slightly larger melt-pool depth on part density was tested by simulation; the results are reported later in this study.

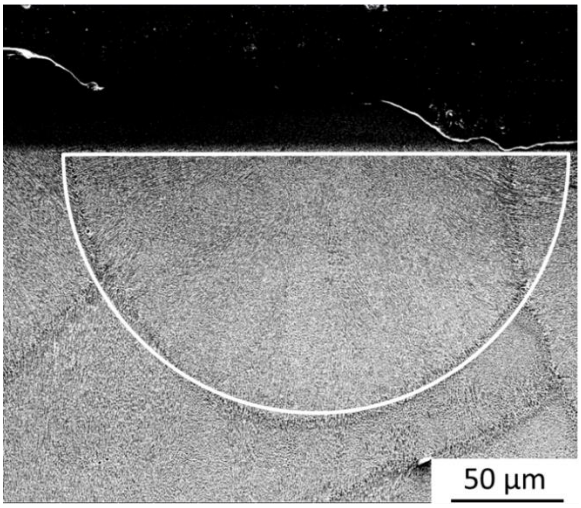

Figure 23. Top surface for a complete melt-pool cross-section (P=360W, V=1m/s), which is perpendicular to the laser travel direction.

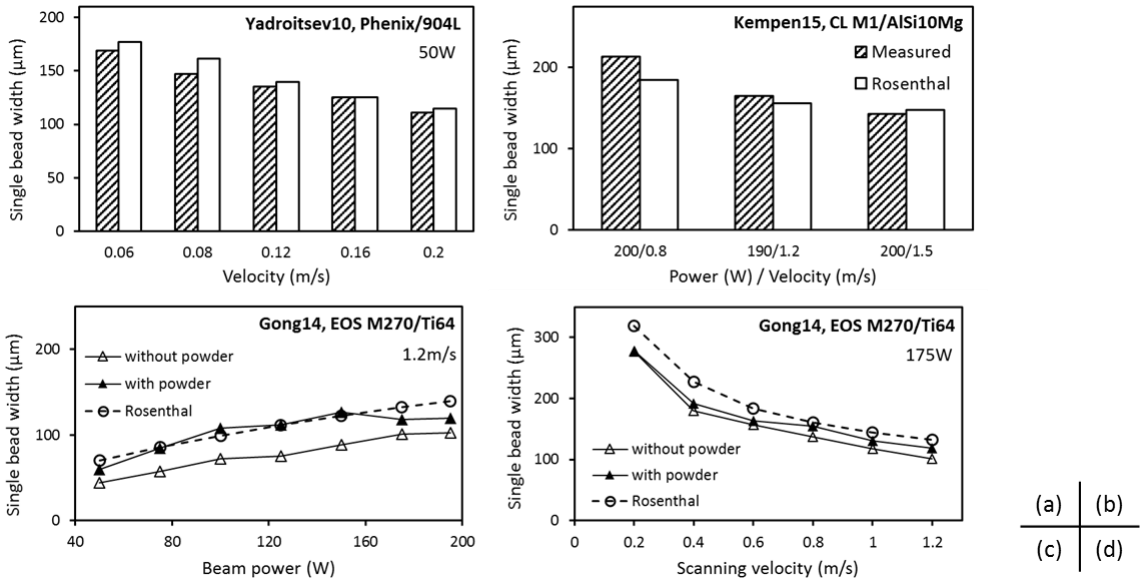

Figure 24. Comparison of experimentally measured melt-pool widths with the Rosenthal equation predictions (a-[107],b-[24],c&d-[137]). The data source, SLM machine, and powder materials are listed in the top right corner of each figure. Beam power and velocity are the only two variables. Melt-pool sizes were measured from the micrographs provided in the papers. Alloy properties and absorptivity used in the Rosenthal equation are listed in Table 12.

3.2.4 Calculation approach: melt-pool size and cooling rate

The calculated melt-pool shape and thermal profiles (for standard conditions, taking T_0=308 K) are illustrated in Figure 25. Based on these calculations, the melt pool is approximately 220µm wide and 320µm long, which is larger than the beam diameter (100µm). The cooling rate between the liquidus and solidus temperatures at the top of the melt pool along the path of the laser beam is approximately 2×10^6 K/s.

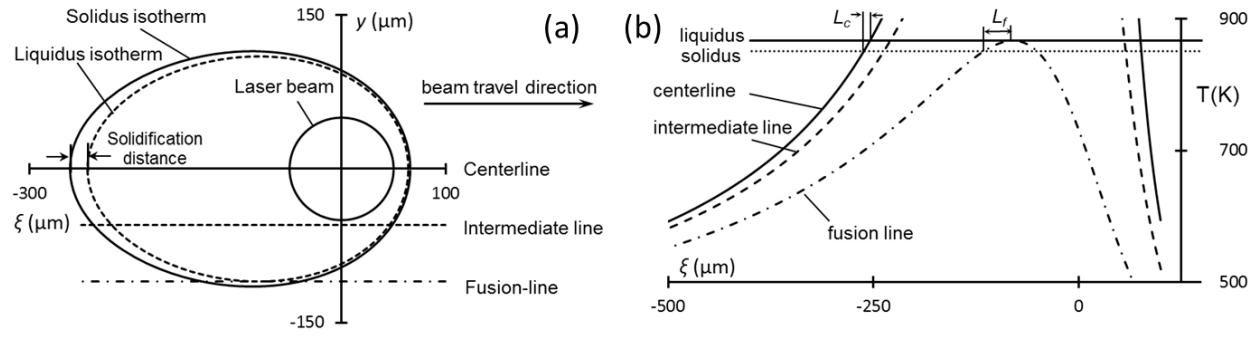

Figure 25. Approximate melt-pool conditions, as calculated using the Rosenthal equation: (a) melt-pool shape (top view), and (b) thermal history for three different positions at the top surface of the melt pool; the arrowed distances L_c and L_f give the solidification distances along the centerline and along the fusion line.

The Rosenthal equation cannot be expected to give a fully accurate description of the thermal conditions, given its restrictive assumptions (as stated earlier). However, as an analytical expression, it is very useful for illustrating trends. For example, the average surface cooling rate between liquidus and solidus at the end of the melt pool along the laser scanning direction (that is, at y=z=0) can be derived from Equation 16 and is given by:

$$\dot{T} = 2\pi k\left(T_{\text{solidus}} - T_0\right)\left(T_{\text{liquidus}} - T_0\right)\frac{V}{Q} \qquad \text{Equation 17}$$

where $\dot{T}$ is the cooling rate, T_{solidus} and T_{liquidus} are the liquidus and solidus temperatures, and T_0 is the plate temperature. The calculation of the cooling rate was performed for the cylinder specimen built with standard conditions and single beads fabricated with non-standard parameters (in Table 8). Since (as mentioned below) the cell size depends directly on the cooling rate, Equation 17 shows that it should be possible to manipulate the cell size by changing the heat input (Q/V).

3.2.5 Calculation approach: cell size and secondary dendrite arm spacing

The relationship reported by Matyja et al. [144] for rapidly cooled aluminum alloys was used to predict cell sizes; the relationship was fitted as follows:

$$\lambda = 43.2\dot{T}^{-0.324} \qquad \text{Equation 18}$$

where λ is the cell size in µm, and $\dot{T}$ is the cooling rate in K/s. This predicts similar cell sizes to those reported by Spear and Gardner [145], and smaller (by a factor of approximately two) than those found with the correlation given by Zolotorevsky et al. [146].

For atomized powder, the dendrite arm spacing varies with particle size, because larger particles cool less rapidly; reported relationships for aluminum alloys (mainly Al-Cu) [37], [147] were compared with the measurements on AlSi10Mg EOS powder. The relationship fitted to the data of Dubé et al. [148] is as follows:

$$SDAS = 0.14 D_{\text{particle}}^{0.61} \qquad \text{Equation 19}$$

where $SDAS$ is the secondary dendrite arm spacing (in µm), and D_{particle} is the particle diameter (in µm). The exponent (0.61) appears reasonable, falling in the range between 0.5 and 1.0 which is typical for powder produced by gas atomization [149].

3.2.6 Solutions for Rosenthal equation

The last part in this section deals with the effect of processing parameters (mainly power and velocity) on the melt-pool dimensions. Two approaches are applied to estimate the melt-pool boundary by solving the Rosenthal equation and obtaining possible positions of the edge of the melt pool (calculated as the contour of the melting temperature, tabulated in Table 12 for different alloys).

Numerical solution

The first method is a numerical solution (using the Newton-Raphson method) implemented in an Excel spreadsheet. A numerical method is needed because the Rosenthal equation (Equation 16) can be used to calculate temperature explicitly for known positions, but positions are not given as explicit functions of temperature. Figure 26 schematically demonstrates the melt-pool dimensions for a given melt pool (top view). Figure 27 illustrates melt-pool dimensions calculated for varying absorbed powers and scan velocities. A higher power causes a larger melted area, in

both length and width. A smaller scan speed has little effect on the total melt-pool length along the scan direction but increases the width (and depth) appreciably. Figure 28 shows the calculated melt-pool dimensions of difference materials with identical absorbed power and velocity. The titanium alloy has a larger melted volume and aspect ratio (length/width) of melt pool, which results from the alloy properties, particularly a lower thermal conductivity (6.7 W/m·K compared to 14 W/m·K for austenitic stainless steel and 110 W/m·K for AlSi10Mg alloy).

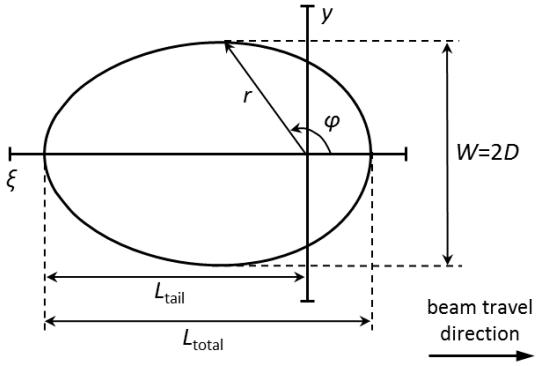

Figure 26. Schematic of melt-pool dimensions for AlSi10Mg with 100W absorbed power and 1m/s speed (viewed from above; frame of reference moves with the beam). The beam is focused at the intersection of the y and ξ axes.

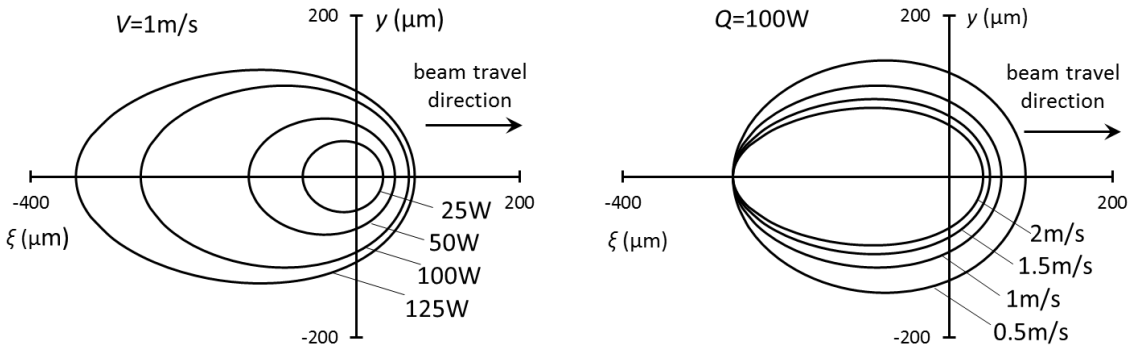

Figure 27. Top view of melt-pool dimensions with different powers and velocities. Constant velocity (1m/s) and absorbed power (100W) are applied to conditions in left and right side graphs, respectively. Alloy: AlSi10Mg

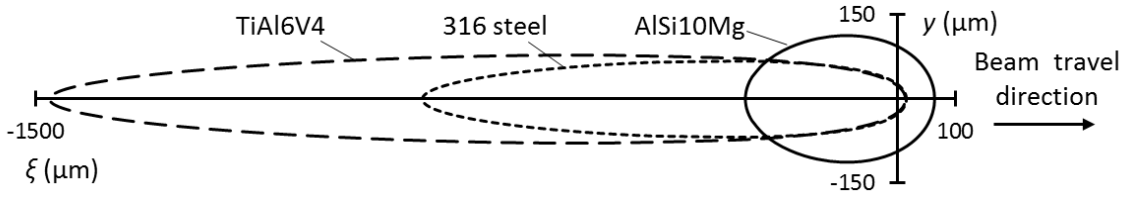

Figure 28. Top view of calculated melt-pool dimensions of different materials, including AlSi10Mg, 316 stainless steel, and TiAl6V4. Absorbed power and velocity are constant, at 100W and 1m/s.

Analytical solution

The second approach is to solve for characteristic melt-pool dimensions (width=2×depth and length) analytically. Several simplified approximate expressions were derived, with details given in Appendix A.

Melt-pool width (W) and depth (D):

$$D = \frac{1}{2}W \approx \sqrt{\frac{2Q}{e\pi\rho C(T - T_0)V}} \qquad \text{Equation 20}$$

Cross-sectional area (perpendicular to laser travel direction):

$$A \approx \frac{Q}{e\rho C(T - T_0)V} \qquad \text{Equation 21}$$

Melt-pool length (along laser scan direction):

$$L_{total} \approx \frac{Q}{2\pi k(T - T_0)} \qquad \text{Equation 22}$$

The aspect ratio of the melt pool:

$$\frac{L_{total}}{D} \approx \sqrt{\frac{eQV}{8\pi k\alpha(T - T_0)}} \qquad \text{Equation 23}$$

The absorbed power required to achieve a certain melt-pool depth can be estimated as follows (Equation 24 for AlSi10Mg; Equation 25 for all the other alloys in Table 12):

$$Q \approx 2\pi k(T - T_0)D + 0.4e\pi\rho C(T - T_0)VD^2 \quad \text{Equation 24}$$

$$Q \approx 2\pi k(T - T_0)D + 0.5e\pi\rho C(T - T_0)VD^2 \quad \text{Equation 25}$$

For Equation 24 and Equation 25, the two terms on the right side correspond to powers required to obtain a prescribed melt-pool depth at zero scan speed ($2\pi k(T\text{-}T_0)D$), derived from the Rosenthal equation with V=0) and non-zero speed (rearranged from Equation 20), and they also refer to the intercept and slope of the melt-pool area contour in a Q-V space, respectively (see Figure 29). For AlSi10Mg, Equation 20 does not hold true because of the high thermal conductivity, but adding an extra fitting factor of 0.8 to adjust the slope of the area contour in Q-V space ($0.5e\pi\rho C(T\text{-}T_0)D^2$)) can give a reasonable match with the analytical expression (Equation 24) with full (numerical) solution; see the bottom-right graph of Figure 29. Refer to the Appendix A for derivation details.

As can be seen from Equation 20 and Equation 22, under prescribed processing parameters (mainly Q, V, T_0), the melt-pool dimensions are entirely controlled by alloy properties: density (ρ) and heat capacity (C) dominate the melt-pool dimensions perpendicular to laser travel direction; and thermal conductivity (k) is the limiting factor responsible for length along beam moving direction.

Reasonable success of these approximate analytical expressions can be demonstrated by comparing with full numerical Rosenthal solution (see Figure 29) and finite element analysis (FEA) simulations from literature results (see Figure 30): the melt-pool depth and area contours are drawn using the simplified analytical expressions (Equation 24 and Equation 25) are in line with data sets from numerical solution and FEA simulations. The slight disagreement between the analytical solution and FEA simulation in Figure 30 could be explained by quantitatively comparing the slopes of dots/plots for constant melt-pool areas, as shown in Table 14. Slopes were extracted from data points by linear fitting; the slope should be equal to the pre-coefficient in Equation 25 ($0.5e\pi\rho C(T\text{-}T_0)D^2$). As illustrated in Table 14, errors between slopes from two methods are somewhat consistent with difference melt-pool areas, which indicates that the slight discrepancy might be caused by the choice of alloy thermal properties, rather than the analytical derivation.

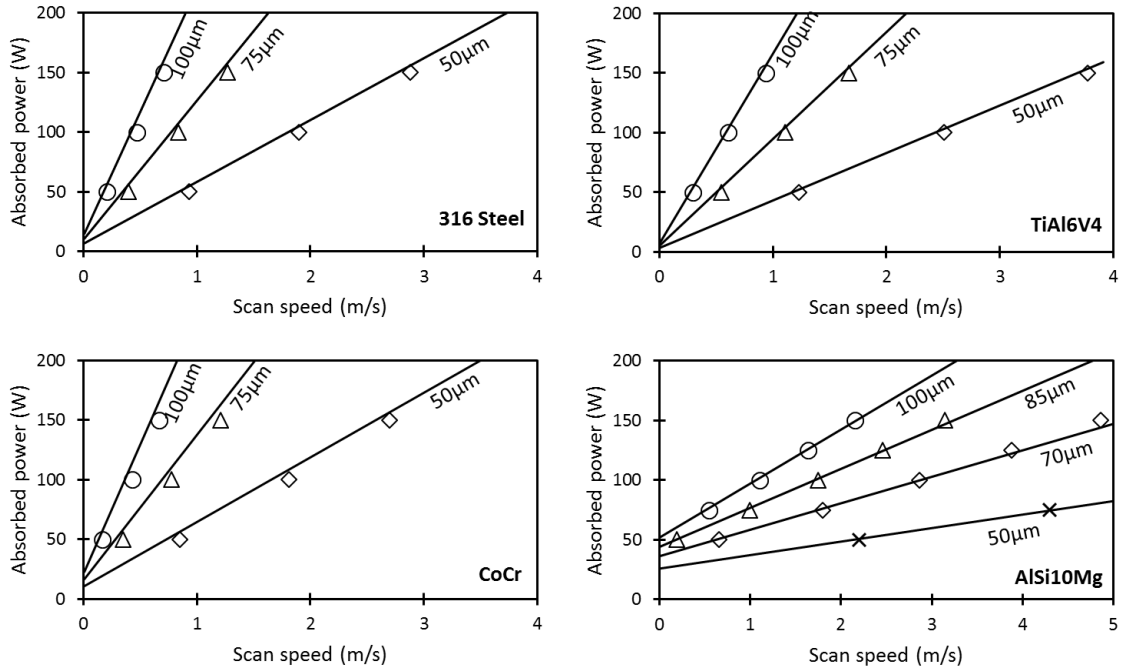

Figure 29. Comparison of melt-pool depth calculated with numerical solution of the Rosenthal equation (data points) and approximate analytical expressions (solid lines, calculated with Equation 24 for AlSi10Mg and Equation 25 for other three alloy systems)

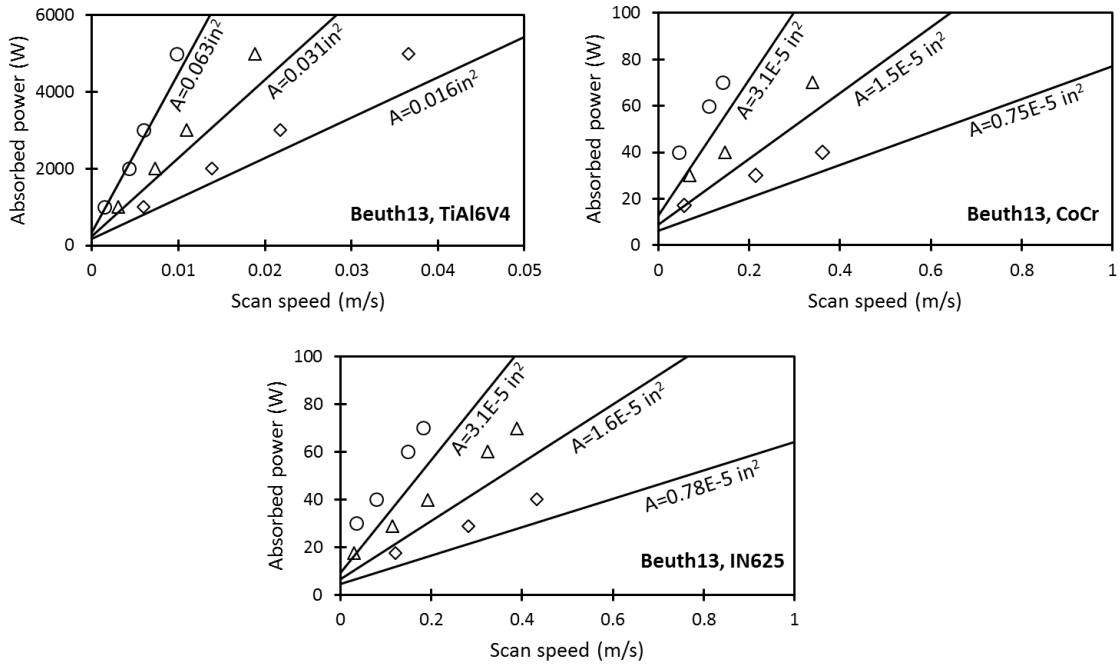

Figure 30. Comparison of transverse melt-pool area between FEA simulation (data points read from Beuth et al. [150]) and analytical solution (solid lines, calculated with Equation 24)

Table 14. Comparison on the slopes for the constant melt-pool area between FEA simulation and the analytical expression for TiAl6V4 (top-left graph in Figure 30).

Area (in^2)	Slope from FEA simulation (W·s/m)	Slope from analytical expression (W·s/m)	Relative error of slopes
0.063	4.8×10^5	4.1×10^5	0.14
0.031	2.5×10^5	2.0×10^5	0.20
0.016	1.3×10^5	1.1×10^5	0.19

4 Results and Discussion

4.1 Microstructure

4.1.1 Metal powder microstructure

Characteristic features

Figure 31 illustrates typical features of the metal powder. While the powder particles appear generally spherical (Figure 31a), the particles depart from ideal sphericity in two main ways: smaller "satellite" particles are attached to large particles and "splats" are observed (Figure 31b). The splats often exhibit dendritic features, showing that these were partially solidified particles which collided with fully solid particles during atomization.

The dendritic solidification microstructure (Figure 31c) and precipitated intermetallic phases (Figure 31d) are also evident on the powder surface at a higher magnification. EDS spot analysis of intermetallic showed an obvious Mg peak (analyzed Mg mass fraction around 12%), which is close to but slightly lower than 16% of the $Al_{18}Fe_2Mg_7Si_{10}$ phase (as predicted by Scheil model). The presence of Mg in the intermetallic supports the use of the Scheil model, rather than equilibrium solidification. A likely cause of the lower Mg concentration in microanalysis is that the size of observed intermetallic (around 0.5μm wide) is small compared to the electron-material interaction volume (0.7μm deep at 5kV for Al-10Si, predicted by NIST DTSA-II [109]). The AlSi10Mg matrix with a relatively lower Mg concentration (0.4%) might partially contribute to the overall composition analysis, thus decreasing the average Mg concentration to some extent.

Some powder particles contain internal pores (Figure 31e), likely entrapped atomizing gas. These can affect part quality: satellites and splats are likely to affect the spreading behavior of the powder, and entrapped gas would contribute to part porosity if the gas did not escape from the melt pool before solidification.

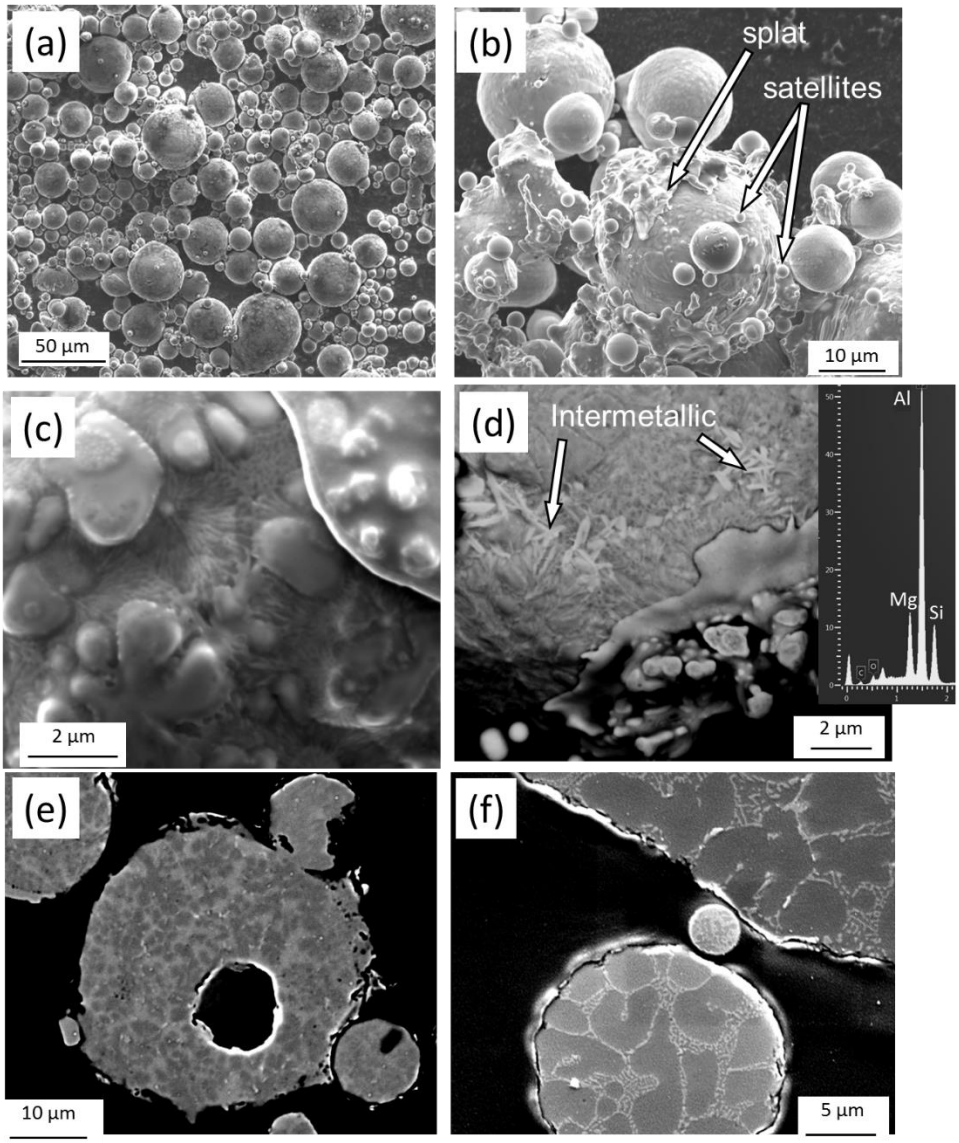

Figure 31. Typical features of atomized metal powder. (a) General view (secondary electron image). (b) Higher-magnification view, showing splat and satellites (secondary electron image). (c) Dendritic solidification microstructure from powder surface (secondary electron image) (d) Intermetallic on the powder surface (backscattered electron image). (e) Polished cross-section, showing an internal pore (backscattered electron image). (f) Polished cross-section through three particles with different sizes, showing differences in dendrite arm spacing and eutectic component (backscattered electron image).

SDAS and eutectic fraction

The expected trend of dendrite arm spacing with particle size was found, as illustrated qualitatively by the polished section through three particles of different sizes (Figure 31f), and quantitatively in Figure 32a. The secondary dendrite arm spacing varied from around 0.4µm to 4µm, for particle diameters from 4µm to 140µm. The observed relationship between dendrite arm spacing and particle size closely followed those reported by Dubé et al. [148] and Grant [37] for atomized aluminum alloys.

The fraction eutectic component in the microstructure was estimated for a number of particles; the approach was to measure the average Si concentration in the α-aluminum (approximately 2wt% Si in all cases) and in the eutectic component (containing approximately 22wt% Si), by SEM/EDS area analysis. The fraction eutectic was then found with a simple mass balance, taking the overall Si concentration in the alloy to be 10wt%. The results in Figure 32b indicate a similar fraction eutectic component for smaller and larger particles, much lower in all cases than the equilibrium eutectic fraction (which is approximately 80%, as shown in Figure 4). This is somewhat similar to the results previously reported for atomized near-eutectic Al-Si alloys, in which the fraction eutectic component depended weakly on particle size, although larger particles had a higher fraction eutectic [151], [152]. For comparison, the results of Armstrong et al. [152], which were presented in terms of cooling rates, were converted to estimated particle sizes based on the correlation from Dubé et al. [148]. For the powder particles examined in the current work, the higher silicon concentration in the eutectic component than equilibrium (the actual silicon concentration in the eutectic component was around 22wt%, compared with 12.5wt% at equilibrium) and the associated decrease in the fraction eutectic component in the microstructure (around 40%, compared with 80% at equilibrium) reflect the shift in the composition of the coupled eutectic zone to higher silicon contents at higher solidification rates [153]–[155].

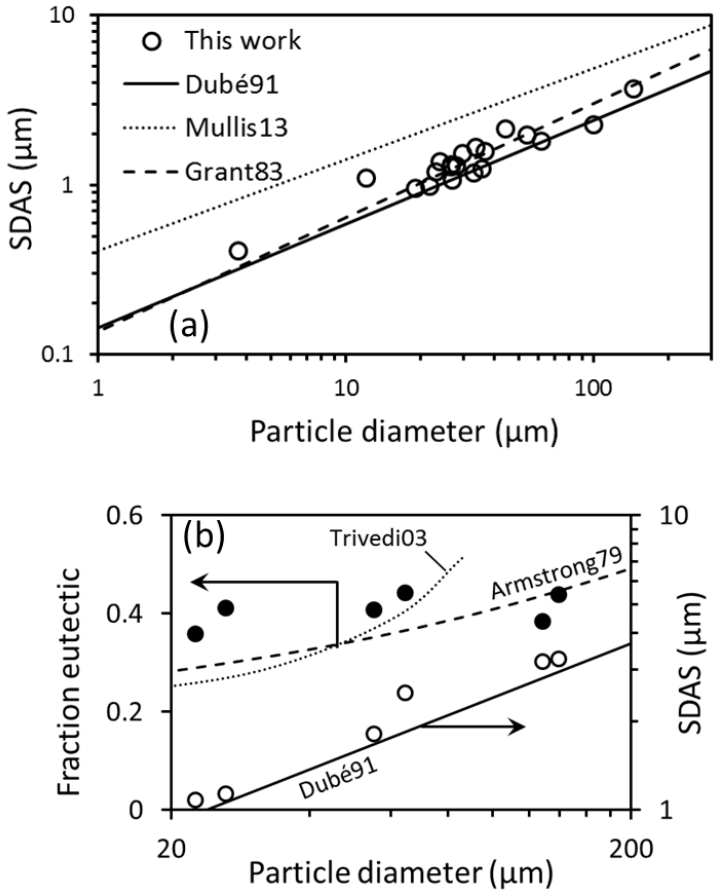

Figure 32. Variation of metal powder microstructure with particle size. The data points are measured in this work and lines refer to literature correlations. (a) Comparison of measured secondary dendrite arm spacing with literature correlations, for atomized metal powder [37], [147], [148]. (b) Variation of fraction eutectic component and secondary dendrite arm spacing with metal powder size for a few powder particles [151], [152].

4.1.2 Melt-pool microstructure

Mesostructure

The EOS laser sintering system used in this work rotates the laser scan direction by 67° for every layer that is deposited. The result is a complex pattern of variations in apparent melt-pool width and overlap on a vertical section through the built part, illustrated in Figure 33 experimentally and Figure 34a schematically. Optical micrographs of etched samples (Figure 33) show contrast along the edges of the melt pools (the interwoven appearance of the melt pools is a result of the hatch spacing between scans in one layer, and the hatch rotation angle of 67° between consecutive layers). The tracks of each laser scan are not continuous in the cross section due to the variation of melt-pool dimension (particularly depth). The optical contrast arises because the cell spacing is of the order of the wavelength of visible light. The melt-pool boundary is less obvious in the stress-relieved samples, since the heat treatment breaks up the cellular Si network (as discussed later) and subsequently decreases the contrast under the light.

Epitaxial growth of grains from the fusion line in the melt pool is evident in Figure 34b. Electron channeling contrast allows grains to be distinguished in this backscattered electron image [156]; several grains can be seen to be continuous across the melt-pool boundaries. This is similar to the growth of grains from the fusion line observed in fusion welds [157]. The resulting grains are large – around 10 μm wide, and spanning the entire depth of the melt pool in several cases.

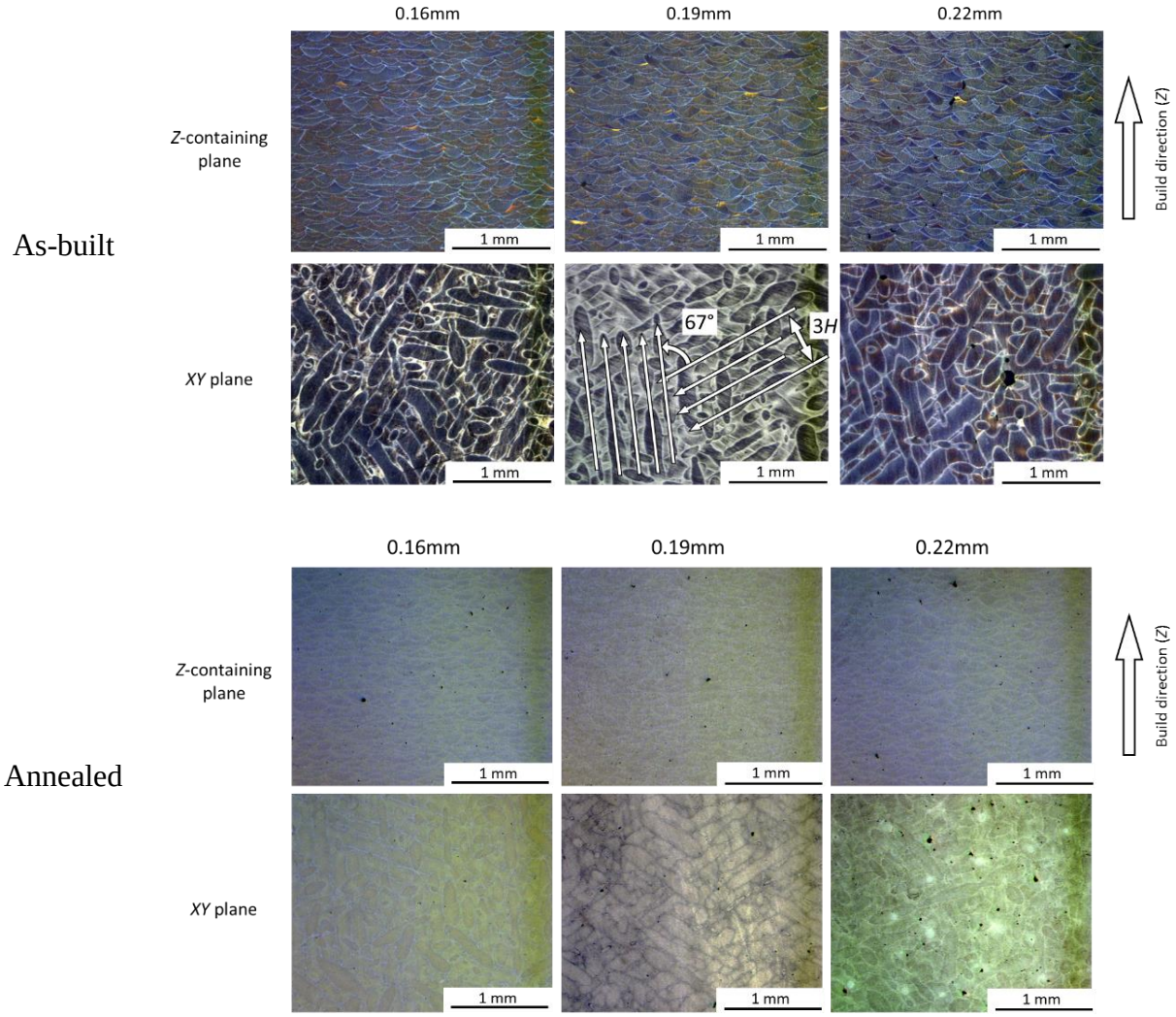

Figure 33. Optical micrographs of AlSi10Mg specimens with cross-sections along various planes after etching with Keller's reagent for 15 seconds.

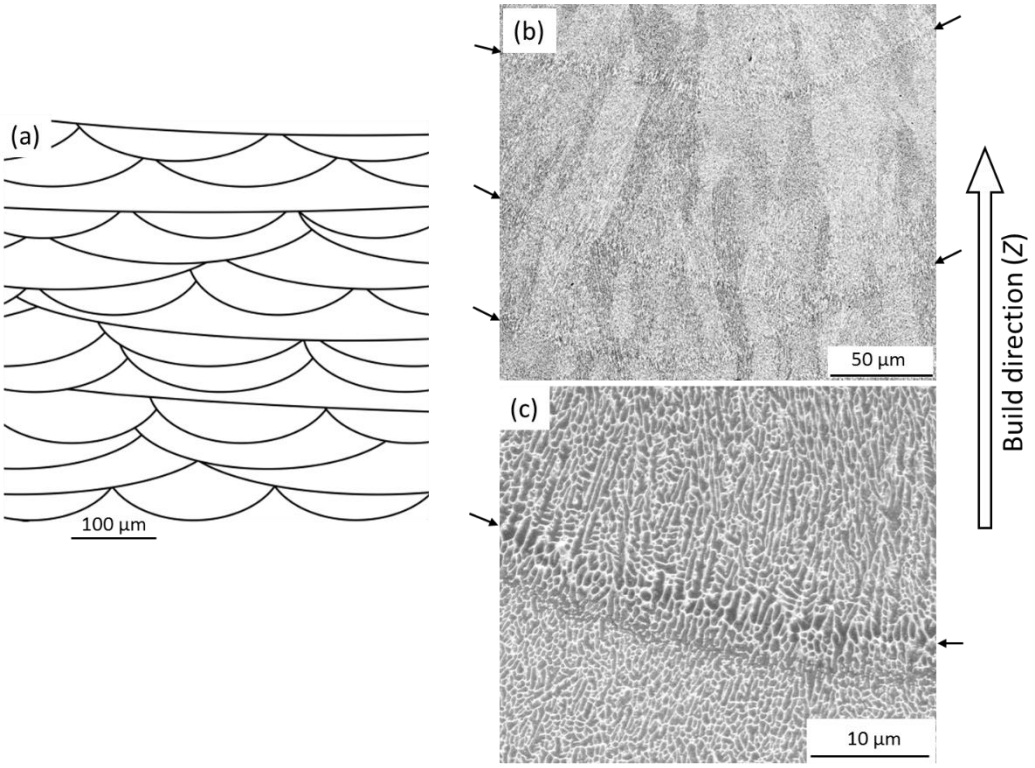

Figure 34. General features of solidified melt pools in built parts. (a) Simulated overlap between melt pools. (b) Backscattered electron micrograph with channeling contrast, showing epitaxial growth of grains from fusion line of the unetched sample. (c) Secondary electron image with a higher-magnification view of the region near fusion line of the etched sample, showing cellular growth. In (b) and (c), arrows indicate fusion lines (melt-pool boundaries).

Melt-pool dimension

Melt-pool dimensions were not only predicted by the Rosenthal equation, but also measured on the transverse cross-section of the top surface of the AlSi10Mg cylinders produced by EOS M280 in this work, with examples of the melt-pool dimension shown in Figure 35 and summarized in Table 15. Owing to the instability of melt pool, the melt-pool size is not consistent during the building process [52], [107], [158]. The processing parameters for the last three layers at the top surface are 360W beam power and 1.0m/s speed (slightly different from default values in Table 1). The standard deviation of melt-pool depth and width are based on measurements for more than 20 melt pools. Figure 36 depicts the width and depth for individual melt pools and histograms for these dimensions. The width and depth tend to be connected with a similar aspect ratio (D/W), falling in the range between 0.5 and 0.7. The deeper penetration (than the theoretically expected

D/*W*=0.5) may be caused by the relatively low speed when the melt pool becomes more prone to key-holing.

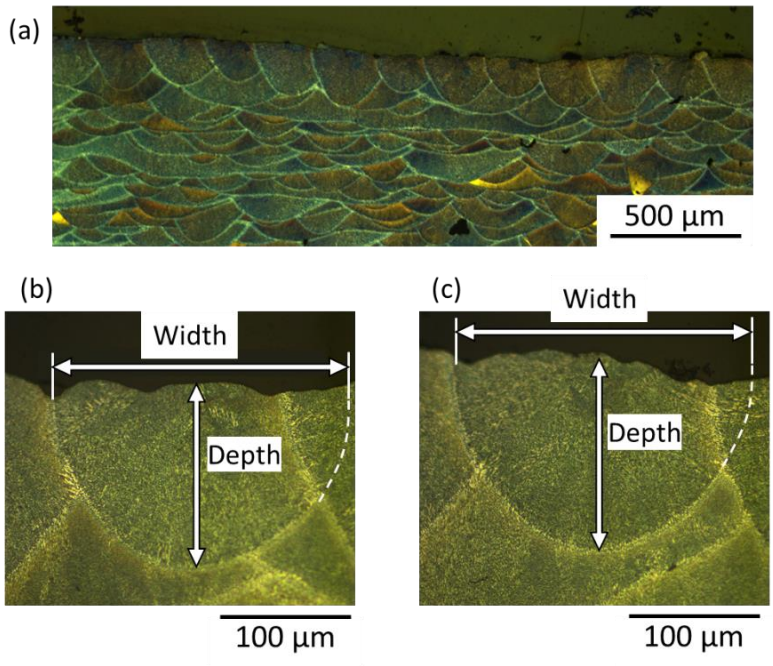

Figure 35. Optical micrographs of melt pools from the polished section perpendicular to the last laser travel direction on the top surface scanned with 360W beam power and 1.0m/s speed. (a) is an overview of melt pools, and (b) & (c) are two example sites for the dimension measurements on individual melt pools.

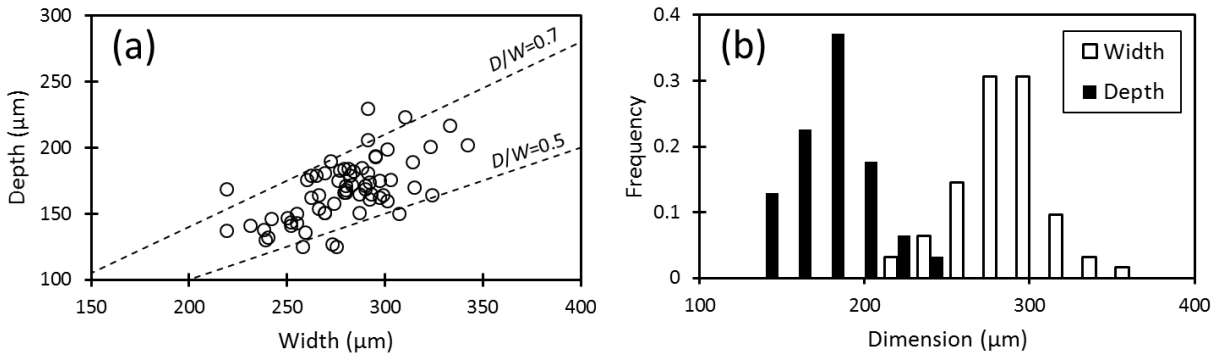

Figure 36. Melt-pool dimensions measured from the top surface. Dashed lines in (a) indicate the constant geometrical ratios between depth and width, and 0.5 refers to a semi-circular shape.

Table 15. Measurement of melt-pool geometry from AlSi10Mg cylinders fabricated by EOS M280, by using 360W beam power and 1.0m/s speed.

	Melt-pool width (μm)	Melt-pool depth (μm)
Average	278	168
Standard deviation	25	23
Relative standard deviation	0.09	0.14

Phase morphology

In this section, detailed morphology, composition and fraction of solidification phases in the cellular structure and the effect of heat treatment were studied [140].

Figure 37 reveals the binary solidification microstructure of cellular α-Al matrix decorated with brighter Si from the polished and etched cross-sections. The Si network exhibits a fibrous form in the as-built condition and is broken and spheroidized into islands after annealing at 300°C for 2 hours, as also observed in the literature [44]–[47]. In addition to the major phases of α-Al and Si, white particles tend to form inside α-Al, for both as-built and annealed samples; see Figure 38. These particles are likely precipitated Si which was originally retained in solid solution upon rapid solidification and precipitate out from α-Al afterward. Due to the limited build rate during the part fabrication, a specific location may remain at a relatively high temperature and allow some trapped Si to precipitate out. Intermetallic particles (such as Mg-rich and Fe-rich rod-like particles found on the powder surface) were not commonly observed on the polished sections of as-built and heat-treated samples, due to the limited concentration (as listed in Table 2). Even with a low accelerating voltage of 5kV during SEM, L peak of Fe was not readily found after analyzing multiple random spots, indicating the near-absence of intermetallic phases.

In the as-built sample, the cellular spacing was fine (less than 1μm), and its growth orientation appears to follow the heat extraction direction (as expected). Such a cellular microstructure driven by rapid solidification is as expected for laser remelting surfaces of near-eutectic Al-Si alloys [38], additive manufactured AlSi10Mg parts [28], [44], [159], [160] and Al-12Si components [32], [47], [161]. According to Aboulkhair et al. [159], rapid cooling after laser scanning reduces the amount of Si rejected into the liquid by extending the solubility of Si in Al, so α-Al solidifies first in the preferential cellular structure leaving the residual Si at the grain boundaries.

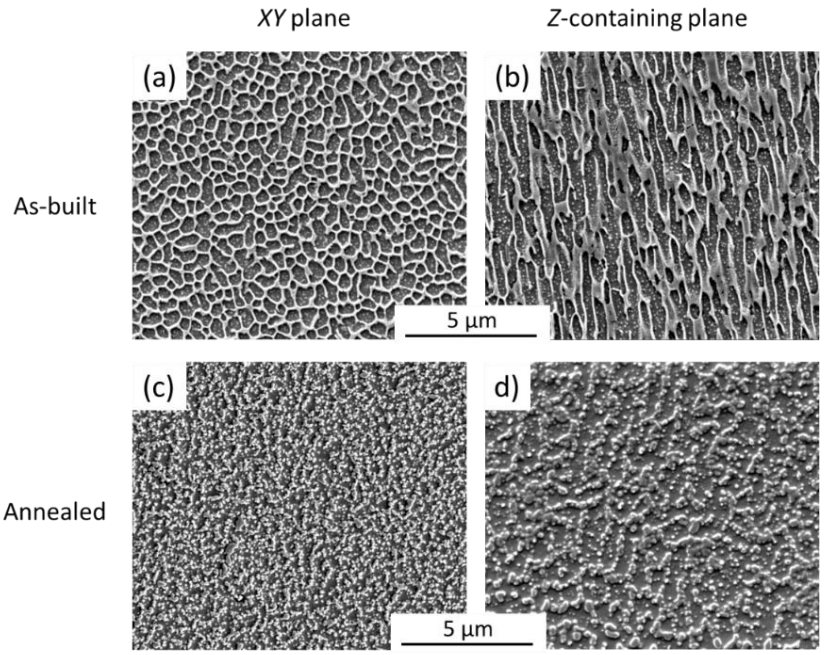

Figure 37. Secondary electron images of the cellular structure from different planes of as-built and heat-treated samples. Etched with Keller's reagent.

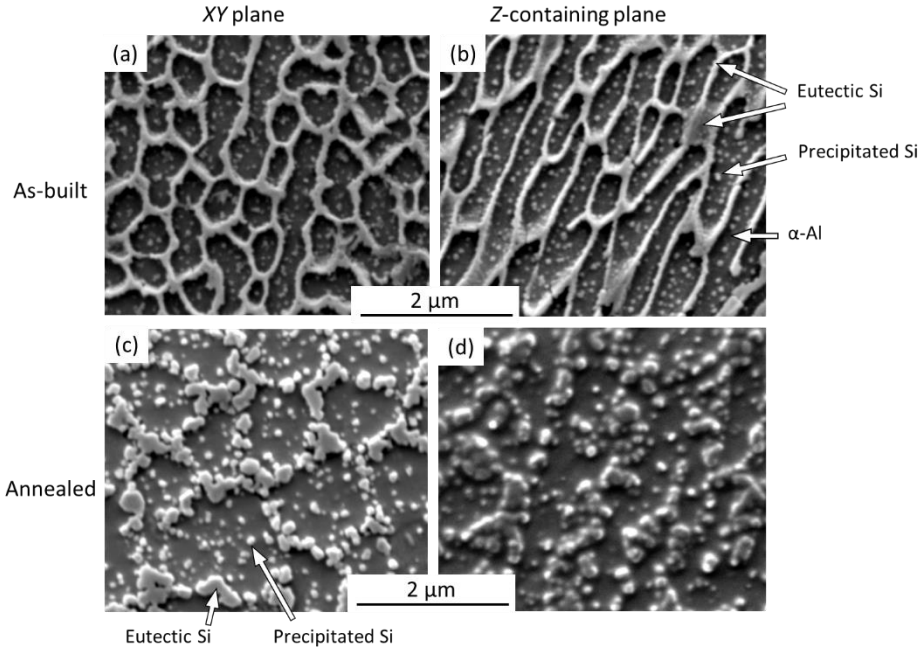

Figure 38. Detailed view of the precipitated Si particles from polished sections. Etched with Keller's reagent.

Phase composition

To further understand rapid solidification phenomena, it is essential to quantify the composition of phases, particularly dissolved Si in α-Al. Phase compositions were measured by two approaches: electrical conductivity on printed cylinders and EDS analysis on the polished section.

Table 16 shows the measured electrical conductivity and estimated weight fraction of dissolved Si, with Equation 15. It was found that roughly 4wt% Si was trapped in solution of as-built samples. Apparently, the experimental values in this work and 8.89 at% that obtained in the literature (corresponding to 9.19wt%, as reported for AlSi10Mg/SLM in Li et al. [44]) are very different; however, the trend of dissolved Si decreasing during annealing holds. Li et al. [44] utilized the shift of the α-Al peak in the XRD pattern to quantify the true lattice parameter and subsequently mass fraction of Si in α-Al. However, the lattice parameter of Al matrix could also be distorted by the residual stress in the as-built sample which arises during rapid solidification and cooling. According to the electrical conductivity analysis, most dissolved Si would precipitate out of solution during annealing at 300°C for 2 hours, which is in agreement with a negligible amount of solubility of Si in α-Al at 300°C at equilibrium (as shown in Figure 5).

Table 16. Electrical conductivity measurements for as-built and heat-treated cylinders.

	Conductivity (%IACS)		Weight fraction of Si (%)	
	Measurements	Averaged	In solution	As a separate phase
As-built	23.6, 23.7, 23.6	23.6	4.1	5.9
Annealed	44.9, 45.1, 44.8	44.9	0.3	9.7

Furthermore, the thermal conductivity (k) was estimated by the measured electrical conductivity (σ). The Wiedemann-Franz law was used for this conversion, as indicated below:

$$k = LT\sigma + C \qquad \text{Equation 26}$$

where L is the Lorentz number, T is the temperature in Kelvin, and C is the lattice thermal conductivity. The values used for L (2.1×10^{-8} W·Ω/K^2) and C (12.6 W/m·K) were taken from Ólafsson et al. [50]. Figure 39 shows a reasonable agreement between estimated thermal conductivity (from electrical results) and that reported in the EOS datasheet [29].

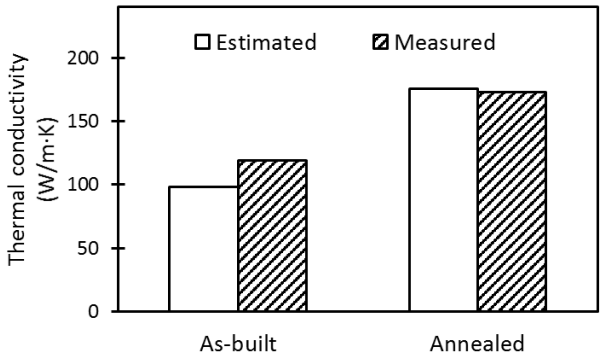

Figure 39. Comparison of thermal conductivities estimated from the electrical conductivity in this work and reported in the EOS datasheet [29].

With respect to the results from electrical conductivity, EDS indicates similar trapped Si (4.8wt%) in α-Al of the as-built sample, but an appreciably higher amount of Si (1.3wt%) remaining in the α-Al phase after annealing. One likely reason for the apparently higher dissolved Si after annealing is that Si would precipitate out as fine particles within the α-Al. This agrees with white Si particles observed in the heat-treated sample (as seen in Figure 38) and these fine precipitates would contribute to the measured Si peak during EDS.

Phase fraction

The last part of the phase analysis is the quantification of volume fractions. Two methods were applied: metallographic analysis from polished and etched planes, and estimation from phase compositions and mass balance.

A line intercept method similar to grain size measurement was applied on the polished sections, as shown in Figure 40 [162]. Care was taken during the sample preparation: as-built samples were only slightly etched for 3 seconds (as compared to 15 seconds suggested for conventional etching [108]), to minimize the stereological effect brought by the Si network protruding above the α-Al after etching. The resulting estimated overall volume fraction of Si is 12% for the as-built condition and 16% in the annealed sample, which correspond to 11% and 14% weight fractions, respectively. Both results overestimate the amount of Si, likely because the fine cellular structure and the edge effect from the thin Si fibrous structure (as seen from Figure 38b) make it challenging to achieve sufficient resolution to distinguish the boundary between phases and determine the width of Si fibers that intercept with the reference lines. Figure 40c highlights the precipitated Si particles

inside the α-Al cell that were estimated separately on the cross-section of the heat-treated sample. The precipitated Si accounts for around 4% volume fraction (equal to 3.4wt%) and approximately agrees with the amount of dissolved Si in α-Al in the as-built condition, as estimated by the electrical conductivity.

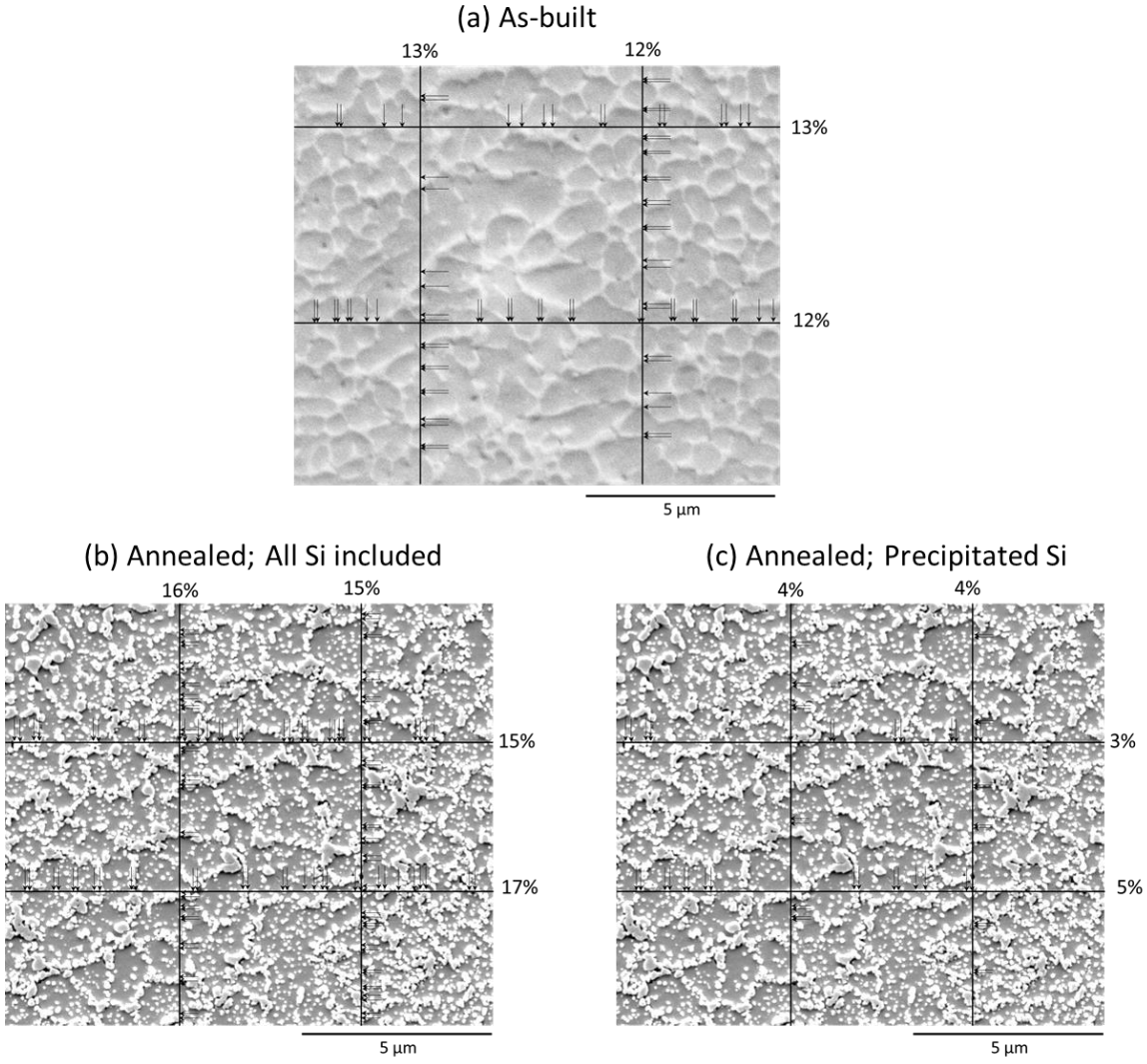

Figure 40. Linear intercept analysis to estimate the volume fraction of the Si phase. Arrows indicate the boundary between Si and α-Al cells. Top image: as-built; Bottom images: both heat-treated at 300°C, left-hand image marks all Si phases, and right-hand figure only highlights precipitated fine Si particles.

An alternative to estimate the phase fraction is to use the phase compositions measured from electrical conductivity and mass balance. The results of the α-Al composition estimated from electrical conductivity (Table 16) were utilized to quantify the volume fraction of phases. The mass balance of the phases and Si yields following equations:

$$W_1^{Si} V_1 \rho_1 + W_2^{Si} V_2 \rho_2 = W_{alloy}^{Si} \rho_{Alloy} \quad \text{Equation 27}$$

$$V_1 \rho_1 + V_2 \rho_2 = \rho_{Alloy} \quad \text{Equation 28}$$

where subscript 1 and 2 refers to the α-Al and Si phase, respectively, W^{Si} indicates the weight fraction of Si in different phases, V refers to the volume fraction of phases, and ρ indicates the density.

Combining the above two equations and canceling ρ_1 give

$$V_2 = \frac{W_{alloy}\rho_{alloy} - W_1 \rho_{alloy}}{W_2 \rho_2 - W_1 \rho_2} \quad \text{Equation 29}$$

Using the physical properties of phases in Table 7, the calculated volume fraction of Si is 7% in the as-built sample and 11% in the annealed condition, both slightly smaller than estimates from the polished plane by the line intercept method.

Table 17. Physical properties, weight fraction, and volume fraction of phases

Phase	Density (g/cm^3)	Mass fraction of Si		Volume fraction	
		As-built	Annealed	As-built	Annealed
α-Al	2.70	0.041*	0.003 *	0.93	0.89
Si	2.33	1	1	0.07	0.11
Alloy	2.67	0.1	0.1	1	1

* Estimated with the electrical conductivity; as shown in Table 16.

Cell size variation

Within a melt pool shown in Figure 34a, the cell size is expected to vary little, based on similar solidification times (see Figure 25b and Figure 41). In Figure 25b, the estimated liquidus-solidus solidification distances (in the direction of beam travel) are marked on the temperature profiles; the solidification time is equal to the solidification distance divided by the beam travel speed. Figure 41 shows the resulting expected variation of cooling rate across the width of the melt pool,

which was calculated for each radial position from the Rosenthal equation and using Equation 18 to predict the corresponding cell size.

Figure 42 demonstrates the evolution of the solidification microstructure across the melt pool as seen from various planes, and the observed solidification structure confirms that cell size varies little within the melt pool – apart from a coarsened structure along the melt-pool boundaries (shown by in Figure 42e), cell sizes appear uniform. Coarser cells along the melt-pool boundary are approximately 50% larger than internal cells, resulting from the slower cooling rate. Figure 42 also indicates the possible transition of the solidification mode from cellular morphology at the melt-pool center (Figure 42a) to dendritic growth at the melt-pool edge (Figure 42e), which supports the calculation of the decreasing cooling rate across the melt pool (Figure 41a).

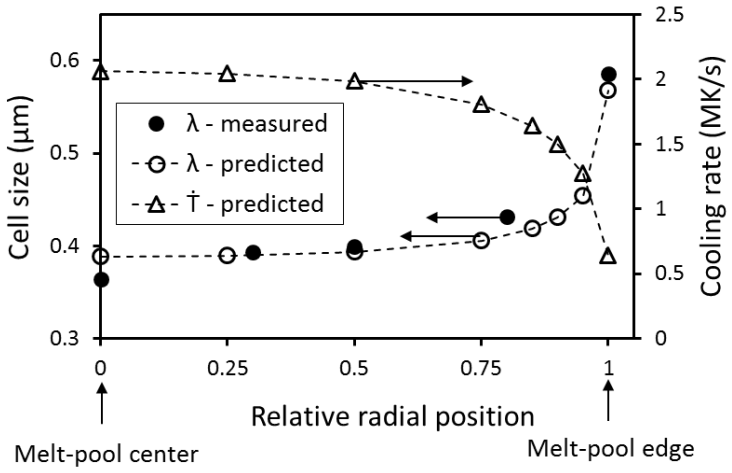

Figure 41. Predicted cooling rate ($\dot{T}$) and cell size (λ) across the width of the melt pool, and experimental measurements from the *YZ* plane in Figure 42(2a-2e). The sample top surface built with 360W power and 1.0m/s speed was considered.

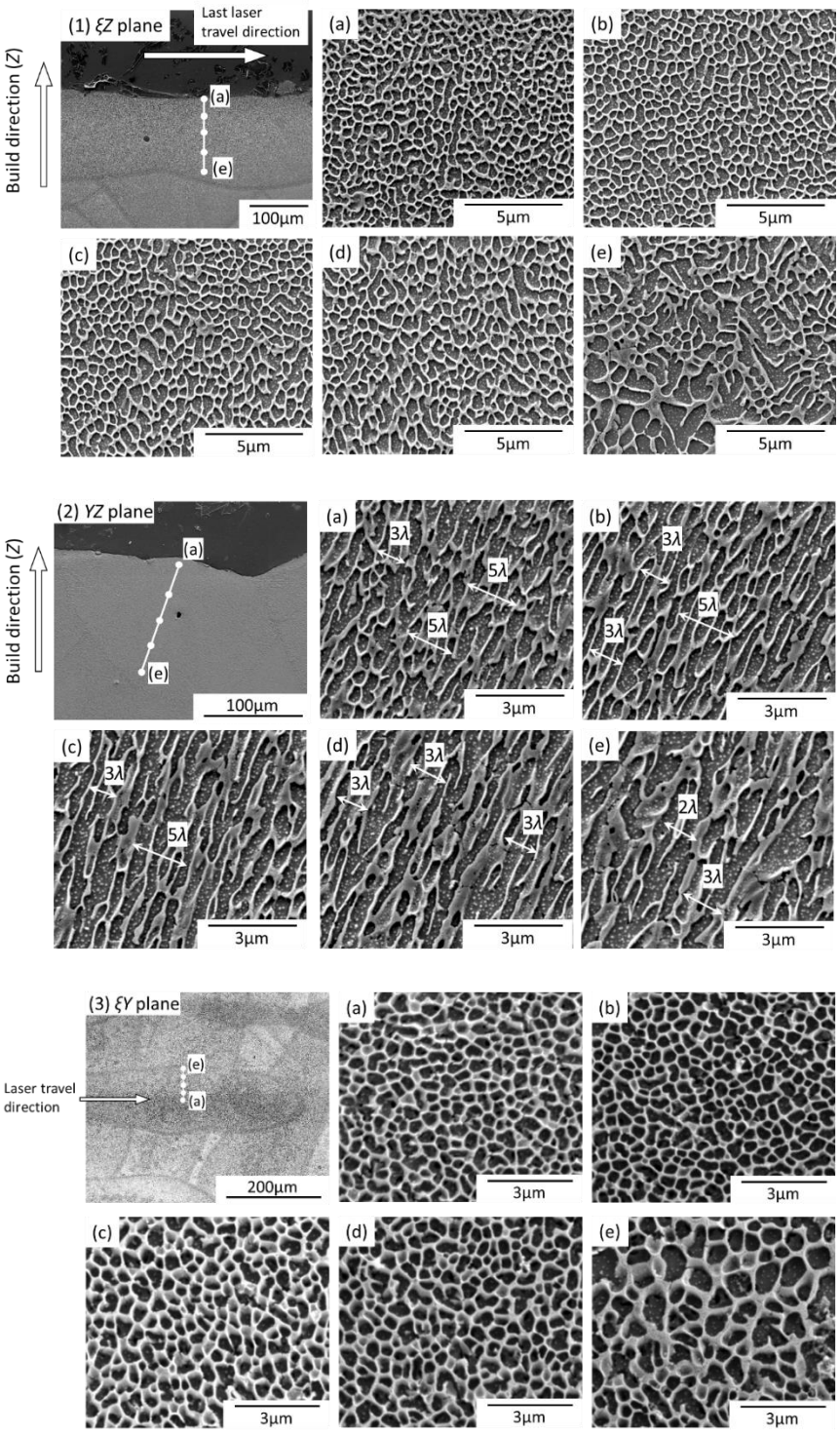

Figure 42. Secondary electron images showing the cellular structure evolution from the melt-pool center to the edge, as seen from various planes, as per Figure 21. (a) is from the center, (e) is at the edge, and the rest of the sites are approximately evenly distributed in between.

Cell size prediction

Despite the epitaxial growth of larger grains with approximately 10 μm wide, the strength of the material would be dominated by the much finer cellular structure of silicon precipitated within α-aluminum during solidification. For standard conditions, Equation 18 predicts cell sizes of approximately 0.4 μm at a cooling rate of approximate 2×10^6 K/s. For a range of processing conditions as tabulated in Table 8, the measured cell sizes and predicted cooling rates are listed in Table 18 and plotted in Figure 43. The trend of measured cell sizes in Figure 43 agrees with Equation 18, indicating that cell sizes do respond to variations in cooling rate as expected. This means that variations in heat input can be used to change cell sizes.

Table 18. Measured cell sizes and calculated cooling rates for conditions as listed in Table 8.

Case No	Power (W)	Velocity (m/s)	Measured cell size (μm)	Estimated cooling rate ($\times10^6$ K/s)
1	370	1.3	0.37	2.9
2	360	1.0	0.38	2.2
3	100	0.2	0.30	4.5
4	200	1.4	0.26	3.3
5	300	0.8	0.30	4.5
6	370	0.4	0.57	0.6

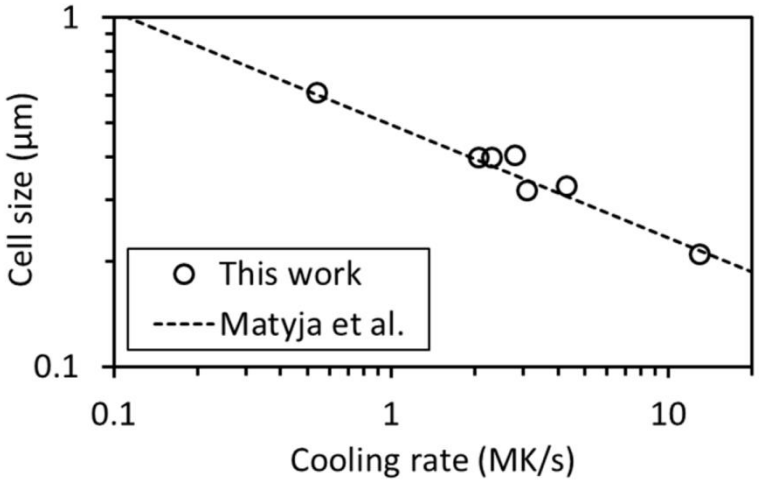

Figure 43. Comparison of measured cell spacings (data points; conditions as listed in Table 8) with expected spacings from literature correlation (broken line). Cooling rates were estimated with the Rosenthal expression.

Heat-affected zone

Figure 44 and Figure 45 show the transition regions in the vicinity of the melt-pool boundary in as-built and annealed samples. Four distinct zones are identified from all polished planes: the cellular structure remains fine in the major part inside the melt pool, becomes coarser at the boundary, tends to be finer again, and eventually disappears in the heat-affect zone by Si breaking into fine particles. The band of coarser cells is less than 5μm wide (viewed on the plane perpendicular to the laser scanning direction), small compared with the melt-pool width of 220μm [140]. Similar coarser cells at the melt-pool boundary of AlSi10Mg parts have been reported in the literature [24], [28], [60]. The coarser structure may form during slower cooling through the solidification range of melted material at the boundary [140], or because of reheating of the adjacent previously deposited solid to just below its melting point (similar to the heat-affected zone in fusion welds). The heat-affected zone is along the melt-pool boundary and characterized by coarsening of the silicon phase into idiomorphic particles, which may be caused by the increasing diffusion rate of silicon [28], [44]. However, it is still unclear why a finer zone is sandwiched between the coarser region and the outer heat-affect zone.

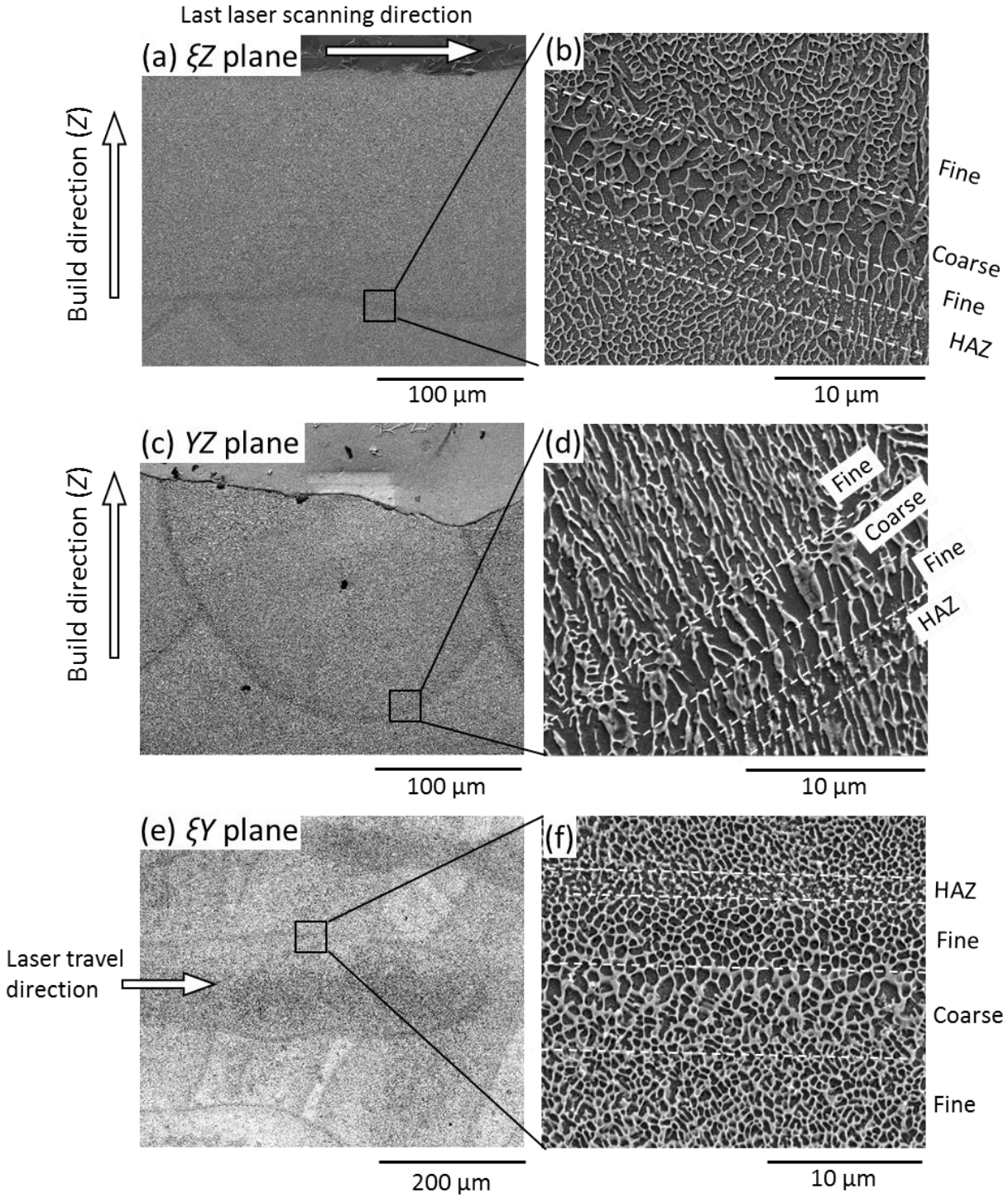

Figure 44. Secondary electron images of the microstructure near the melt-pool boundary in *as-built* samples. Notation of directions was available in Figure 21.

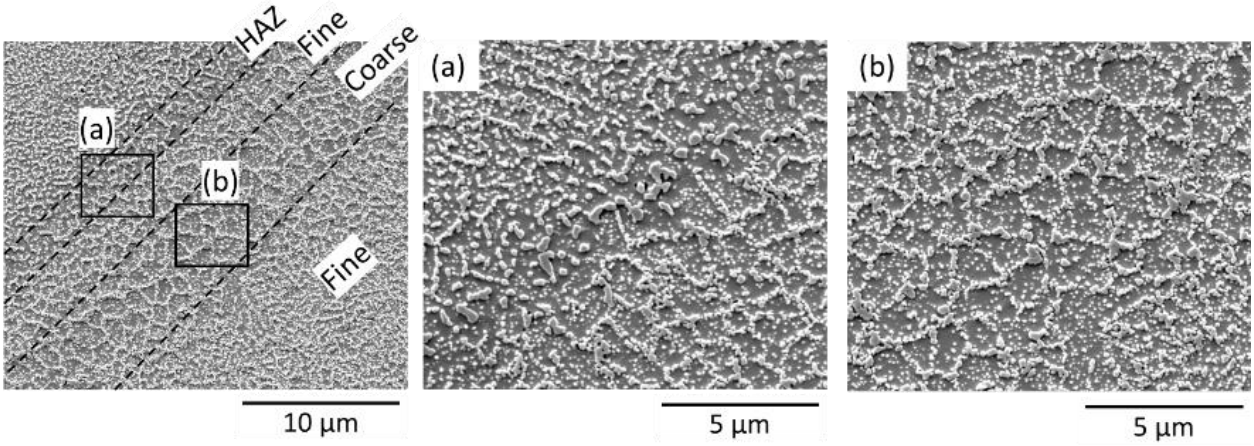

Figure 45. Secondary electron images of the microstructure near the melt-pool boundary and seen from *XY* plane in the *annealed* sample.

4.2 Tensile behavior

4.2.1 Summary of mechanical properties

Table 19 and Table 20 summarize the mechanical properties of specimens built in this work; the results are also presented and compared with literature data in Figure 46 - Figure 48. The yield strength of the additively manufactured components is a little higher than that of the conventionally cast components and with significantly larger tensile elongation (both likely reflecting the fine cellular microstructure of the SLM components [140]), with a somewhat lower tensile strength. A stress-relief heat treatment (300°C for 2h [29]) was applied after building. Since heat treatment would affect this comparison, the "quality index" for cast parts provides a consistent basis for comparison of static mechanical properties (strength and ductility). The quality index (*QI*) is defined as follows:

$$\mathrm{QI} = R_m + 150 \log e_f \qquad \text{Equation 30}$$

where R_m is the tensile strength (in MPa), and e_f is the tensile elongation (in percentage) [85]. Figure 49 shows that parts produced by SLM have a quality index in the range 450-500 MPa, which is similar to high-quality conventionally cast aluminum alloy parts [85].

Table 19. Summary of mechanical properties of specimens built under different conditions and with different orientations.

Group ID	Build direction	Hatch spacing	Strength		Elongation*		Area reduction*	Strain-hardening exponent **	Fatigue life at 100MPa***	Fatigue life at 80MPa***
			Yield	Tensile	Uniform	Total				
(-)	(-)	(mm)	(MPa)	(MPa)	(%)	(%)	(%)	(-)	($\log(N_f)$)	($\log(N_f)$)
A	*XY*	0.16	181	284	(-)	18	42	(-)	4.78	5.49
B	*XY*	0.19	182	285	6.1	18	41	0.12	4.74	5.35
C	*XY*	0.22	182	284	(-)	16	35	(-)	4.65	5.16
D	*Z*	0.16	177	285	5.8	15	32	0.16	4.65	5.27
E	*Z*	0.19	180	287	6.1	14	29	0.15	4.59	5.17
F	*Z*	0.22	180	287	6.1	14	27	0.14	4.51	5.06

* From tensile test

** Strain-hardening exponent estimated with data points from the start of plastic deformation to uniform strain, as per ASTM E646[163].

*** 100MPa and 80MPa are stress amplitudes, with R_{stress}=0.1; values in the table are averages of 4 specimens for each stress condition.

Table 20. Summary of fatigue lives of specimens built in this work.

Group ID	Fatigue life at 100MPa ($\times 10^3$ cycles)	Fatigue life at 80MPa ($\times 10^3$ cycles)
A	60, 46, 78 *	191, 348, 430, 307
B	52, 48, 59, 64	152, 235, 280, 245
C	46, 45, 42, 45	130, 143, 172, 142
D	53, 41, 41, 44	165, 210, 189, 186
E	34, 39, 39, 43	142, 121, 199, 135
F	31, 38, 32, 28	110, 120, 99, 137

* One fatigue test was interrupted at 86×10^3 cycles due to a power outage.

The fatigue behavior falls within the band of literature results for SLM parts produced with this alloy (Figure 47), indicating that similar-sized defects controlled the fatigue resistance of the parts manufactured in this work as in previous research. As discussed later in this work, porosity associated with oxides was found to control fatigue resistance of these samples.

Orientation during building and hatch spacing did affect both the static mechanical properties and fatigue behavior (Figure 48), with similar static strength but lower ductility (especially reduction in area) and lower fatigue life for samples prepared from vertically oriented cylinders (*Z*-oriented cylinders) and for samples built with larger hatch spacings.

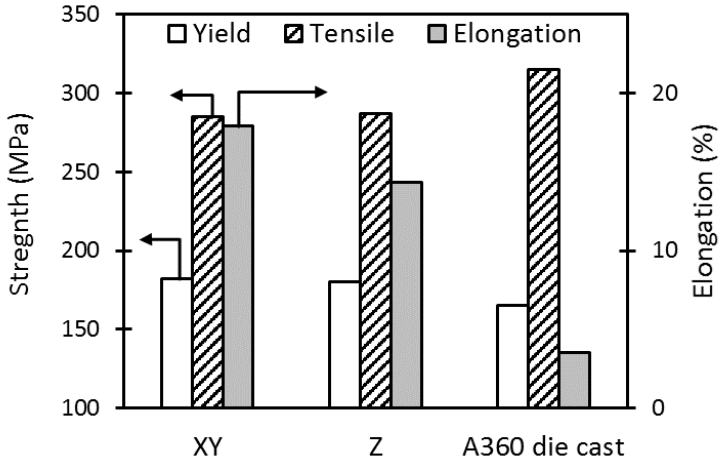

Figure 46. Comparison of tensile results of parts made by SLM (this work; standard hatch spacing of 0.19 mm) with die-cast aluminum alloy parts [62].

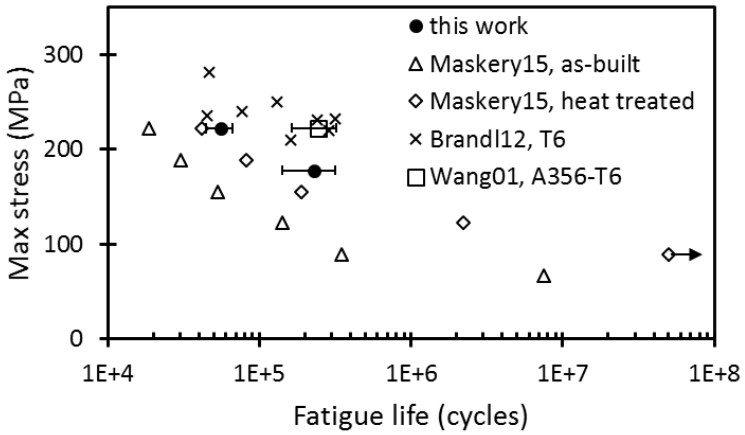

Figure 47. Fatigue resistance of AlSi10Mg specimens from this work (with standard hatch spacing of 0.19 mm and *XY*-oriented cylinder), compared with conventionally cast aluminum alloys (Wang01 [84]) and AlSi10Mg parts from literature (Maskery15 [58] and Brandl12 [45]). Horizontal error bars give 95% confidence intervals on the mean.

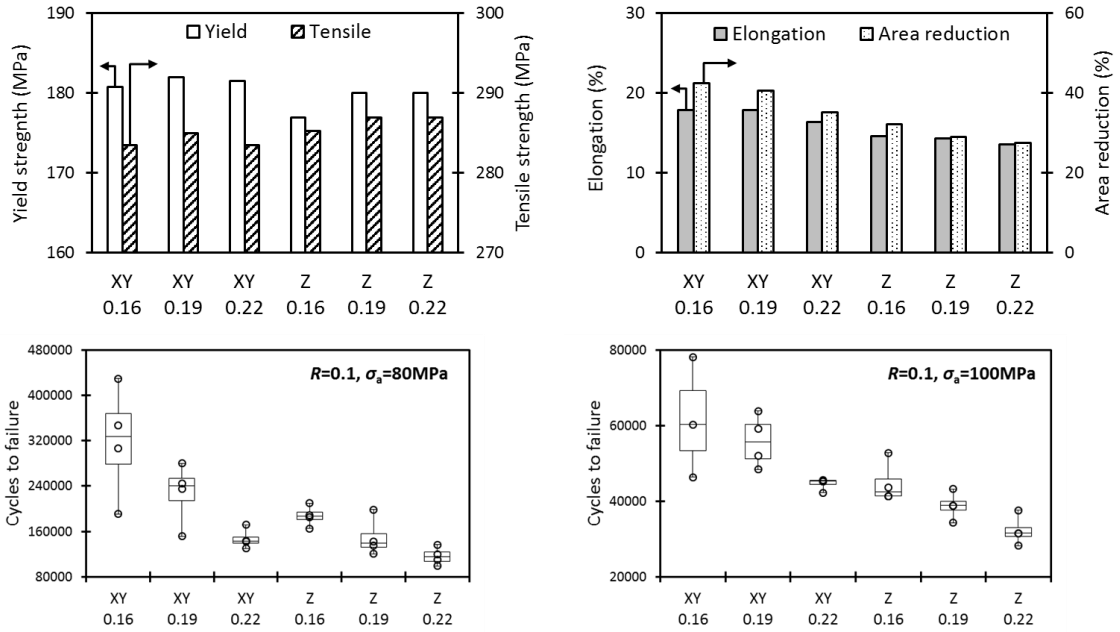

Figure 48. Effect build direction and hatch spacing on strength, ductility, and fatigue resistance. Units for hatch spacings are mm.

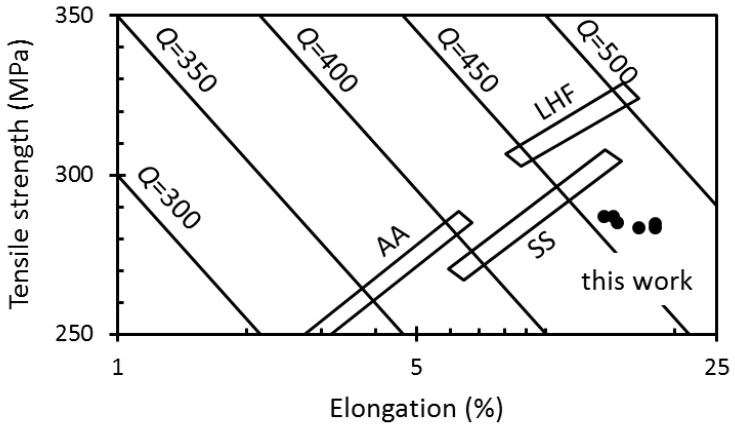

Figure 49. Comparison of the static mechanical properties of SLM AlSi10Mg parts (this work) compared with conventionally cast aluminum alloys, using the Quality Index (defined as $QI = R_m + 150 \log e_f$). AA, SS, and LHF refer to different casting producers; results for these reproduced with permission of Modern Casting [85].

4.2.2 Anisotropic ductility

The work reported in this section mainly investigated the effect of hatch spacing and build orientation on the tensile flow and work-hardening behavior of AlSi10Mg [164]. Table 19 summarizes the mechanical properties of the AlSi10Mg bars in this work; *XY* samples had notably higher ductility (elongation and reduction in area) than *Z* samples, but similar uniform strain: clearly the differences in tensile ductility arose after the start of necking (during non-uniform deformation).

Figure 50 below compares the engineering stress-strain curves of the additively manufactured AlSi10Mg parts. The tensile curves of the different AlSi10Mg samples appear to be largely consistent, for both *XY* and *Z* orientations. Such consistency is expected as the hatch spacing values were chosen to avoid lack-of-fusion porosity [165]. However, there are differences of detail, as discussed below.

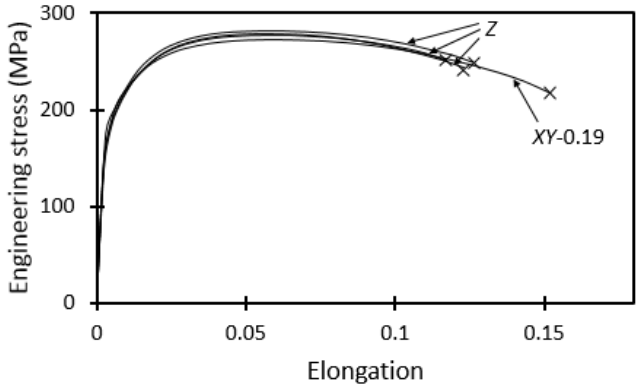

Figure 50. Engineering stress-strain curves of samples built in this work. Three *Z*-oriented samples built with different hatch spacings have a similar tensile behavior and are not distinguished in the figure.

As noted in Table 18 and Figure 46, *Z*-oriented samples had lower tensile ductility (most evident in the reduction of area) than *XY* samples, and those produced with larger hatch spacings had lower ductility. (In contrast, uniform tensile elongation was similar for all samples.) It appears that at least two microstructural features contributed to this effect of sample orientation and hatch spacing: coarser microstructure along the borders of melt pools (heat-affected zones), and porosity.

Details of the microstructure in the vicinity of the melt-pool boundary are shown in Figure 51; the coarser cells at the border are evident (see also in Figure 42). Such a coarsened structure of silicon precipitates in an aluminum matrix would be expected to have lower strength; previous work in which the structure of eutectic Al-Si alloys was refined by mechanical deformation showed that similar material with coarser silicon (in α-aluminum) had both lower strength and lower tensile ductility [166]. In this work, hardness tests confirmed that the part was softer in the coarser region at the melt-pool boundary (see Figure 51). Microhardness was measured with an MTS Nano Indentation XP instrument equipped with a Berkovich tip (TB22452-Berk), using an indentation depth of 800nm. The etched microstructures and indentations were examined by optical microscopy and scanning electron microscopy (SEM). Furthermore, the effect of heat treatment was also evident in the indentation results: the hardness significantly drops after annealing, particularly in the region with fine cells. Such a trend agrees with the coarsening of fibrous Si and precipitation of Si from solution, indicating strength loss by less solution hardening.

The lower strength of the annealed sample as compared to the as-built specimens agrees with the EOS datasheet [29].

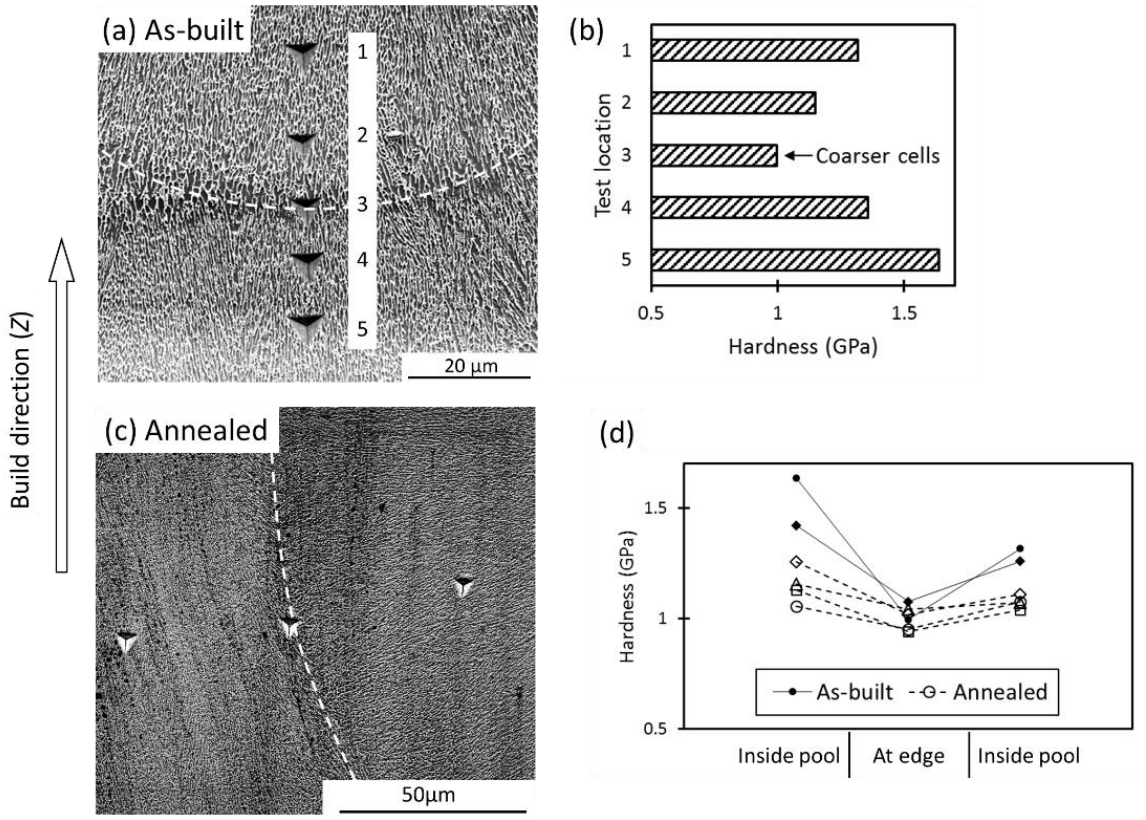

Figure 51. Hardness tests near the boundary of the melt-pool boundary, which is marked with a dashed line. The polishing plane contained the build direction as shown and was perpendicular to the laser scanning direction in this part of the sample. (a&c) Secondary electron image of the microstructure (cellular Si in a matrix of α-Al) in the vicinity of the melt-pool boundary, showing hardness measurement indentation marks. (b&d) Microhardness measurements at various locations.

Figure 52 demonstrates that the network of softer, less ductile melt-pool boundaries through the part did affect ductile failure of the samples in the tensile test: these typical fracture surfaces show tearing along the melt-pool boundaries for all the *Z*-oriented samples (especially so at the smallest hatch spacing). *XY*-oriented samples did not tear along the melt pool boundaries. Figure 53 illustrates the tearing behavior of *Z* samples schematically. To the best our knowledge, although

a few published papers have reported similar failure mode for *Z* samples [61], [167], [168], this is the first direct measurement of the weak layer along the melt-pool boundary, as supported by the micro-hardness measurement.

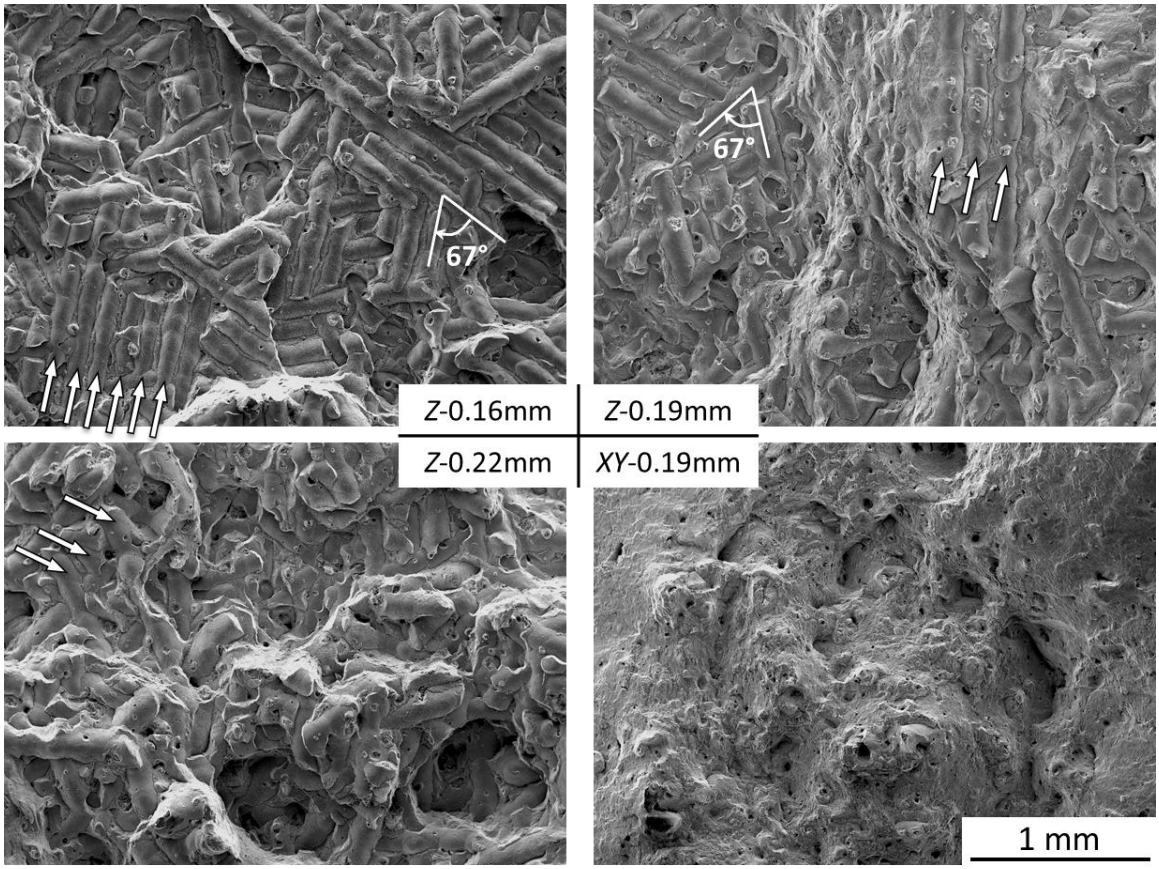

Figure 52. Fracture surfaces of AlSi10Mg tensile samples in this work. The arrows indicate the individual melt pools which are visible on the fracture surfaces.

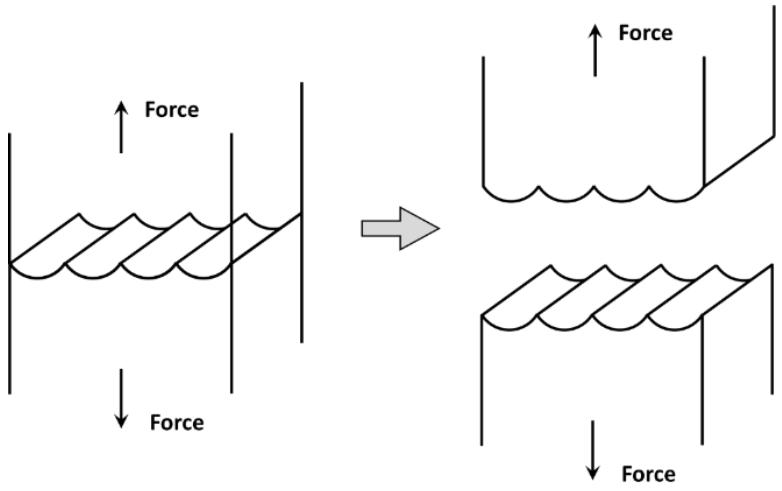

Figure 53. Schematic of the failure mode for *Z* samples. Adapted from Rosenthal et al. [168]

Figure 54 shows examples of the microvoids on the fracture surfaces; the spacing was measured using a line intercept method similar to grain size measurement [162], counting at least 100 intercepts along five lines. The average spacing was 0.39μm for an *XY* sample and 0.45μm for the matching *Z* sample built with the same hatch spacing. These are of the same order as the cell spacing inside the melt pool (around 0.40μm [140]), and coarser – as expected – for the *Z* sample which fractured along the coarser melt-pool boundaries. Fracture of the silicon particles at the center of the voids was not evident; rather, voids appear to have initiated at the silicon-aluminum interface.

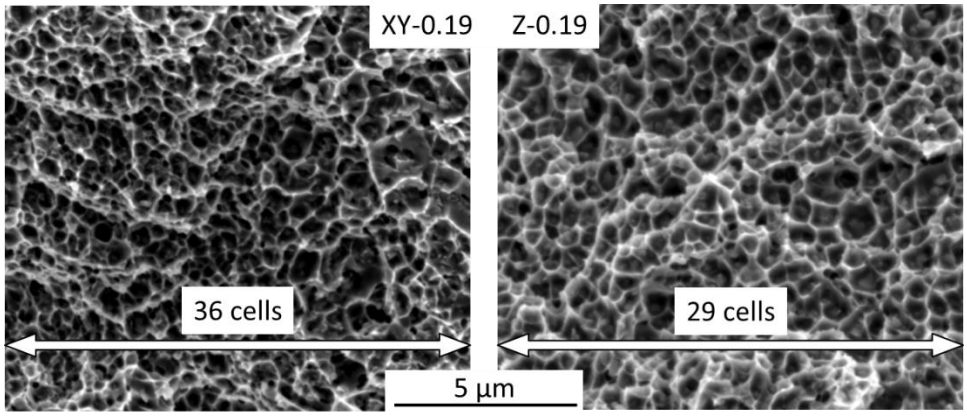

Figure 54. Microvoids on the fracture surface of printed samples.

The effect of hatch spacing on tearing along the melt pools for *Z*-oriented samples is evident in Figure 52, with the fracture surface more closely following the melt pool boundaries for the samples built with a smaller hatch spacing. This may result from a simple geometric effect (illustrated in Figure 55): for parts built with the smaller hatch spacings, the melt-pool boundaries would form a smoother plane of softer material (perpendicular to the sample drawing direction) through the part.

However, even though the fracture surface more closely followed the melt-pool boundaries for *Z*-oriented samples produced with smaller hatch spacings, these samples had better tensile ductility: their reduction in area was larger compared with *Z* samples built with larger hatch spacing (Table 19). The second microstructural feature contributing to this difference is pores in the samples. Pores are evident on the fracture surfaces (Figure 52); examples are shown at higher magnification in Figure 56. Even though building conditions were chosen to avoid lack-of-fusion pores, pores are present in the built parts; these are mostly associated with oxide particles and have been shown to affect fatigue resistance [165]. In fatigue tests on similar samples, parts built with smaller hatch spacings had improved fatigue resistance [165]; it appears that multiple cycles of remelting the part during building promote elimination of oxide-induced pores. A similar effect is evident in these ductility results: parts built with smaller hatch spacings (more remelting cycles) had larger tensile ductility.

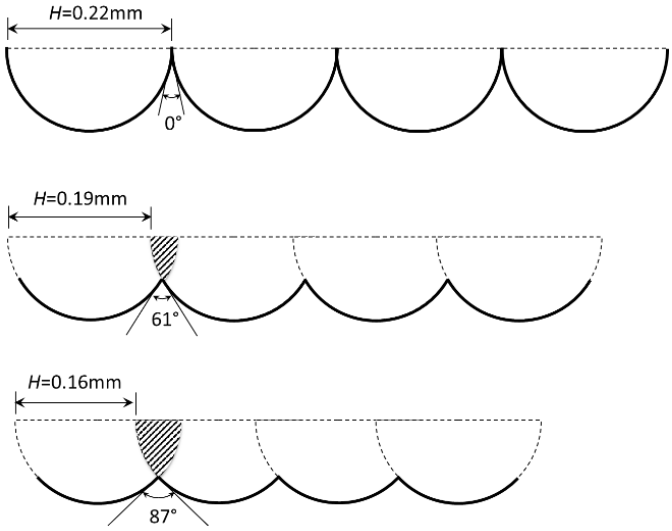

Figure 55. Schematic of overlap between adjacent melt pools for different hatch spacings. The melt-pool width is 0.22mm.

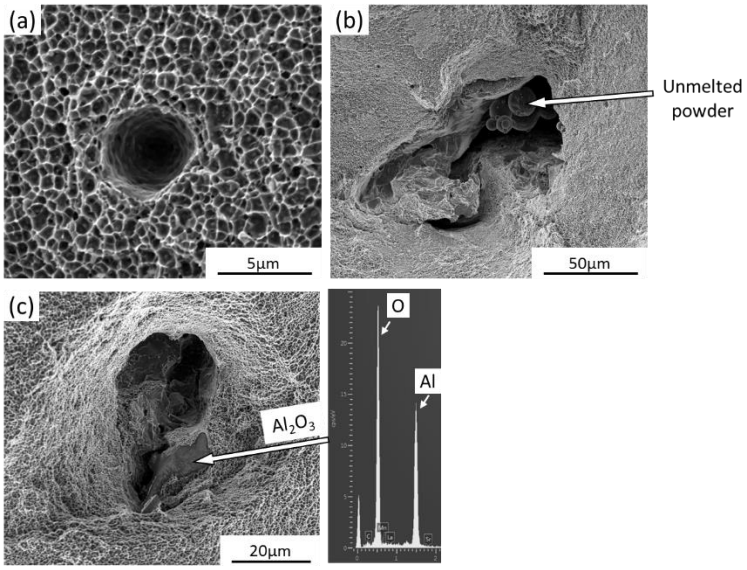

Figure 56. Typical defects on the tensile fracture surface of additively manufactured AlSi10Mg samples. (a) possible gas-driven porosity (based on the small size and round shape); (b) lack-of-fusion porosity (indicated by the unmelted powder particles; from *Z* sample built with 0.22mm hatch spacing); (c) oxide-induced porosity; EDS spectrum is shown at right, identifying the oxide as aluminum-rich.

4.2.3 Anisotropic elastic-plastic behavior

The region of the flow curve at low strains – which is important for fatigue resistance – shows consistent differences between *XY*-oriented and *Z*-oriented samples, see Figure 57. In this figure, the true stress is plotted against true plastic strain (true plastic strain was calculated by subtracting the elastic strain – calculated from the applied stress using an elastic modulus of 70 GPa). Evidently, plastic deformation of *XY* samples started at a substantially higher stress; the difference was approximately 25 MPa at a low plastic strain. The difference diminished at higher strains, but did result in a small but consistent difference in yield stress (measured at 0.2% plastic strain), with *Z*-oriented samples having a slightly lower yield stress (as also reported in [165]).

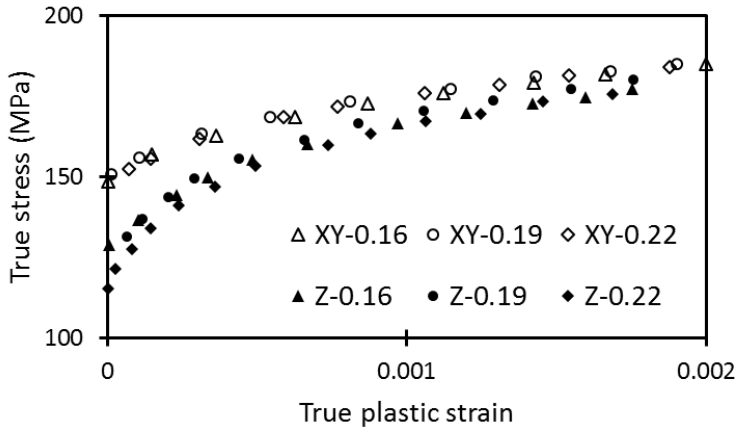

Figure 57. Effect of orientation on the stress-strain behavior at the start of plastic deformation.

This effect of sample orientation likely reflects the weak cube texture [28], of which one effect is that the silicon cells in the structure are approximately aligned with the *Z* direction. Heat treatment (at 300°C) after the build served to remove residual stresses that arose during part fabrication. However, the large difference in thermal expansion coefficient between silicon and aluminum is expected to lead subsequently to new microscopic thermal residual stresses parallel to the cells; the new residual stresses are expected to develop upon cooling the parts after the 300°C stress-relief treatment. During cooling, the higher thermal expansion coefficient of aluminum (than silicon) is expected to lead to residual tensile stress in the aluminum matrix. This is similar to what has been reported for composites of aluminum and silicon carbide (silicon carbide has a small

thermal expansion coefficient, similar to silicon); in the composites, the measured longitudinal tensile residual stress was 35 MPa for alloy 6061 containing 5% (by volume) of SiC whiskers [169]. The magnitude of the thermal stress in the AlSi10Mg parts was estimated by using the bulk material properties summarized in Table 21; note that the detail of the crystallographic orientation of the aluminum and silicon was not considered. For plane-stress conditions, and perfect bonding between the aluminum and silicon, the stress in the aluminum matrix is estimated as follows:

$$\sigma_{\mathrm{Al}} = \frac{E_{\mathrm{Al}}(T_1 - T_0)(\bar{\alpha}_{\mathrm{Si}} - \bar{\alpha}_{\mathrm{Al}})}{1 + \frac{f^V_{\mathrm{Al}}}{f^V_{\mathrm{Si}}}\frac{E_{\mathrm{Al}}}{E_{\mathrm{Si}}}} \qquad \text{Equation 31}$$

where E_i is the elastic modulus of phase i, $\bar{\alpha}$ is the average thermal expansion coefficient, f^V the volume fraction of the phase, and $(T_1\text{-}T_0)$ is the temperature change. Substitution of the material properties and a temperature change from 300°C to 20°C yields an estimated tensile stress of 75 MPa. This first-order estimate indicates that the thermal residual stress within the material is expected to be significant, if no micro-creep occurs during cooling of the parts after the stress-relief treatment. Such tensile residual stress may contribute to the observed lower fatigue resistance of *Z*-oriented samples (compared with *XY*-oriented samples) [165].

Table 21. Parameters used to estimate the thermal residual stress in AlSi10Mg sample [170], [171]

Properties	Al	Si
Density (kg/m³)	2699	2329
Elastic modulus (GPa)	70	112
Thermal expansion coefficient* (1/K)	25.5×10^{-6}	3.3×10^{-6}
Mass fraction	90	10
Volume fraction	88.6	11.4

*Average, for a temperature change from 20°C to 300°C.

The presence of micro-stress arising after annealing is further supported by the effect of cooling rate after stress relief (300°C for 2 hours). Figure 58 compares the flow curves for the fast-cooled (this work; air cool) and slow-cooled samples (Rosenthal et al. [168]; furnace cooling for 12 hours). Both sources used the same raw material (AlSi10Mg powder), machine (EOS M280) and post heat treatment (2 hours at 300°C). Figure 58 reveals that anisotropy in stress at the beginning of the

plastic deformation is much less obvious for slower cooling, which may allow time for the α-aluminum to creep to relieve the micro-scale stress.

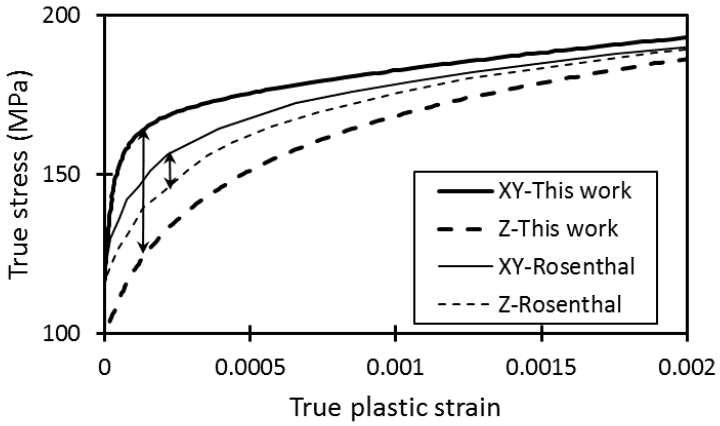

Figure 58. Effect of cooling rate after annealing at 300°C on the stress-strain behavior at the start of plastic deformation. Rosenthal et al. [168] utilized a furnace cooling from 300°C to 60°C for 12 hours, while samples in this work were air cooled.

4.2.4 Anisotropy of AM materials

Anisotropic mechanical properties of additive manufactured materials also show dependence on powder materials, manufacturing process, post heat treatment, and base-plate temperature. Figure 59 provides a summary of the reported directionality of the mechanical properties of metal samples fabricated by laser powder-bed fusion, showing the ratio of different mechanical properties for *XY* samples to that of *Z* samples. A ratio larger than 1 implies that *XY* samples are stronger, more ductile or stiffer; the figure also shows that in most cases properties are rather similar, with the most common difference in ductility. For AlSi10Mg alloy in Figure 59a, both base-plate heating during fabrication and post heat treatment would reduce the anisotropy in ductility, possibly caused by the Si phases coarsening and precipitation and hence less strength difference between the melt-pool center and boundary; as shown in Figure 51. However, Figure 59b indicates that parts built with other raw materials, including TiAl6V4, IN718, CoCr, and stainless steel, show different anisotropic mechanical properties: *XY* samples generally have slightly higher strength but substantially lower ductility. The higher fracture elongation of *Z*

samples of these alloys could result from the more textured microstructure, such as columnar prior-β grains parallel to the build direction [71]. All these alloys, except AlSi10Mg, have a relatively low thermal conductivity (Table 12) and hence an elongated melt pool with a relatively flat liquid-solid boundary will form (see melt-pool geometries of different materials in Figure 28). Such less curved boarder favors grains growing epitaxially and continuously along the *Z* direction across multiple layers. The boundary between these aligned grains may act as the weaker region and be prone to fail first when applying stress perpendicular to *Z* direction, corresponding to the failure mode of *XY* samples [71].

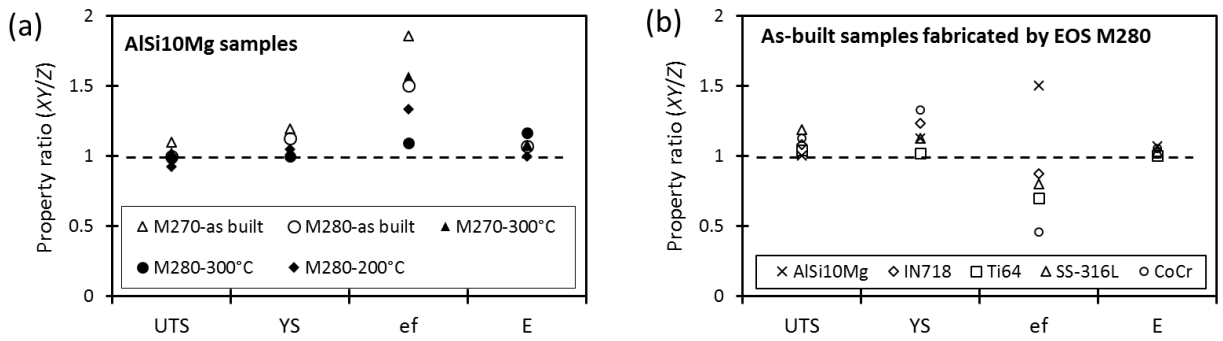

Figure 59. Anisotropic mechanical properties of the parts produced under different conditions [74], [125]. In (a), M270 and M280 refer to the EOS machine models, 300°C represents the post annealing process for 2 hours, and 200°C indicates the increased baseplate temperature during part manufacture. In (b), IN718 is a nickel-based alloy, Ti64 is a two-phase titanium alloy, SS-316L refers to a stainless steel, and CoCr is a Cobalt-Chrome alloy. UTS is the ultimate tensile stress, YS is the yield strength, e_f is the tensile elongation at failure, and *E* is the elastic modulus.

4.2.5 Work hardening behavior

Examples of fitted work-hardening, using the Hollomon and Kocks-Mecking/Voce equations, are given in Figure 60 and Figure 61; see also Table 19 for the fitted work-hardening exponents. In all cases, the linear Kocks-Mecking equation underestimated the work-hardening rate at low stress and strain, whereas the Hollomon equation overestimated the work-hardening rate at strains close to the uniform elongation. The Kocks-Mecking equation correctly predicts the true uniform strain (Figure 61(c)), whereas the true uniform strain is much smaller than the Hollomon work-hardening exponent in all cases (Figure 61(b); see also Table 19). Similar conclusions were reached for cast A357 samples [76]; Figure 62 shows that the relationship between the work-hardening exponent and yield strength for the additively manufactured samples tested is similar to the relationship reported for conventionally cast A357 samples.

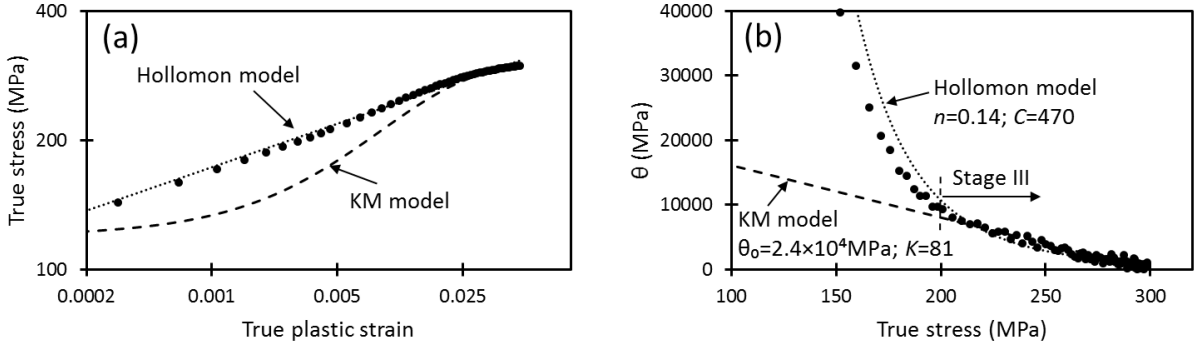

Figure 60. Examples of fitted Hollomon and Kocks-Mecking (KM) work-hardening equations (broken lines) to a true stress – true strain curve (points; an example is from group *E* of Table 19: *Z* orientation, 0.19mm hatch spacing).

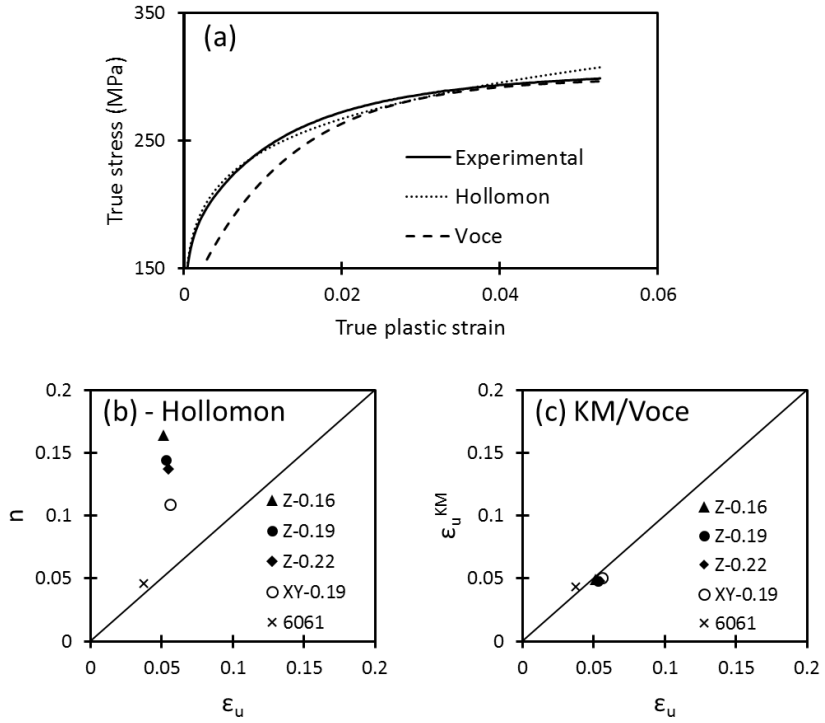

Figure 61. Comparison of agreement between fitted Hollomon and KM/Voce equations and (a) the stress-strain curve (the example is from E group of Table 19: *Z* orientation, 0.19mm hatch spacing) and (b&c) true uniform plastic strain.

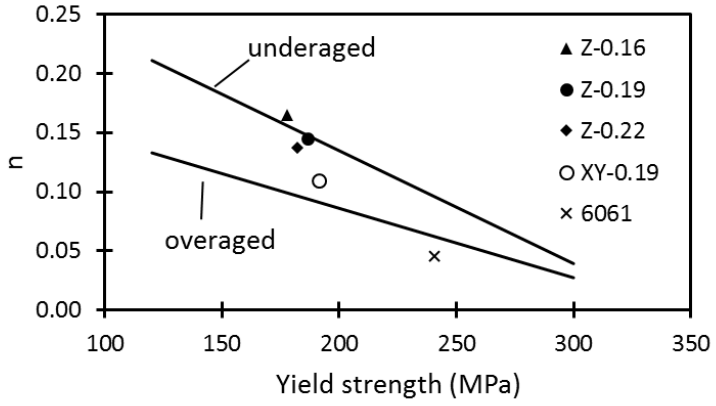

Figure 62. Comparison of work-hardening exponent and yield strength between samples tested in this work and cast A357(7%Si, 0.6%Mg) [76].

4.3 Fatigue behavior and defects

4.3.1 Effect of defects on fatigue resistance

In order to improve the fatigue behavior, it is essential to understand the origin of the defects. Typical defects, including porosity, oxide inclusions and unmelted powder (as found in various locations on polished cross-sections and the surface of as-built parts), are illustrated in Figure 63 to Figure 66.

Figure 63 highlights typical defects at the origin of fatigue cracks. These invariably included large oxides (several microns large) and associated porosity; in some cases what appeared to be unmelted powder was present. The more-detailed views of the morphology of oxide particles from fracture surfaces in Figure 64 show two main sizes: larger, micron-size oxides (likely associated with oxidized vapor or spatter, as discussed later), and much smaller, sub-micron oxides. The latter small oxides appear to originate from the native oxide film (expected to be around 3-4 nm thick [111]) of the powder particles, as seen from partially melted powder particles: upon melting of the powder, the native film apparently de-wets from the aluminum alloy, forming many small oxide particles (see Figure e & f). De-wetting of the oxide film from the aluminum alloy is expected, since the contact angle between hypo-eutectic Al-Si alloys and aluminum oxide is generally 90° or larger [172].

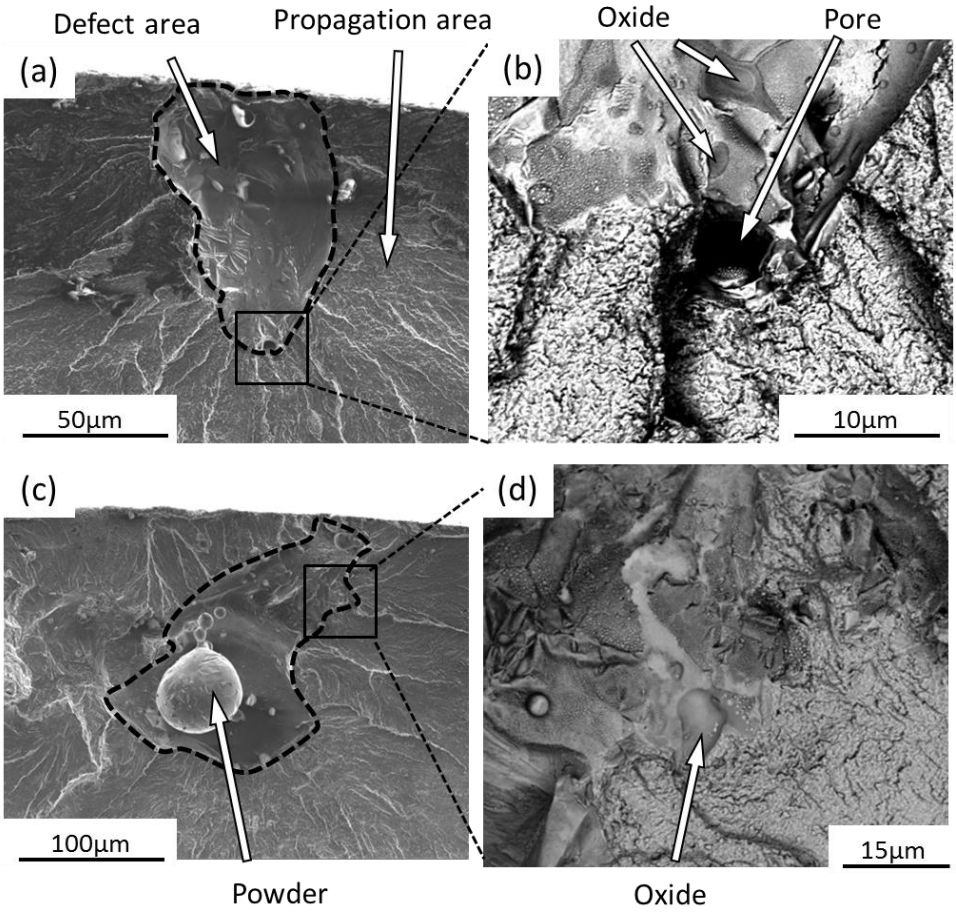

Figure 63. Scanning electron images of typical fracture surfaces after fatigue tests with various magnifications. (a&c) Secondary electron images for an overview of defect areas. (b&d) Backscattered electron images for a detailed view of the pore and oxide at the boundary between defect area and crack propagation region.

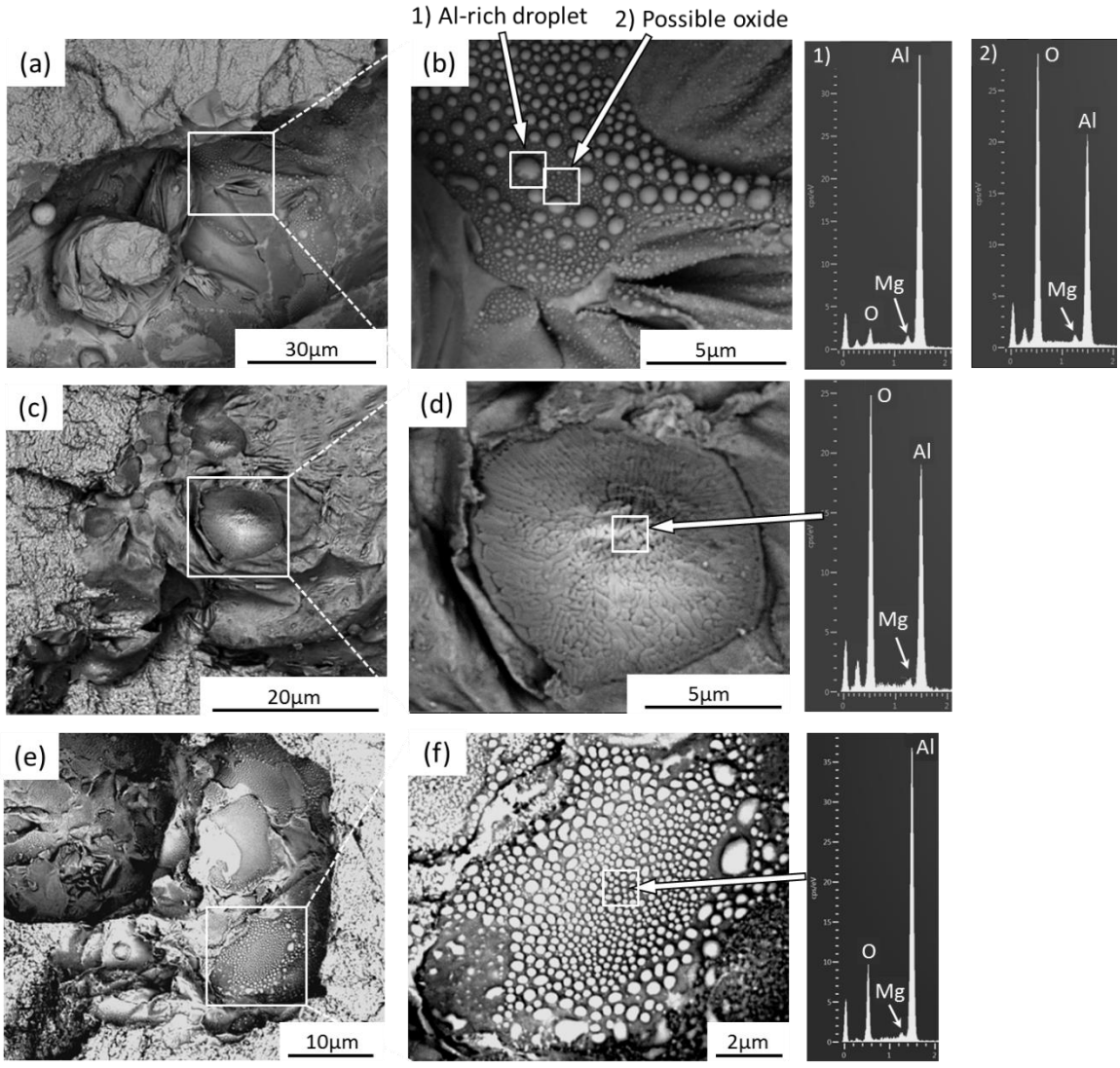

Figure 64. Backscattered electron images of oxide particles at the border between defect area and crack propagation region. An overview at lower magnification is given in left-hand images (a, c, and e), and detailed surface morphology in right-hand images (b, d, and f). Typical EDS spectra at right show the presence of Al and Mg in oxide particles.

Of the two sizes of oxides, the larger particles showed a consistent association with larger pores (several microns to tens of microns large) as seen on polished cross-sections; see Figure 65 for examples. In most case where large pores were found on cross-sections, associated large (micron-sized) oxides were also found; this correlation was also supported by the porosity quantification by automated SEM of polished sections: the 30 largest pores in the sample built with the standard hatch spacing (0.19mm) are mostly connected to oxide particles (as summarized in Table 29 in Appendix B). A likely mechanism by which oxide particles can cause porosity is that the molten aluminum alloy does not wet the oxides; the oxide particles prevent the consolidation of the molten alloy. Such an effect of oxides (causing poor consolidation) was previously noted in parts produced by selective laser melting of aluminum alloy powder [173].

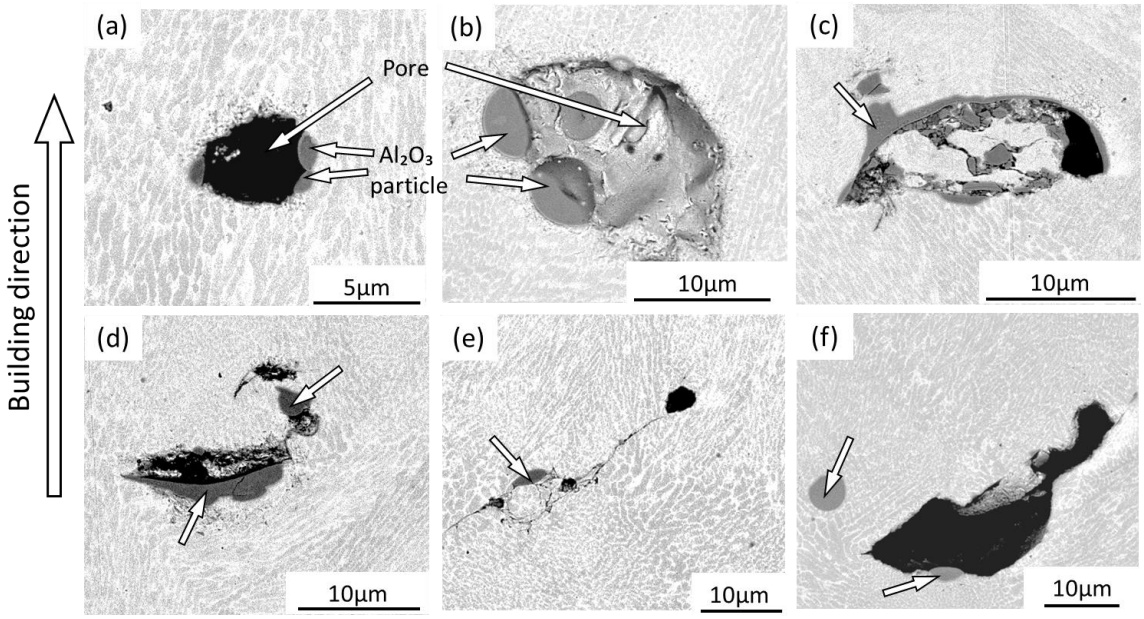

Figure 65. Backscattered electron images of porosity and associated oxide particles on polished cross-sections of as-built specimens. Most oxide particles are associated with porosity and located at the pore boundary (a,b,c,d) or connected with a lap (e); some are present as isolated particles (f).

Further observations which point to the origin of the larger oxides are that the oxides are more evident on the upper (last-melted) surface of the built parts (Figure 66) and that the large oxides have a significant magnesium content, much higher than in the alloy itself (Figure 64). From image

analysis, the large oxides cover approximately 7% of the top surface of the built part, much higher than expected from the volume fraction of these oxides: as noted earlier, the total oxygen concentration in the parts is around 400 ppm by mass, implying a total oxide concentration of around 0.08%; the volume percentage of oxides (equal to the oxide area fraction on a random plane through the part volume) would be slightly lower than this, given that the oxides are denser than the alloy (the density of Al_2O_3 is approximately 4.0 g/cm^3, and that of $MgAl_2O_4$ 3.6 g/cm^3).

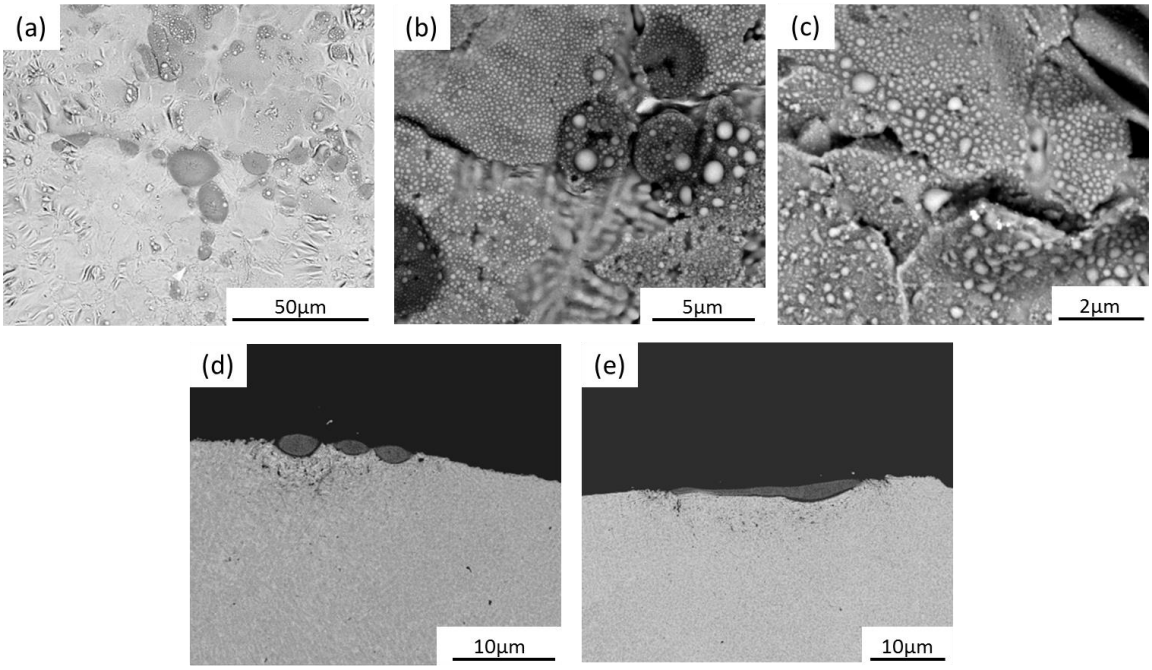

Figure 66. Backscattered electron images of the top surface of the as-built part. Oxide particles appear darker than metal. Top views are given in (a, b and c), and side views (polished cross-section, with polishing plane parallel to build direction) in d and e.

The elevated magnesium content indicates that these oxides may have formed by oxidation of metal vapor which is produced in the high-temperature region below the laser beam and which is enriched in magnesium; Figure 67 illustrates the elevated vapor pressure of Mg compared with Al, and the much-lower vapor pressure of Si. From these observations and calculations, a likely mechanism for the formation of the large magnesium-rich oxides is that these are vaporized alloy which was oxidized by residual oxygen in the argon atmosphere.

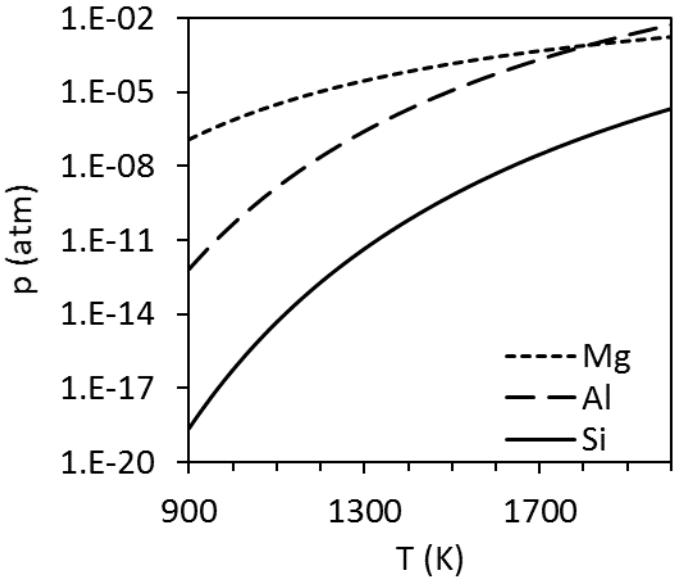

Figure 67. Calculated partial pressures of Mg, Al, and Si in equilibrium with an Al-10%Si-0.5%Mg alloy at different temperatures. Partial pressures were calculated from activities of species as found with Thermo-Calc using the alloy database TCAL4.

4.3.2 Defect quantification

Porosity

The approaches to quantify pores and oxides, used in this work, are summarized in Table 22 and graphically illustrated in Figure 68 to Figure 73. As mentioned before, Archimedes method gives global densities with limited accuracy.

Table 22. Summary of defects examined by different approaches.

Hatch (mm)	Pore			Oxide			
	f_{area}	f_{volume}	f_{volume}	f_{area}	W_O (ppm)	W_O (ppm)	W_O (ppm)
	2D-SEM	3D-CT	Archimedes	2D-SEM	2D-SEM	Bulk analysis	Oxide Film
0.16	0.042%	0.020%	< 1%	0.024%	101	290	399
0.19	0.053%	0.066%	< 1%	0.035%	159	360*	399
0.22	0.147%	0.219%	< 1%	0.045%	233	460	399

* This is the average value based on two measurements in Table 11.

Figure 68 compares the volume fractions of pores estimated by 2D SEM and 3D CT. The total fractions of pores from the two methods should be equal, since the area fraction on a random plane through the part volume is equal to the overall volume fraction. Figure 68 reveals a slight difference which may arise from somewhat limited analysis area in 2D analysis and volume in 3D study. However, a similar trend is evident: a larger hatch spacing leads to a larger porosity volume fraction, in line with the observation that a smaller hatch spacing gives better fatigue results. The dependence of porosity on the hatch spacing may result from a beneficial effect of multiple melting cycles on promoting consolidation (eliminating porosity); as noted earlier, for the smallest hatch spacing used in this work, each volume in the part was on average melted 4 times, whereas with the largest hatch spacing each volume was melted on average 2.9 times. Generally, repeated melting tends to reduce both oxide-driven and lack-of-fusion pores, which were both present in the samples studied in this work. Moving beyond this speculative explanation to quantitative prediction of oxide-driven porosity would require detailed mechanistic information on the rate of production of large oxides, possible removal of oxides from the top surface by the recoater bar (between layers), and improved consolidation upon repeated melting [174].

Figure 68 also indicates similar porosity volume fractions for the two smaller hatch spacings but substantially higher for the large hatch spacing. As mentioned earlier, the two smaller spacings satisfied the criterion for full melting, while the largest hatch spacing would introducing lack-of-fusion porosity, which could contribute to the steep increase of the porosity fraction. The predicted volume fraction of lack-of-fusion pores (0.02%) is smaller than the large difference as observed in Figure 68 (around 0.10 to 0.15%). This underestimation of unmelted regions could have resulted from ignoring varying melt-pool dimensions during part manufacture.

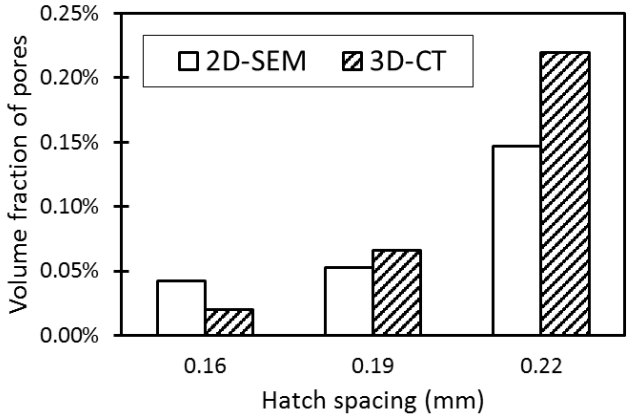

Figure 68. Volume fractions of the porosity estimated by 2D SEM and 3D CT for *Z* cylinders built with different hatch spacings.

Figure 69 illustrates a possible mechanism behind the effect of hatch spacing on the amount of larger oxides: the removal of the oxide particles by the recoating blade, particularly when the oxide particle size is comparable to the layer thickness (30μm in this work) [174]. The valley between the caps of adjacent melt pools could shield oxide particles from being removed by the recoating blade. With a larger hatch spacing, this valley becomes deeper and hence more oxides would be left in parts. This argument could be further tested in future work by analyzing the location distribution of oxide particles on the last solidified surface (more oxides at the intersection between melt pools), as well as the effect of layer thickness on the oxygen concentration (an increasing layer thickness would imply a high cap, possibly affecting oxide removal).

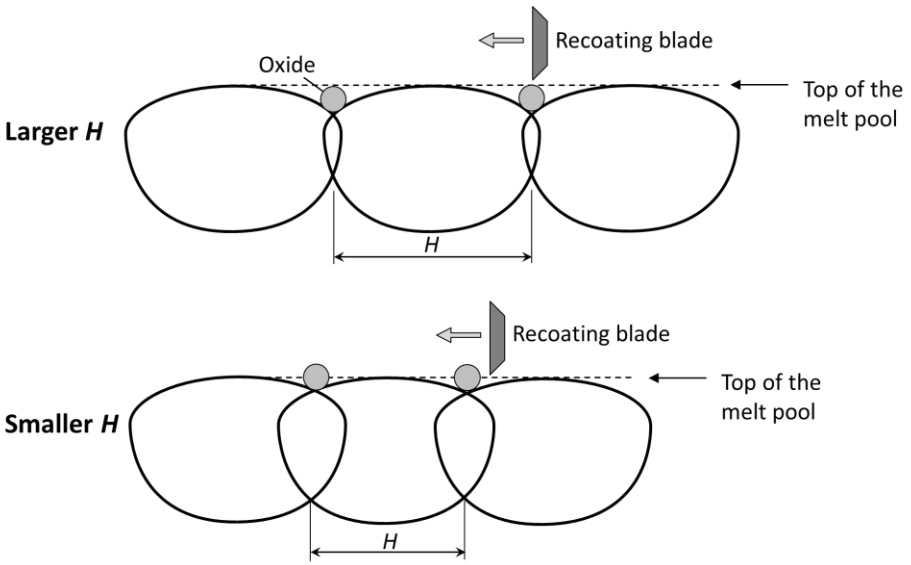

Figure 69. Schematic showing the effect of hatch spacing on the surface morphology and proposed removal of attached oxide particles by the recoating blade [174].

Figure 70 reveals the detailed distribution and cumulative fractions of pores as measured by 2D SEM and 3D CT. Pore sizes are defined as the equivalent circular diameter from the defect area in 2D, and the equivalent spherical diameter from the volume of the feature in 3D, respectively. The lower threshold of feature dimensions was set as 3.6μm for 2D SEM and 3.0μm for 3D CT, to exclude possible noise during the feature detection.

The histograms in Figure 70(a)&(b) give a similar trend of more large pores (larger than 15μm) for the greater hatch spacing, which is caused by the expected lack-of-fusion porosity. However, within the range of a small pore diameter (less than 10μm), analysis of the sample built with the smaller hatch spacing shows more pores (compared with the other builds) by 2D analysis but 3D indicates less. Either trend could be explained by the effect of remelting to reduce both oxide-driven and lack-of-fusion pores: a smaller hatch spacing introduces more melting cycles and could eliminate these pores, decreasing the whole porosity population, as indicated by the 3D results. However, if remelting does not diminish the previous pores completely but only reduce their size, a greater number of small pores would be found, as shown by the 2D results. To justify these opposing effects, detailed examination on the correctness of individual features and stereological study for a direct comparison between 2D and 3D results would be helpful. However, the larger pores are more relevant to the fatigue behavior.

The cumulative size distributions in Figure 70(c)&(d) show a similar effect of the hatching spacing on the porosity, as illustrated by the histograms, but also highlight the remarkable contribution of large pores (diameter larger than 40μm) to the total pore volume fraction for the largest hatch spacing. These larger pores are similar in size to the melt pool (around 100μm deep) and likely lack-of-fusion pores.

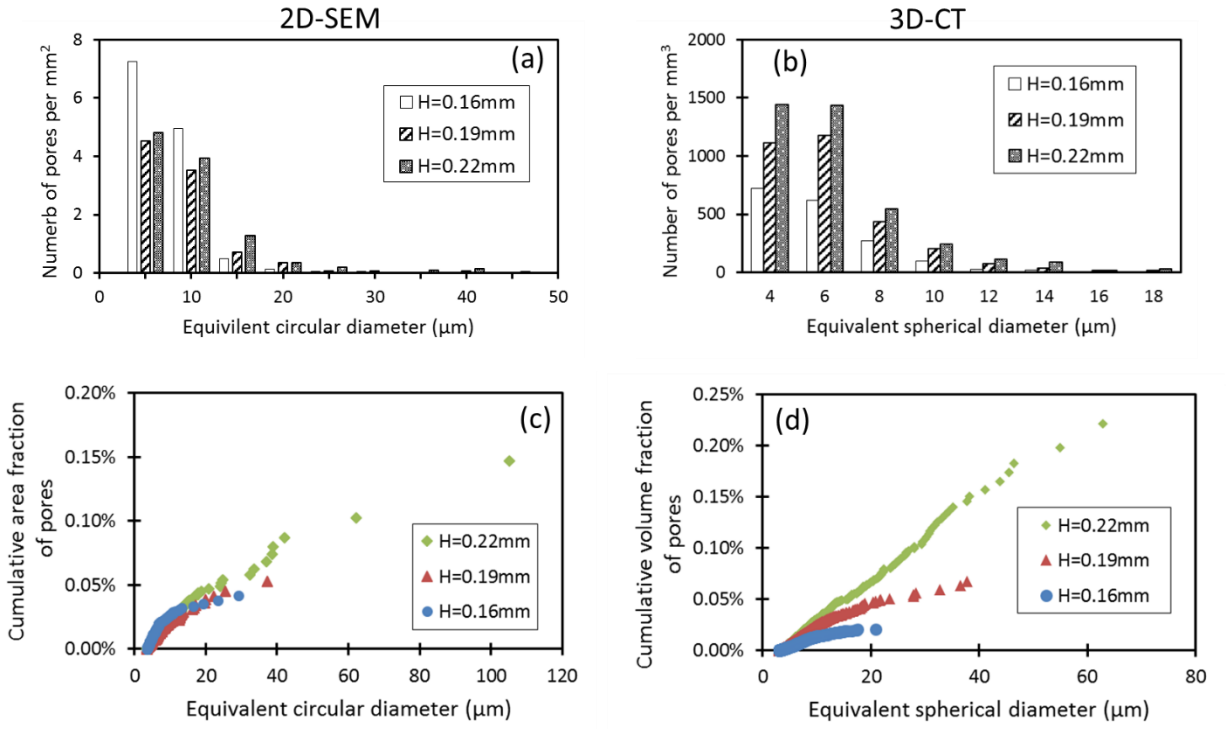

Figure 70. Histograms (a&b) and cumulative distributions (c&d) of pores. Left-hand plots are from measurements on a polished plane and right-hand figures are from 3D tomography results.

Figure 71 depicts the histogram of pore orientations measured from the polished section that contained the *Z* direction. The angle reported is between the longest chord of pores and the *XY* plane. It can be seen that more pores tend to align with the *XY* plane (lower angles) than parallel to the *Z* direction (90°). This explains the lower fatigue lives of *Z*-oriented samples, with larger effective pore sizes perpendicular to the stress direction.

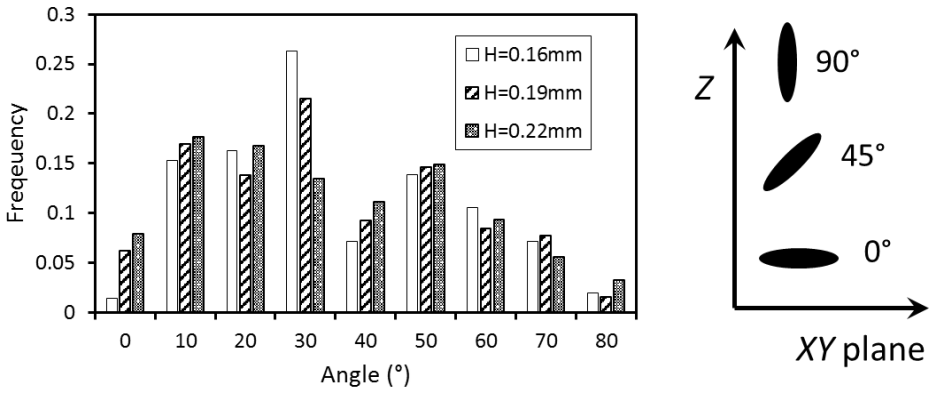

Figure 71. Histogram of pore directions measured on polished planes. Angle is between the longest chord of pores and the *XY* plane.

Figure 72 shows the variation of the aspect ratio and angle of pores measured on the polished planes. The aspect ratio is defined as the ratio between the length of the longest chords though the feature centroid and the length of the chord perpendicular to the longest chord. The measured data points were divided into four groups by the diameter size. Figure 72 reveals that the aspect ratios of the pores span quite a wide range (as large as 10). The pore size does not have a significant effect on the median aspect ratio and angle of the pores. The large pores (larger than 24μm in diameter) tend to have more circular shapes (aspect ratio close to 1), particularly for the sample built with 0.22mm hatch spacing.

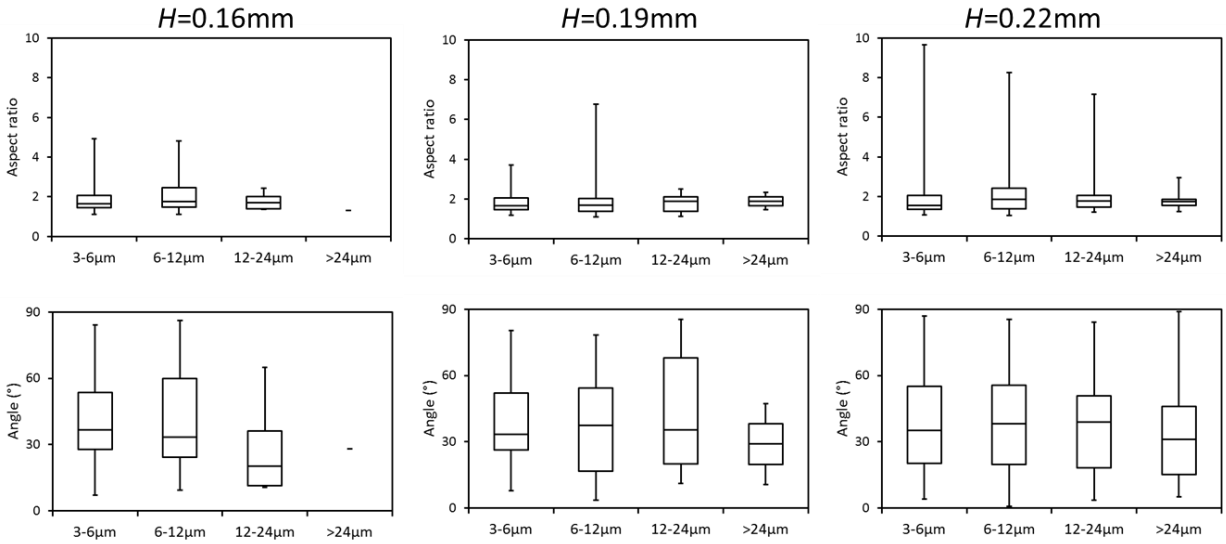

Figure 72. Box plots of the aspect ratio (top) and angle (bottom) of pores measured on the polished planes. Angle is between the longest chord of pores and the *XY* plane. Five horizontal lines (including top and bottom whiskers) represent minimum, 25th percentile, median, 75th percentile, and maximum values, respectively.

Figure 73 shows the fitted distributions of pore sizes as-observed on the polished planes with Gumbel and Fréchet probability functions, and indicates that both distributions fit the pore sizes reasonably well. Table 23 summarizes the optimized distribution parameters, which were used to estimate the pore size distributions on the surface of the fatigue sample and hence the fatigue lives.

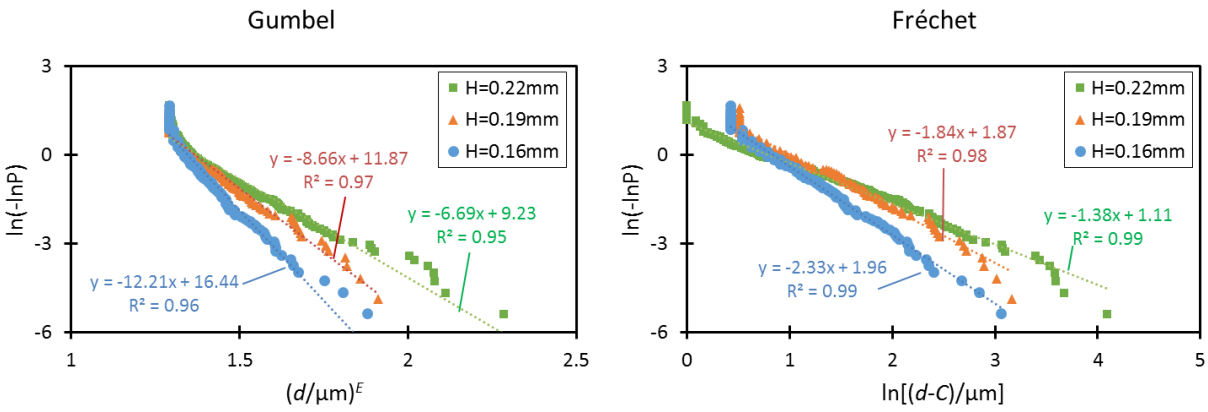

Figure 73. Fitted distributions of pore sizes as observed on the polished planes

Table 23. Optimized fitting of the pore size distributions by Gumbel and Fréchet functions. The unit of measured pore sizes is μm.

Hatch spacing (mm)	0.16	0.19	0.22
Gumbel parameters			
A	10.5	7.5	5.7
B	-14.4	-10.5	-8.0
E	0.21	0.21	0.21
Fréchet parameters			
A	-2.3	-1.8	-1.4
B	2.0	1.9	1.1
C	2.1	1.9	2.6

Oxides

Figure 74 compares the oxygen weight fraction (in ppm) from oxides (diameter larger than 3.6μm) measured by 2D SEM and the total oxygen from the bulk analysis (inert gas fusion). The size distribution and volume fraction of oxides, as reported by 2D analysis, are converted to the weight fraction by a theoretical density of 4.0 g/cm^3 for Al_2O_3. There are two main noteworthy tendencies in Figure 74. First, a larger hatch spacing gives a higher overall oxygen concentration. The exact reason behind the increasing oxide concentration with a larger hatch spacing is still unclear and needs more in-depth study. To expand upon this work, one would need to understand both oxide formation mechanisms and possible oxide removal by the recoater blade after printing each layer [171].

Figure 74 also indicates that, for each hatch spacing, the bulk analysis shows approximately 200ppm higher total oxygen concentration than in the measureable oxide particle distributions from 2D analysis. This consistent gap between two methods reflects small oxides, likely originating from the oxide film on the powder particles. However, the value of 200 ppm is significantly less than the 400 ppm of oxygen as a film on powder particles, as estimated from the powder size distribution [60] and assuming a uniform oxide film thickness of 3.5nm [111]. It appears that some net removal of oxygen occurs during part building.

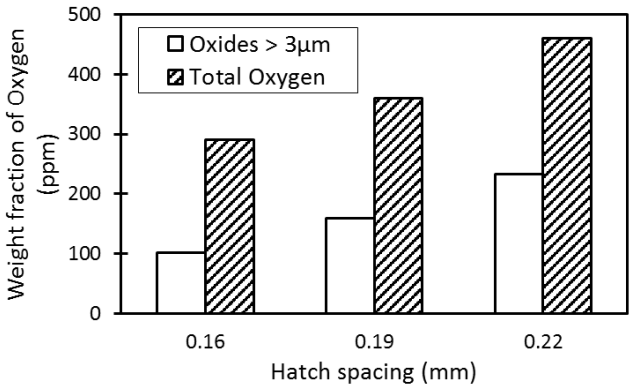

Figure 74. Comparison on the weight fractions of larger oxides estimated by 2D SEM and total oxygen from the bulk analysis by inert gas fusion.

Figure 75 illustrates the size distribution of oxide particles as observed on the polished planes. It is apparent that a larger hatch spacing generally increases both the number and size of oxide particles. This trend is surprisingly similar to the variation of pores observed by 3D (Figure 70b), and possibly implies that oxide-driven pores could in turn scale with the number and size of the oxides.

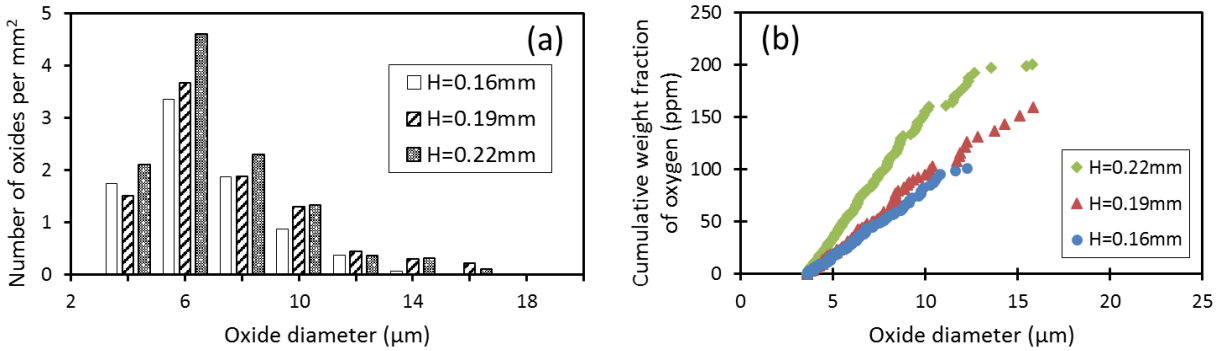

Figure 75. Histogram (a) and cumulative size distribution (b) of large oxides measured on the polished planes.

Comparison between porosity and oxide

Figure 76 below compares the volume fraction and number density of pores and oxides measured on polished planes. As shown in Figure 76a, for the small hatch spacing of 0.16mm, the residual oxides have a comparable volume fraction with pores and may somewhat contribute to the failure during fatigue tests. A larger hatch spacing correlates with more of both types of defect, but with a more pronounced increase in the porosity. Figure 76b reveals that for the standard hatch spacing, pores in the part are larger and more numerous than oxides, indicating that pores would have a stronger direct effect on the fatigue behavior than oxides.

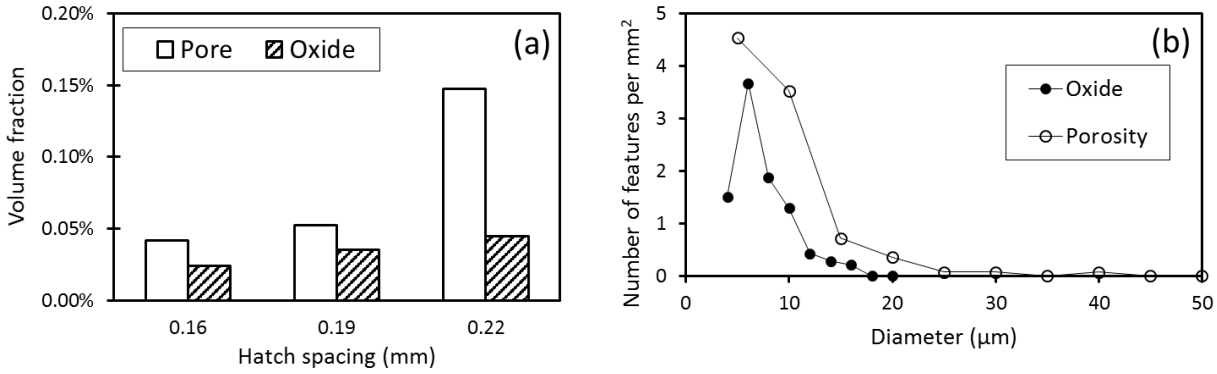

Figure 76. Comparison of the volume fraction (a) and number density (b) between pores and oxides. (b) is for sample built with 0.19mm hatch spacing.

To test the spatial association between oxides and pores, Figure 77 shows the spatial distributions on the polished plane of the sample built with 0.16mm hatch spacing, with no lack-of-fusion porosity. Oxides (solid markers) and pores (open markers) are distributed almost uniformly throughout the cross-section. A large fraction of pores is accompanied by oxide particles. To test this in more detail, Table 29 in Appendix B shows the 30 largest features in the polished section of the sample built with 0.19mm hatch spacing, confirming that most pores are associated with visible oxides. Of the 30 largest features, 21 were oxide-induced pores, 7 were isolated oxide particles, and only 2 pores were not linked to visible oxides (but oxides might have been present, just not in the polishing plane).

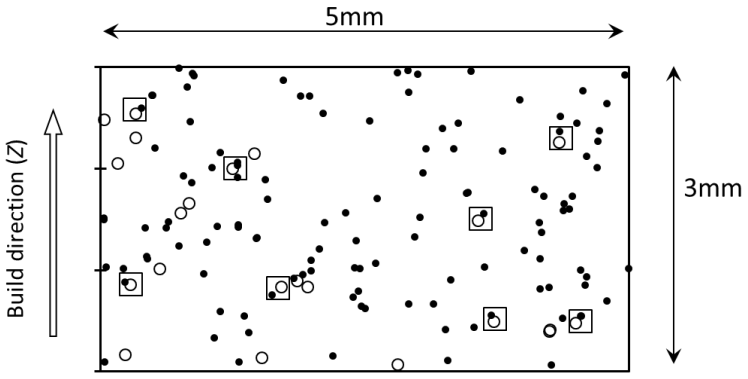

Figure 77. Spatial distributions of pores (open points) and oxides (solid points) in the sample built with 0.16mm hatch spacing. Squares likely indicate oxide-induced pores. 8μm is set as the lower limit of pore diameters to highlight the effect on relatively large ones.

4.3.3 Defect area and fatigue life

Defect areas were measured by scanning electron microscopy; examples were shown in Figure 63. As expected from the difference in fatigue lives (Figure 48), samples built with smaller hatch spacings and horizontal orientation (*XY*-oriented) during building generally showed smaller defect areas on the fracture surface (Figure 78). However, there was considerable overlap between parts built under different conditions.

Figure 78 also shows the correlation between defect area (measured on the fatigue fracture surface) and fatigue life, and compares this with the literature data for A356-T6 alloy with failure initiated by pores. As expected, and in agreement with results for conventionally cast parts [86], smaller defect areas correlated with longer fatigue lives. However, the additive manufactured AlSi10Mg samples have shorter fatigue lives when compared to the A356 cast parts failed with similar defect area. This is likely due to the alloy composition and T6 heat treatment causing a significantly higher yield strength around 270MPa for A356 [175], compared with the typical value of 180MPa for AlSi10Mg printed cylinders.

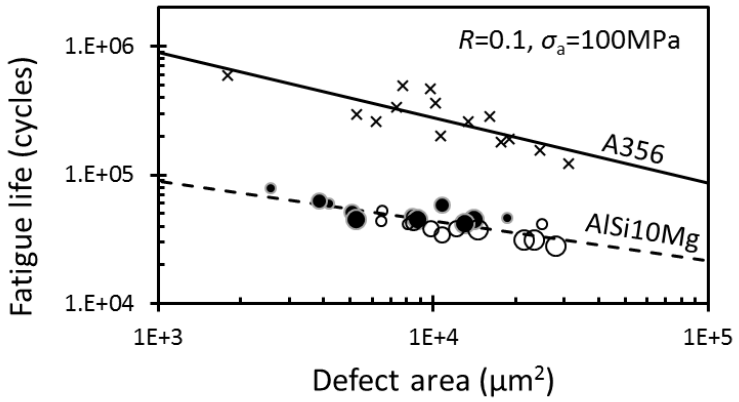

Figure 78. Correlation between defect area and fatigue life, for SLM AlSi10Mg parts (this work, circles), compared with results from conventionally cast A356-T6 (solid line and crosses, failed by pores) [86] tested at the same stress ratio (R_{stress}=0.1) and stress amplitude (100 MPa). Circle sizes indicate the hatch spacing (smallest circles: 0.16 mm hatch spacing; medium-sized circles: 0.19 mm; largest circles: 0.22 mm); filled symbols: *XY* cylinders; open symbols: *Z* cylinders.

In every case, the defect from which the fatigue crack grew was at the surface of the fatigue sample, as expected from literature findings [65], [88]–[90]. From examination of the fracture surface, in only two cases (out of 47 samples) did the fatigue failure grow from more than one surface defect. However, from examination of the cylindrical flanks of the samples, away from the final failure, some crack growth from other surface defects could be seen; an example is shown in Figure 79. However, it does not appear that these affect the measured fatigue life.

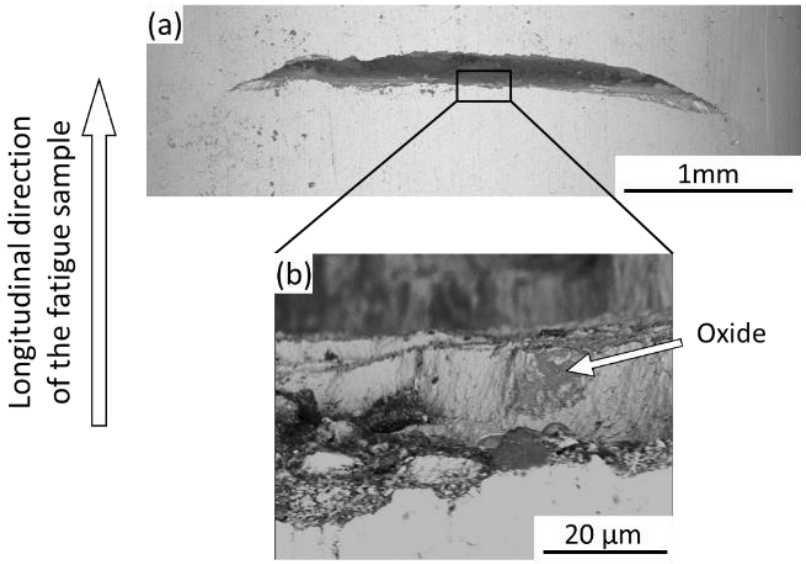

Figure 79. Backscattered electron images of the secondary crack (on the cylindrical part of a fatigue sample, remote from the final failure) and oxides on the crack surface. This sample is from group B (*XY* specimen and 0.19mm hatch spacing).

In general, the relationship between fatigue resistance and strength depends on whether pre-existing defects are present or not. Without pre-existing defects, the fatigue life is dominated by crack nucleation, and stronger alloys give significantly better fatigue resistance. If pre-existing defects are present (as in the material considered in this work), the issue is whether there is any relationship between the stages of crack propagation and final failure, and material strength. In general, there are some effects of the microstructure (and hence strength) on crack propagation (Paris-law behavior), although the effect is weaker than the effect of strength on crack initiation [176], [177]. For aluminum alloys, Yi et al. [178] showed that samples taken from a conventional A356 casting (T6 treatments) showed more cycles of crack propagation to failure for samples that were taken from regions with higher solidification rates (and hence higher strength). For AlSi10Mg parts produced by selective laser melting, Brandl et al. [45] found that T6 heat treatment of parts built with 30°C and 300°C baseplate temperatures changed the fatigue resistance. For both base-plate temperatures, the fatigue life was longer for the samples with the higher strength; the results are summarized in Figure 80.

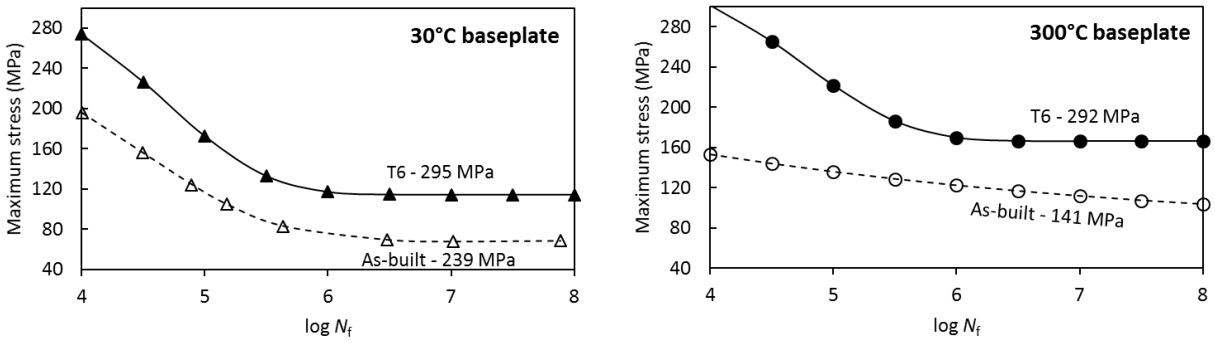

Figure 80. Effect of strength on the fatigue performance of additive manufactured AlSi10Mg parts. The results presented here were collected and plotted with Weibull constants available from Brandl et al [45], [48]. The strength values adjacent to the plots are yield strengths.

As mentioned earlier in the introduction, the Paris-Erdogan law was used to model the fatigue life and Equation 11 can be rearranged to the following form:

$$\log(N_f) = \log(B) - m\log(\sigma_a) + \frac{2-m}{4}\log(A_i) \qquad \text{Equation 11a}$$

The experimental results of fatigue lives and defect areas were used to fit a linear relationship between log(N_f) and log(A_i); the constants of B and m can be estimated from the slope ((2-m)/4) and the intercept (log(B)-$m$log(σ_a)). The values of B and m were optimized by fitting a linear correlation between log(N_f) and log(A_i) for all data points, yielding the smallest error, with results shown in Figure 81.

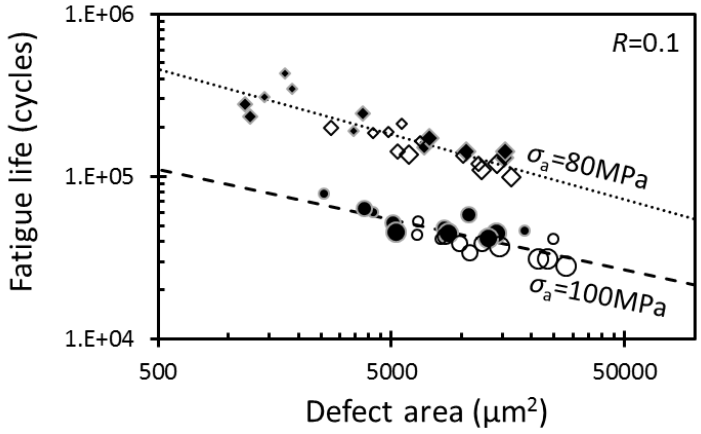

Figure 81. Fatigue life data plotted as a function of the area of the failure-initiating site, for two stress amplitudes of 80MPa and 100MPa. Symbol sizes reflect the value of hatch spacing. Rhombus and circles refer to tests performed at a stress amplitude of 80MPa and 100MPa, respectively. Filled symbols represent *XY* cylinders and open symbols are *Z* cylinders.

Multiple datasets from the literature were also analyzed to validate the linear relationship of Equation 11a; calculated parameters were summarized in Table 24. The *m* values for parts built in this work correctly fall in the range between 3 and 4, as expected for aluminum alloys [65].

Table 24. Comparison of *m* and *B* by fitting Equation 11a for cast Al-7%Si-Mg (A356) aluminum alloys and printed AlSi10Mg.

	Source	*m*	*B*
Printed AlSi10Mg	This work - 100MPa	3.2	2.2×10^{12}
	This work - 80MPa	3.6	3.9×10^{13}
Cast A356	Wang et al. [86]	3.8	7.9×10^{14}
	Yi et al. [98], [99]	4.8	3.3×10^{17}
	Davidson et al. [104]	4.2	8.1×10^{15}

4.3.4 Fatigue life prediction

The fitted pore size distributions on the polished plane were used as inputs, and extrapolated from a small analysis area in 2D to the large surface area of the fatigue sample (serving as the sites for failure) by a scaling factor (*T*). The probability failure (*F*) of the fatigue sample, which is equal to $1\text{-}P(d_{max}<d_c)$, where $P(d_{max}<d_c)$ is the probability that the largest defect is smaller than d_c, the

defect size which would cause failure within a given number of cycles. The critical pore size on the fatigue sample surface for this probability of failure is estimated with the following equations (rearranged from Equation 8 and Equation 9, respectively):

Gumbel $$d_c = \left(\frac{\ln(-\ln(1-F)) - \ln(T) + B}{-A}\right)^{1/E}$$ Equation 32

Fréchet $$d_c = exp\left(\frac{\ln(-\ln(1-F)) - \ln(T) - B}{A}\right) + C$$ Equation 33

where *A*, *B*, *C*, *E* are parameters already optimized by fitting the pore size distribution on the polished plane (see values in Table 23), and *T* is calculated by Equation 10 and values for different samples are listed in Table 25.

As stated earlier (Equation 11a), the defect size is related to the fatigue life by the following equation (substituting *m* and *B* with values in Table 24):

100MPa amplitude $$N_f = 8.1 \times 10^5 \, d_c^{-0.62}$$ Equation 34

80MPa amplitude $$N_f = 6.0 \times 10^6 \, d_c^{-0.80}$$ Equation 35

where N_f is the fatigue life and d_c is the equivalent circular diameter in microns.

Table 25. Calculation of the scaling factor (*T*) for each hatch spacing.

Hatch spacing (mm)	0.16	0.19	0.22
Analyzed area $S_{analysis}$ (mm^2)	16.1	13.9	19.6
Number of pores detected (n)	209	130	215
Test area* (S_{sample}) (mm^2)	325	325	325
$T = nS_{sample}/S_{analysis}$ =	4214	3045	3573

* The test area (S_{sample}) is estimated with the fatigue sample dimension as shown in Figure 12.

Figure 82 shows the calculated fatigue life distribution based on the measured pore size distribution. For each hatch spacing, the fatigue life has a quite large variation and spans a wide range. The distribution function used to extrapolate the size distribution to the fatigue sample strongly affects the predicted life; this is a result of the necessarily limited area examined for pore size analysis. The effect of limited analysis area is illustrated qualitatively in Figure 83: with a larger analysis area, the largest detected pore is greater, but still much smaller than the failure-initiating pores observed on the fatigue fracture surface.

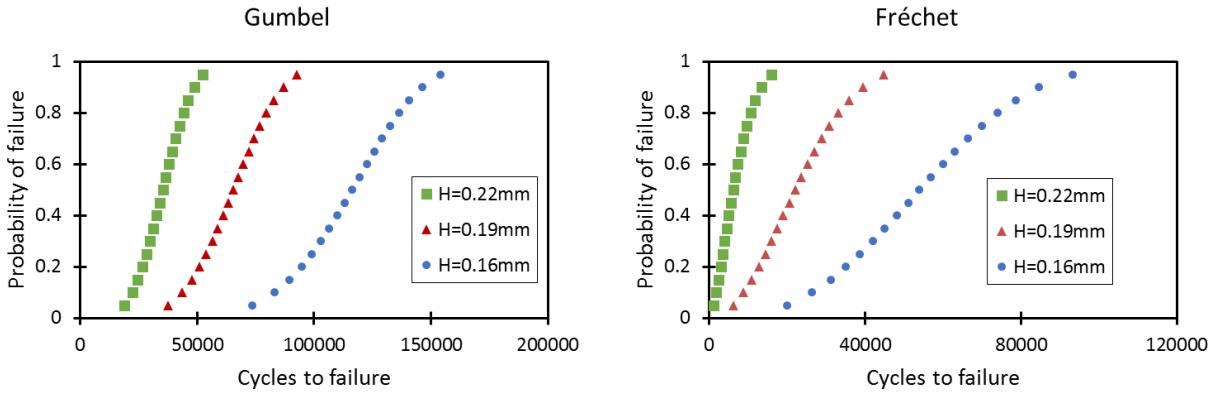

Figure 82. Predicted distribution of fatigue lives for samples built with various hatch spacings based on different distribution functions. The porosity size distributions measured from polished planes were used as input. The stress ratio is 0.1 and stress amplitude is 100MPa.

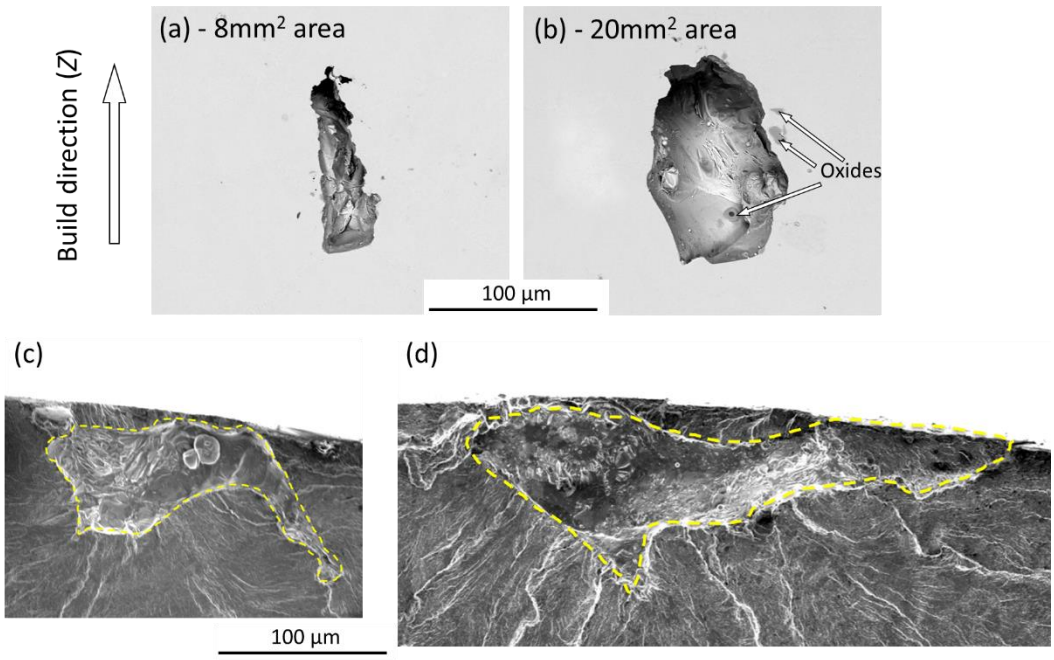

Figure 83. The largest pores found by 2D SEM when analyzing smaller (a) and larger (b) areas, for the sample built with 0.22mm hatch spacing. Two images at the bottom are smallest (c) and largest (d) failure-initiating pores found on the fatigue fracture surfaces of samples built with the same condition.

Figure 84 compares the predicted fatigue lives (50% failure probability) with observed average cycles to failure. The Gumbel function shows a better agreement, whereas the Fréchet distribution significantly overestimates the pore sizes and so underestimates fatigue lives, particularly for parts built with a larger hatch spacing.

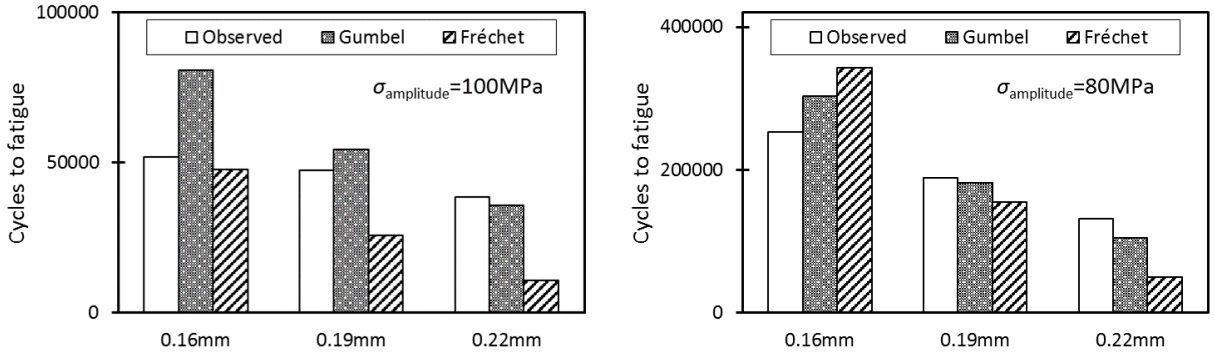

Figure 84. Averaged (50% probability) fatigue lives from experimental tests and predictions. The stress ratio is 0.1 and stress amplitudes are 100MPa and 80MPa, respectively.

4.4 Prediction of lack-of-fusion porosity

4.4.1 Background

Limiting part porosity is essential for building parts with good mechanical properties. The approach described in this work can be used to predict whether processing conditions in a powder bed fusion process would lead to porosity due to lack of fusion [105], [179]. Other causes of porosity in powder bed fusion include entrapped gas, keyholing, and oxide-induced porosity; these are not addressed by this prediction method.

Although internal porosity of metal parts manufactured by selective laser melting has been studied for many years, predicting and controlling porosity inside the products still remains a challenge. Numerous studies have been carried out to assess the effect of processing parameters on part density (which is a direct indication of the volume fraction of internal porosity) [174]. Part porosity is often correlated with the process parameter "Energy density," usually defined as volumetric power input (see Equation 36) [174], [180], [181].

$$Energy \quad density = \frac{P}{VHL} \qquad \text{Equation 36}$$

where P is the beam power, V the beam speed, H hatch spacing, and L layer thickness.

Typical experimentally measured curves of part density (or porosity) with respect to energy density (Figure 85) show increased porosity due to keyholing at high energy density (high power and low speed), minimum porosity at intermediate energy density, with the porosity increasing again (due to incomplete melting, or "lack of fusion") at lower energy density; see Figure 85.

The fundamental origin of lack-of-fusion porosity is the insufficient overlap of successive melt pools. In the approach present here, the melt-pool overlap is calculated to predict lack-of-fusion porosity. The fundamental parameters used in the calculation are melt-pool cross-sectional dimensions, hatch spacing, and layer thickness. The approach allows rapid prediction of the effects of changes in processing parameters (beam power and beam speed, hatch spacing, and layer thickness) on part porosity.

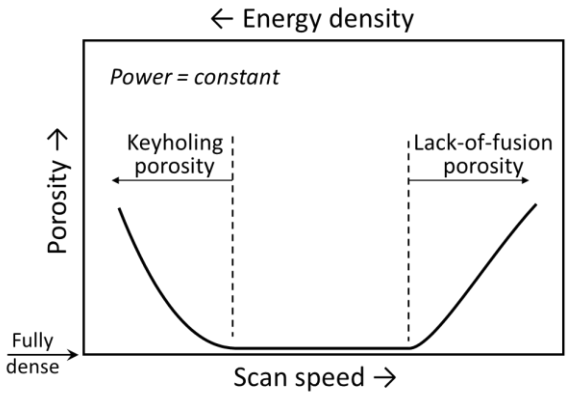

Figure 85. A typical trend of part porosity with changes in scan speed and energy density (at constant power). Drawn after the results of Gong et al. [174]

4.4.2 Calculation approach

The fundamental principle behind the calculation is that, for complete melting, the depth of the overlap between adjacent melt pools (L^*; see Figure 86) must be at least as large as the layer thickness (L) used in building the part. If $L>L^*$, the part will contain lack-of-fusion porosity; for such conditions, the volume fraction of lack-of-fusion porosity can be calculated using the approaches described in this work.

Input parameters: melt-pool geometry

The main input parameters for porosity prediction are the melt-pool dimensions (width and depth), hatch spacing, layer thickness and hatch rotation. While the latter three parameters are generally controlled directly, the melt-pool dimensions are not. The melt-pool size depends primarily on absorbed power, beam speed and the thermal properties (conductivity and diffusivity) of the material [150]. As with the general approach to process mapping [150], two approaches can be used: the melt-pool dimensions can be measured experimentally, or these can be estimated by calculation (as discussed earlier). For the examples shown here, melt-pool dimensions were estimated using the simple analytical Rosenthal equation with absorptivity and alloy properties in Table 12 [23].

Analytical relationships

Analytical relationships were derived to guide simulations and processing choices. Each melt pool contains previously deposited material which is remelted in the current beam traverse, and newly deposited material (powder which is melted into the pool). The newly deposited material forms a "cap" (or "reinforcement" in welding terminology [182]) on top of the previously deposited layers. To derive the analytical relationships, the cross-sections of the remelted material and the cap were assumed to be half-ellipses, with their major horizontal axes both equal in length to the melt-pool width (*W*) and located at the surface of the previously deposited layer (see Figure 86). This geometry was found to approximate many real melt pools and greatly simplifies analytical treatment. (In the simulation approach described later, any melt-pool cross-section shape can be used in principle, although the simulation examples shown are for the dual half-elliptical melt-pool cross-section depicted in Figure 86.)

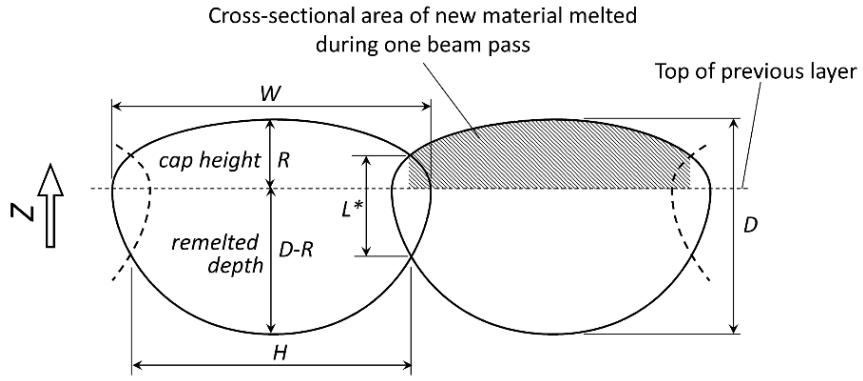

Figure 86. Schematic of the assumed dual half-ellipse shape of melt pools, showing the overlap between two adjacent beads (for a cross-section in the build direction, perpendicular to the beam scanning direction), and with relevant dimensions labeled.

Criterion for full melting

For this dual half-elliptical melt-pool cross-sectional shape, the same relationship previously given for half-elliptical cross-sections [105] states the conditions for which $L^* \geqslant L$:

$$\left(\frac{H}{W}\right)^2+\left(\frac{L}{D}\right)^2\le 1 \qquad \text{Equation 12}$$

where H is the hatch spacing, W the melt-pool width, L the layer thickness, and D the total melt-pool depth. That is, the combinations of hatch spacing and layer thickness that give full melting (no lack-of-fusion porosity) depend only on the melt-pool width and the total melt-pool depth; there is no dependence on cap height (R in Figure 86) as such.

For process conditions that do not obey Equation 12, lack-of-fusion porosity would be present in the built part. The simulations discussed later in this document were used to calculate the expected fraction porosity for such conditions. One thing worth noticing is that this criterion only holds true for non-zero scan rotation between layers if the melt pools in consecutive layers do not have random offsets. The example of zero rotation is discussed as an exception in the following section.

Build rate, number of melting cycles and cap height

The build rate (part volume deposited per unit time, including porosity) is simply given by:

$$\text{Build rate} = HLV \qquad \text{Equation 37}$$

The cross-sectional area of a dual half-elliptical melt pool depends on just its width and depth (and not on the cap height):

$$A = \pi DW/4 \qquad \text{Equation 38}$$

Because of the overlap between melt pools, the material deposited in the part is in general remelted several times. The average number of melting cycles (n_{melt}) is equal to the rate at which the melt-pool volume propagates through the part ($A \times V$) divided by the build rate:

$$n_{\text{melt}} = (\pi/4)(W/H)(D/L) \qquad \text{Equation 13}$$

For process conditions where the melt pools overlap fully laterally ($H<W$) and in the Z direction (that is, conditions which obey Equation 12), the height of the cap (R) is found from melt-pool geometry, recognizing that the cross-sectional area of material deposited with each bead is given by the shaded region in Figure 86. This leads to the relationship given in Equation 39:

$$R = \frac{2L}{\sqrt{1-(H/W)^2} \;+\; (W/H)\sin^{-1}\left(\frac{H}{W}\right)} \qquad \text{Equation 39}$$

4.4.3 Simulation principle

A square two-dimensional slice (in the build direction) through a built part was simulated (see Figure 87). The melt-pool shape was as given in Figure 86. The calculation inputs were the melt-pool dimensions (*W*, *D*, and *R*; see Figure 86), hatch spacing (*H*), layer thickness (*L*), and the angle between the beam scanning direction of subsequent layers ("hatch rotation"). Consecutive melt pools were placed within the simulation region a layer at a time, as in the actual powder-bed processes. For each layer, melt pools were placed from left to right; the position of the leftmost melt pool was randomized. The apparent width of each melt pool on the cross-section was calculated from the beam direction of that layer (as determined by the number of layers deposited and the hatch rotation). For the results shown here, all melt pools were assumed to have the same width and depth (for one set of building conditions); however, the practically observed variation in melt-pool size on the polished plane of top surfaces (see Figure 36 and Table 15) and along a single bead [107], [158] could be readily incorporated in the simulations.

The number of pixels in the simulated area could be adjusted; the simulations shown here were for 1000 pixel side lengths, with each pixel corresponding (in these examples) to a distance of 1 μm. For each pixel, the number of times it was within a melt pool was totaled. Each melt pool was assumed to be well-mixed within the plane of the slice, with an average number of melting cycles assigned to all pixels within that melt pool.

The simulation was implemented in Python; the libraries *matplotlib* and *numpy* [183] facilitated calculating and displaying the simulation results. Typically at least ten simulations were performed for each set of processing conditions to obtain reliable estimates of the average unmelted volume.

For faster estimates of the porosity, calculations were based on the same dual half-elliptical melt-pool cross-section, but instead calculating the probability that positions in a plane at a particular vertical position would not be melted during deposition of any of the layers. The principle of the calculation is illustrated in Figure 88. As an example, Figure 88 illustrates that the probability that positions at the top of layer 1 would remain unmelted after the first pass is simply given by δ_{01}/H, where δ_{01} is the shortest distance between the melt pools at the top of this layer (δ_{01}/H=1 for the melt-pool geometry shown). This position would have a probability δ_{02}/H of not being melted during deposition of the next layer, and of δ_{03}/H when the third layer was deposited.

If the positions of unmelted areas between subsequent layers were independent (that is, with random offsets between melt-pool positions for consecutive layers), the probability of this position remaining unmelted after three passes would be given by $(\delta_{01}/H)\times(\delta_{02}/H)\times(\delta_{03}/H)$. Similarly, positions one layer thickness (L) below the top of layer 1 would have a probability $(\delta_{L_1}/H)\times(\delta_{L_2}/H)$ of remaining unmelted (for the example shown, layer 3 did not extend down to this level). To calculate the total porosity, this calculation was performed for 100 positions distributed vertically over the distance L from the top of layer 1, using numerical integration to find the overall probability of positions in one layer remaining unmelted; the calculation was implemented in a spreadsheet. The distances (δ) were found readily, based on the geometry of the dual half-elliptical melt pools.

The example in Figure 88 is for the case where the layer thickness is between one-half and one-third the melt-pool depth, but the approach can be readily extended to any value of L/D. Figure 88 was drawn for zero rotation between subsequent layers, but the probability of not being melted by subsequent layers is independent of the rotation angle.

The full (Python) and faster (spreadsheet) simulations gave the same estimates of unmelted volume fractions, for the same input values. (This comparison is presented later, in Figure 94.)

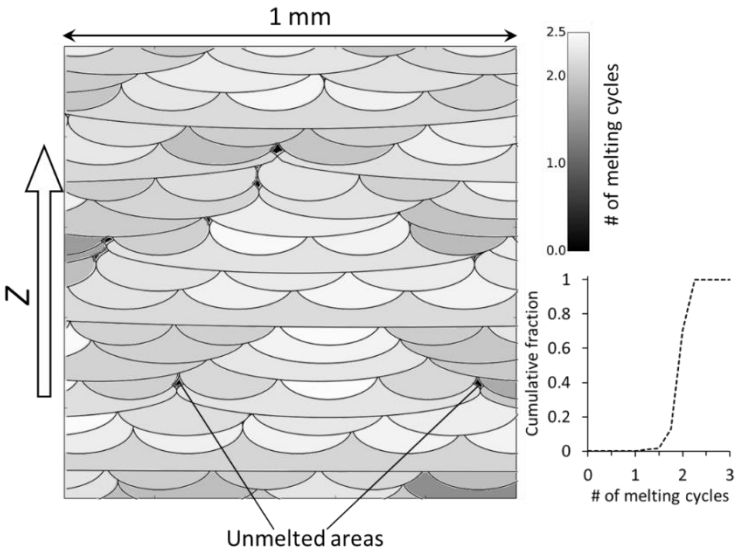

Figure 87. An example of the simulated part. Each melt pool is shaded to indicate the average number of times the material was melted (using the grey scale shown at right.) Melt-pool boundaries drawn in for clarity. The graph at the bottom right gives the distribution of the number of melting cycles for all the melt pools. Assumed dimensions: *W*=220 µm; *D*=110 µm; *R*=51 µm; *H*=220 µm; *L*=40 µm; hatch rotation: 67°

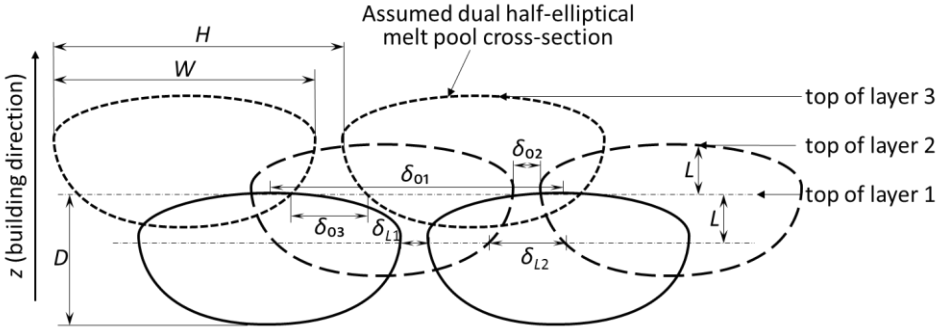

Figure 88. Geometric relationships used in the simplified approach to estimating the probability of different positions in the part remaining unmelted. (Shown for zero rotation between the scanning directions of consecutive layers.)

The main result of each simulation was the fraction of unmelted volume in the part, ε. The unmelted fraction was calculated as the area fraction of unmelted pixels in the Python simulation, and the probability of remaining unmelted in the spreadsheet calculation. The unmelted fraction

was converted to an estimated porosity by assuming the unmelted volume to be filled with powder, and by using an assumed density of fully melted regions. Based on literature results on the porosity in powder beds (0.36 from [107], 0.44 from [130], 0.30 from [184]), the volume fraction of pores in unmelted volumes was taken to be 0.36. The fully melted regions of the part were assumed not to be fully dense, since inspection of literature results indicated that parts typically are approximately 99% dense for process conditions which should eliminate lack-of-fusion porosity. Based on these two considerations, the density of the part relative to the fully dense material was calculated as follows:

$$\rho_{\text{part}} / \rho_{\text{true}} = 0.64\varepsilon + 0.99(1-\varepsilon) \qquad \text{Equation 40}$$

4.4.4 Comparison of measured and predicted porosity

In these simulations, it was assumed that only insufficient melt-pool overlap causes lack-of-fusion porosity, and that powder flow is not limiting. To test the simulation model predictions, experimental density data of test pieces from the literature was used for comparison. Three materials (AlSi10Mg, TiAl6V4, and steel) and machines of two manufacturers (EOS and Concept Laser) were considered, with detailed processing parameters and main variables summarized in Table 26. For these comparisons, the melt-pool sizes were estimated with the Rosenthal equation, using the material properties listed in Table 12. The simulations used the scan patterns employed when building the parts for which densities were reported. Specifically, hatch spacing, layer thickness, and hatch rotation were all considered.

Figure 89 illustrates the success of this model, with measured densities or porosity (solid lines with filled markers) and calculated values (dashed lines with open markers) matching very well. The available experimental data allowed the effects of all processing parameters to be tested, including power (Figure 89 a and c), scanning speed (Figure 89 a-e), hatch spacing (Figure 89 a and d) and layer thickness (Figure 89 d-f). The simulations correctly predicted both the process conditions beyond which porosity started to increase, and rates of porosity increase (with higher beam speed, hatch spacing, or layer thickness).

Table 26. Processing parameters from literature data for model validation shown in Figure 89.

No. in Figure 89	Ref.	Machine	Material	*P* (W)	*V* (mm/s)	*H* (μm)	*L* (μm)	Max relative density (%)
a	[52]	EOS M270	AlSi10 Mg	180, 195	700, 800,900	100, 170, 250	30	99.1
b	[185]	EOS M270	MS1*	200	400-3000	100	40	99.2
c	[174]	EOS M270	TiAl6V 4	40, 80	240-1560	100	30	100
d	[185]	Concept laser M3	20ES*	100	225, 450	50-180	30,40,60	99.0
e	[185]	Concept laser M3	50WS*	100	240-600	125	30, 60	97.1
f	[186], [187]	Concept laser M2	TiAl6V 4	400	2400	75	20~100	99.1

*MS1 and 50WS are maraging steels and 20ES is a stainless steel

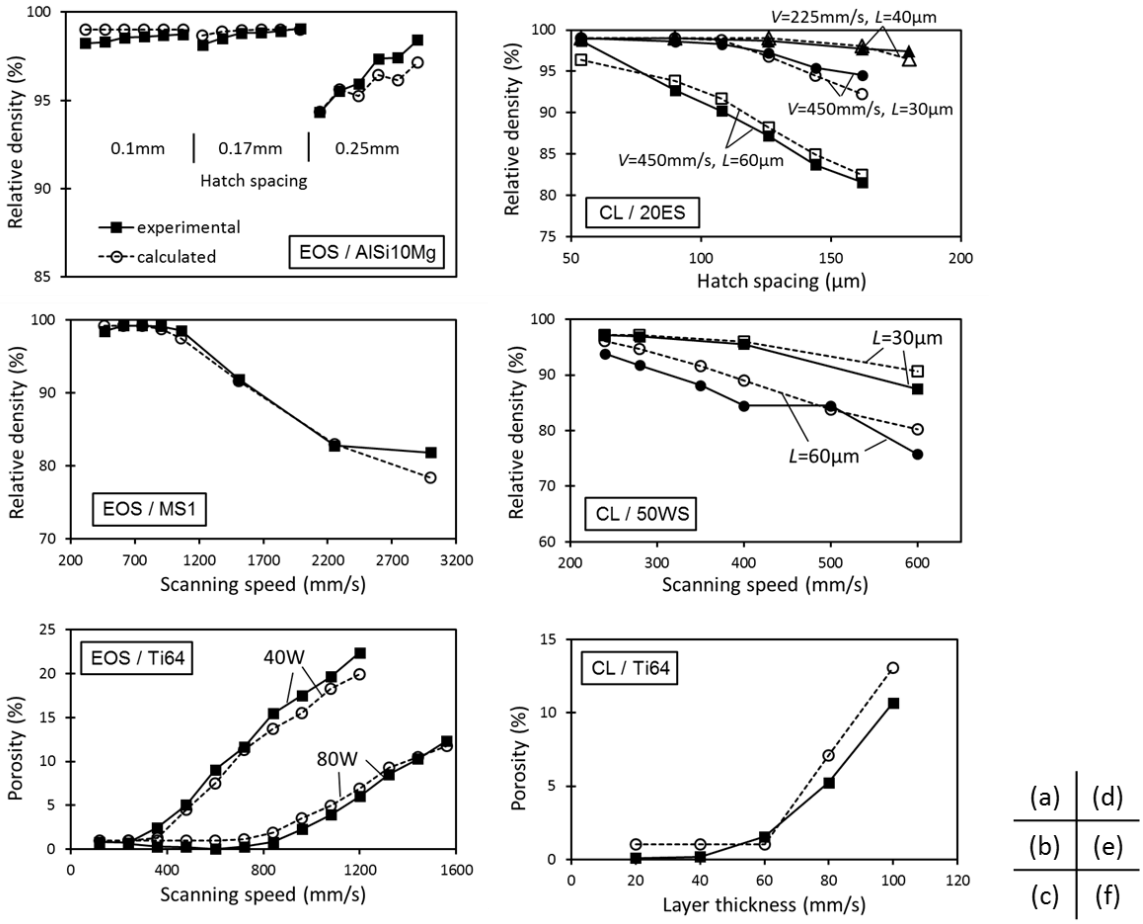

Figure 89. Comparison of measured (literature data) and predicted (this work) part density. Solid lines and filled markers are experimental results, and dashed lines with open markers are simulation results (this work). See Table 26 for references and process conditions.

It should be noted that additional scanning strategies commonly used during fabrication were not included in the present model. First, layer remelting would help to reduce final part porosity, but none of the builds considered here (in Table 26 and Figure 89) employed remelting during part fabrication. Second, contour scans were not considered in the model, since the contours only account for a small volume fraction of the printed samples (part sizes were at least 10×10×10 mm in the literature cited). Third, island scanning (as employed by the Concept Laser machine) is not expected to have a significant effect on the overall porosity, as the island size was large compared with the part size for the builds considered here (5mm×5mm islands for a part with a 20mm×20mm

sample cross-section) [185]; for these conditions, overlap between islands would not give a noticeable difference in overall lack-of-fusion porosity.

The effect of such scanning strategies (islands or overlapped stripes) could be included readily in the simulation. Similarly, changes in melt-pool size at the start and end of scans could be simulated, and would be valuable for simulation of complete parts. However, the available experimental data did not allow the effect of such transient changes in melt pool size to be evaluated. Another useful addition to the model would be to consider local part geometry (such as overhangs or thin walls) which would change heat transfer conditions, and hence give different melt-pool sizes. For such cases, the prediction method would remain the same (based on melt pool overlap), and would consider the particular scanning pattern and estimated melt-pool sizes for the particular heat transfer conditions.

As mentioned earlier, the melt-pool dimension can be either predicted by the Rosenthal equation with processing parameters or measured experimentally by single bead tests. Kamath et al. investigated the effect of processing parameters on melt-pool geometry by measuring the single bead width (*W*), top height of the cap (*R*), and depth of the bottom remelted region (*D*-*R*) over a wide region of *P*-*V* space [138]. Geometric dimensions of single beads were employed as input in the geometric model to estimate the density of the final product. Figure 90 compares densities estimated with inputs of processing parameters (plus the Rosenthal equation) and single bead dimensions. Although both methods slightly overestimate the final porosity, they provide the correct starting point beyond which significant density loss is introduced by a relatively large scan speed. One likely reason for the higher predicted porosity is that the experimental work applied an "island scanning" strategy, which scans each powder layer with small islands [28], [138], [185]. The overlap between islands (15% of track width), which could reduce some internal porosity, is not considered in the geometric model.

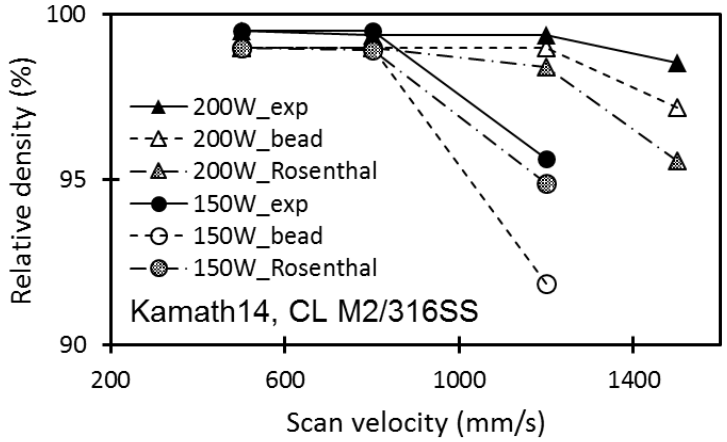

Figure 90. Comparison of measured density and predicted densities using melt-pool sizes estimated using processing parameters (labeled "Rosenthal") and obtained from single bead dimensions (labeled "bead," from Kamath et al. [138]). Solid markers (labeled "exp") refer to measured density.

4.4.5 Processing map

Equation 12 describes a simple relationship between values (L/D) and (H/W) which would avoid lack-of-fusion porosity; graphically, the relationship is in the form of a circular arc (if L/D is plotted vs. H/W); see Figure 91 and Figure 92. If Figure 91 is drawn for constant values of power and speed, the broken lines are contours of constant build rate, and also constant energy density. In these figures, the contour labeled "standard build rate" refers to the processing parameters for EOS M280/AlSi10Mg, as studied in this research [105].

In addition to porosity prediction, one important potential application of the geometric model would be to identify possible processing parameters to improve the build rate, which could be achieved by a slightly smaller hatch spacing and much larger layer thickness, as indicated by the arrow in Figure 91. Theoretically, H/W and L/D for build rate optimization should both be $\sqrt{½}$=0.707. This is close to the practically used hatch ratio (H/W) of 0.74, which is estimated from the experimentally measured melt-pool width and default hatch spacing in EOS machine for building TiAl6V parts [137], but with a much smaller value of L/D. Accordingly, it appears that the default deposition parameters of the EOS machine provide suitable horizontal overlap between

melt pools in the same layer, but redundant vertical overlap between layers, which would adversely affect the production rate and consequently the part cost.

For comparison with the predictions of this work, Table 27 summarizes the standard processing parameters for producing parts of various materials, which conditions are also included in the map of Figure 92. For plotting these, the melt-pool depth was estimated with the Rosenthal equation with absorptivity and alloy properties as in Table 12. Figure 92 demonstrates that most standard processing conditions are well within the safe range for producing fully dense products. As shown in Figure 92, in many cases it appears that there is room to increase the build rate without causing lack-of-fusion porosity.

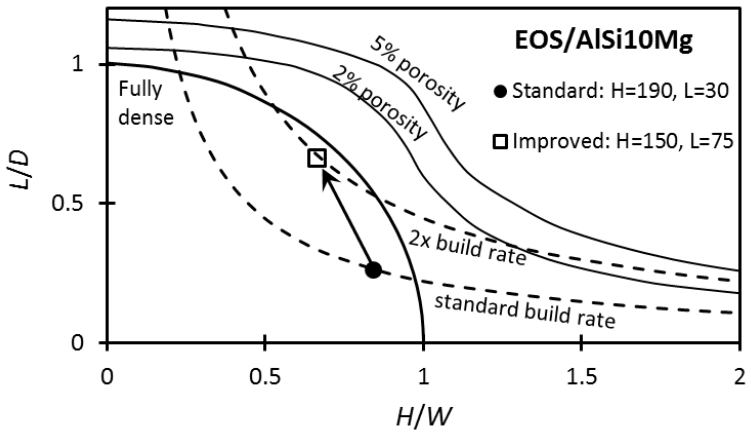

Figure 91. Processing map with isopleths of porosity and build rate; conditions within the circular arc would avoid lack-of-fusion porosity. Units are in μm.

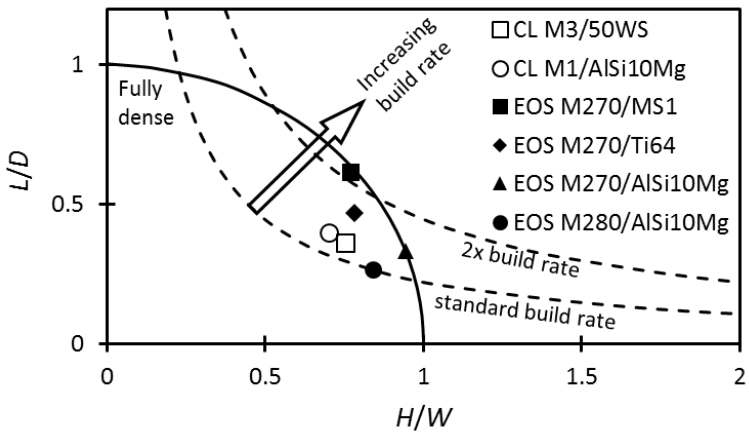

Figure 92. Processing map of hatch spacing and layer thickness (relative to melt-pool dimensions). Markers indicate standard building conditions for different machine/material combinations (see Table 27 for references).

Table 27. Standard processing parameters for machines and materials, showing melt-pool depth estimated with the Rosenthal equation (D_R).

Machine	Material	Reference	P (W)	V (mm/s)	H (μm)	L (μm)	D_R (μm)
Concept laser M3	50WS (maraging)	[185]	100	200	125	30	83
Concept laser M1	AlSi10Mg	[28]	200	1400	105	30	75*
EOS M270	MS1 (maraging)	[185]	200	750	100	40	65
EOS M270	TiAl6V4	[188]	170	1250	100	30	64
EOS M270	GP1 (stainless)	[180]	195	800	100	40	63
EOS M270	AlSi10Mg	[52], [188]	195	800	170	30	90
EOS M280	AlSi10Mg	[105]	370	1300	190	30	113*

*Recalculated values using an absorptivity of 0.32, as noted in Table 13.

4.4.6 Porosity changes at the same energy density

As mentioned above, the broken lines in Figure 91 and Figure 92 are contours of constant building rate and of constant energy density (if the processing map is drawn for constant power and speed). The energy-density contours intersect the circular arc which defines the minimum

condition for parts with no lack-of-fusion porosity. The implication is that increases in energy density need not necessarily improve part density, and that maintaining a constant energy density (while changing other processing conditions) may result in varying porosity. Literature results for parts built at the same energy density but different power/velocity combinations [180] were used to test this prediction, with the results given in Figure 93. Both the measurements and the simulations demonstrate that maintaining the same energy density does not guarantee a constant porosity. (Simulation results are shown for two values of absorptivity - 0.3 and 0.35 - because of the wide range of laser powers in this data set; in general, it is expected that the absorptivity would be somewhat smaller at lower laser power [135].)

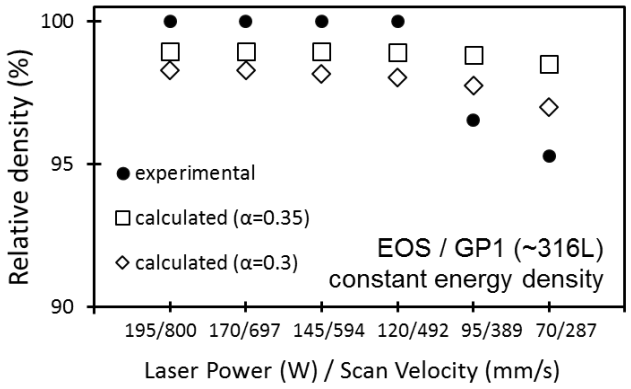

Figure 93. Densities of GP1 (stainless steel) parts built at the same energy density but different combinations of laser power and speed, showing experimental measurements [180] and simulation results (this work).

4.4.7 Effect of varying melt-pool dimensions

Cap height

The criterion for full melting (Figure 87) does not depend on the cap height. However, for conditions where this criterion is not met (that is, when lack-of-fusion porosity would be present), it might be expected that the detail of the melt-pool shape might affect the total porosity. To test this, full simulations were performed for different cap heights, and for melt pools with different depth-to-width ratios. These results were compared with the faster (spreadsheet) calculations (Figure 88) for the same melt-pool geometries. In Figure 94 the results of the faster calculation are

shown by broken lines and those of the full simulation with markers; the predictions of the two simulations agree. The simulations also indicate that there is no significant effect of cap height on the unmelted volume fraction (although the shapes of unmelted volumes would vary).

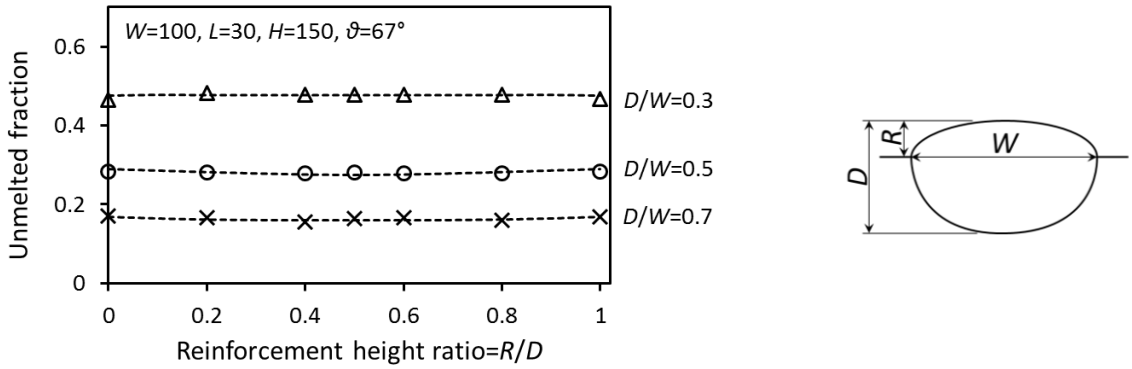

Figure 94. Predicted unmelted volume fraction for various ratios of cap height to melt-pool depth, different ratios of melt-pool depth to width, and hatch rotation angle of 67°. Broken lines are the result with the faster (spreadsheet) simulation, and the open markers are the results of the full (Python) simulation. The melt-pool width was constant at 100 (arbitrary length units).

Larger melt-pool depth

As mentioned earlier, the Rosenthal calculations often underestimate the melt-pool depth. To test the effect of this underestimate, simulations were repeated with 20% larger melt-pool depths for one machine / material combination at two values of laser power and different speeds. Figure 95 shows the expected lower porosity (higher density) with increased melt-pool depth, although the effect is not large. Certainly, improved estimates or measurements of melt-pool depth and width would improve the accuracy of the predictions of this geometry-based simulation.

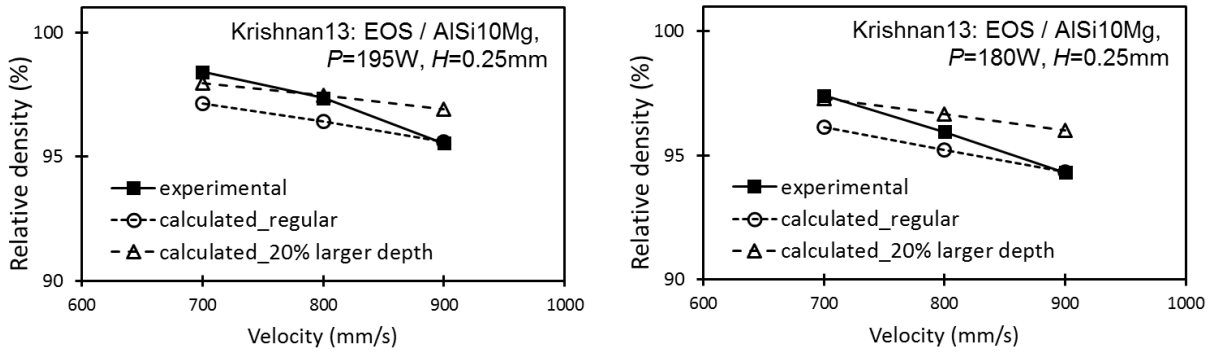

Figure 95. Effect of a 20% increase in melt-pool depth (without changing the total melt-pool width) on the predicted part density, compared with measurements [52]; conditions are for case (a) in Figure 89.

Melt-pool size variation

Since melt-pool dimension is not consistent during the building process, such variation, as tabulated in Table 15, may affect the resulting porosity in the product. Two groups of literature data (Figure 89 a and d) were adopted to test the effect of inconsistent melt-pool sizes by comparing predicted densities with and without variation. The relative standard deviations of the melt-pool depth and width in Table 15 were applied in full (Python) simulations. At least 20 simulations were completed to calculate the average porosity. Figure 96 reveals that varying melt-pool size does not have a significant influence on the overall porosity. Although the effect appears to be small, in principle variations in melt-pool size around the average would imply that isopleths of porosity (in Figure 91) should be expanded to bands.

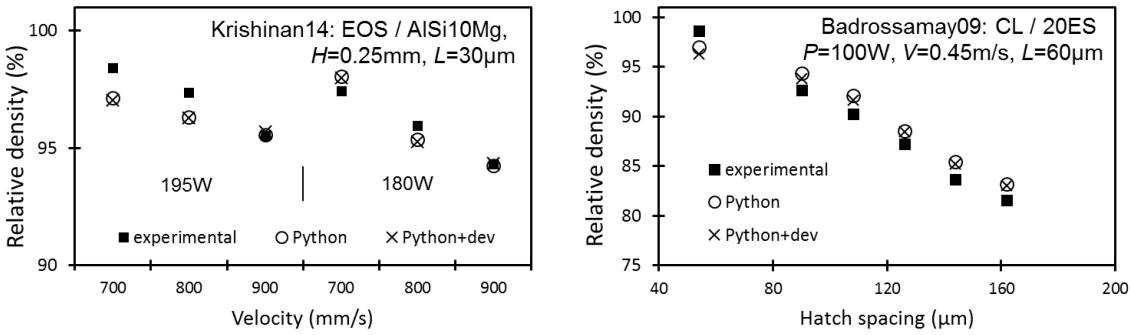

Figure 96. Effect of melt-pool size variation on part density by using literature data [52], [185]. Solid square dots are experimental results. Cross and open circle markers refer to estimated densities with and without size variation.

4.4.8 Hatch rotation angle and beam offset

Apart from processing parameters in Table 1, another two important deposition parameters are hatch rotation angle and beam offset and their effects on part density are discussed in this section. Figure 97 illustrates a top view showing hatch rotation angle and beam offset between two consecutive layers. The solid lines represent the edge of individual scan tracks, and dashed lines refer to centerlines. In this example, the white tracks, representing the layer immediately above the grey tracks, is rotated by 45° and shifted rightwards by a distance indicated by *BO* (beam offset) along the reference line.

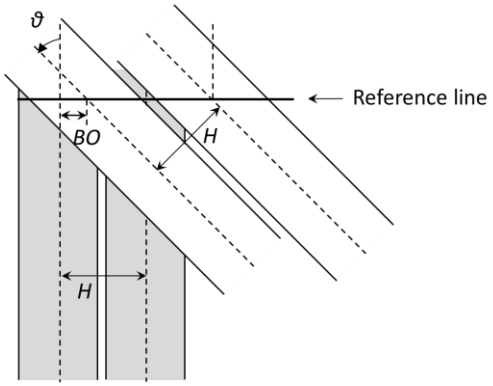

Figure 97. Schematic of hatch rotation angle and beam offset. Reference line represents a transverse cross-section of the bottom-most scan (as shown in Figure 87).

Hatch rotation angle

Five hatch rotation angles (including standard angles for industrial machines, which are 67° for EOS machines [60], [189], and 90° for Concept Laser machines [28]) and two melt-pool dimensions were selected for the test, with results shown in Figure 98. The dashed lines refer to unfused fractions estimated by the faster (spreadsheet) simulation and black data dots were calculated with the full (Python) simulation. Faster simulation gives one specific unfused ratio, since it is inherently independent of the hatch rotation angle and assumes random beam offset (whereas these are adjustable in the full simulation). The variability of the simulation results is caused by the limited analyzed area (1000μm×1000μm). The average values (black data points) are taken from 40 simulations, and vertical error bars give 95% confidence intervals on the mean. Figure 98 reveals that the unmelted volume fraction after multiple passes is independent of hatch rotation angle under the condition of random beam offset. Good agreement between the two calculation approaches in turn supports the assumption (in the faster simulation) that successive passes for the same region are independent. The specific exposure pattern with a hatch rotation angle of 67° was designed to homogenize the residual stress in the part [189].

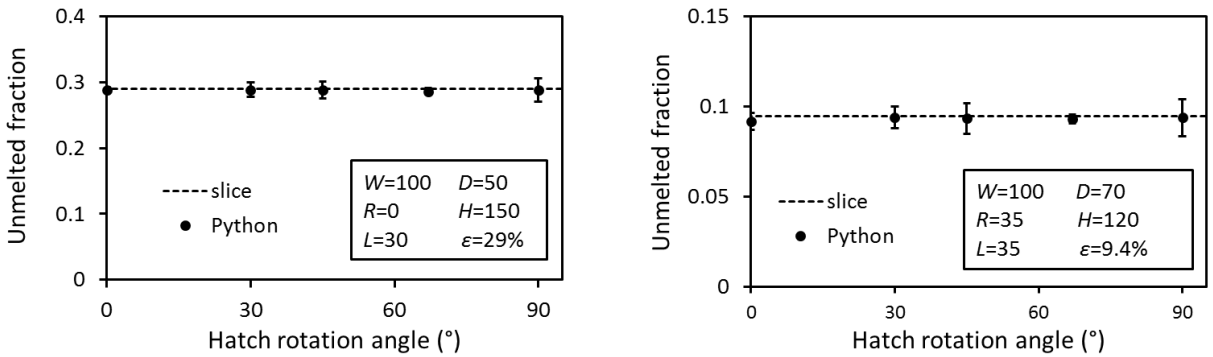

Figure 98. Unmelted fractions with respect to hatch rotation angles. Random beam offset is applied to all cases. Dashed lines are calculated from faster (spreadsheet) simulation and solid circular markers refer to average values estimated with full (Python) simulation.

Apart from the geometric analysis in this work, the effect of hatch rotation angle has been tested experimentally by other researchers. Guan et al. investigated the effect of multiple rotation angles (90°, 105°, 120°, 135° and 150°) on the mechanical properties of 304 stainless steel parts,

utilizing the flexibility offered by a self-developed SLM machine [190]. They showed that hatch rotation angle has little effect on strength (yield strength, ultimate tensile strength) and ductility (elongation), as shown in Figure 99. Since ductility is generally quite sensitive to the volume fraction of internal pores, we can safely guess that the hatch rotation angles do not affect residual porosity. Additionally, Thijs et al. tested two rotation angles (0° and 90°) for AlSi10Mg parts fabricated by Concept Laser M1 machine [28]. However, in that work parts built with these two angles would have been close to fully dense (38%-44% overlap of melt-pool width) and hence the results would be expected to be insensitive to the rotation angle.

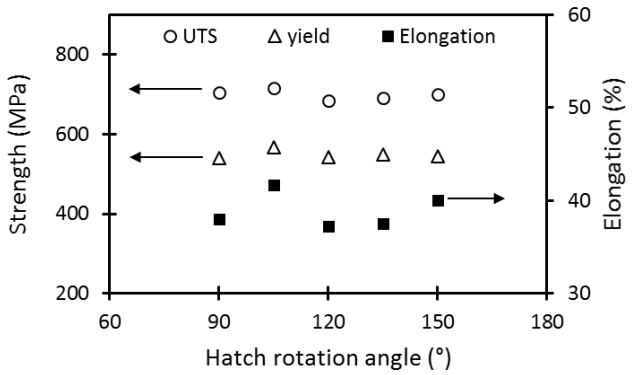

Figure 99. Effect of hatch rotation angle on the mechanical strength and ductility. Data sets adapted from Guan et al. [190]

Beam offset

The effect of beam offset (between two layers) was tested by comparing the predicted unfused fractions from two sets of deposition parameters with zero and random beam offsets, with results shown in Figure 100. Zero beam offset means that the centerlines of leftmost scans in every layer are at the same position (as seen from the section perpendicular to bottom-most scan in Figure 97). Horizontal lines in Figure 100 refer to unmelted fractions with random beam offset, whereas the data points give the results for zero beam offset (both from the full simulation). Unlike the lack of a relationship between the unmelted fraction and hatch rotation angle seen in Figure 98 (with random offsets), zero beam offset leads to a larger scatter of porosity in Figure 100, indicating that the beam offset also affects lack-of-fusion pores, for the size of area simulated here.

For the example of 67° rotation, the unmelted fraction with zero beam offset (black dot in Figure 100) is close to the average value for random offsets (horizontal line), which suggests that it is not necessary to control position of first track (*i.e.* beam offset) when starting scanning in a new layer. Rather, for zero rotation, zero beam offset results in a much higher porosity (for both deposition parameters in Figure 100). This implies that 0° rotation leads to a large variation of porosity with different beam offsets. Such an observation can be employed to realize a lower porosity with carefully selected non-random beam offset, such as half hatch spacing (see Figure 101) with more contribution to melting from the bottom region of subsequent melt pools (deeper penetration into previous layers).

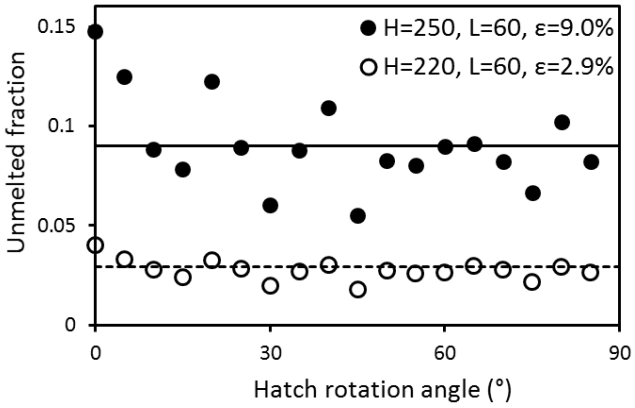

Figure 100. Unmelted fractions against hatch rotation angles, with zero beam offset applied for two hatch spacings. Dimensions are in μm; average unmelted fractions are listed in the legend and indicated by the horizontal lines.

Zero-rotation and H/2 as beam offset

Figure 101 depicts a specific combination of zero-rotation and half hatch spacing as beam offset (left) and calculated overlap between melt pools (right). The unique benefit of zero-rotation is that all the scans share the same scanning direction: consecutive melt pools in subsequent layers could potentially *eliminate* pores left by previous scans, if the thickness of vertical overlap between pools in adjacent layers (X) is larger than layer thickness (L), as shown in Figure 101. Equation 41 expresses this relationship for $X \geqslant L$.

$$\left(\frac{H}{W}\right)^4+9\left(\frac{L}{D}\right)^4+10\left(\frac{H}{W}\right)^2\left(\frac{L}{D}\right)^2-4\left(\frac{H}{W}\right)^2\le 0 \qquad \text{Equation 41}$$

Upon adding Equation 41 into the geometric model, the full-dense window is expanded to the right of the original arc (see Figure 102). It is worth noticing that although the contour of 2.5 times standard build rate is totally outside of the full-dense window in Figure 91 for non-zero rotation, it is predicted that dense parts could be produced with zero rotation at this high build rate (for carefully chosen combinations of *H/W* and *L/D*). This indicates that the approach of using a zero rotation angle and *H*/2 offset could give further improvements in build rate relative to *H-L* combinations optimized for non-zero rotation angles and random offsets.

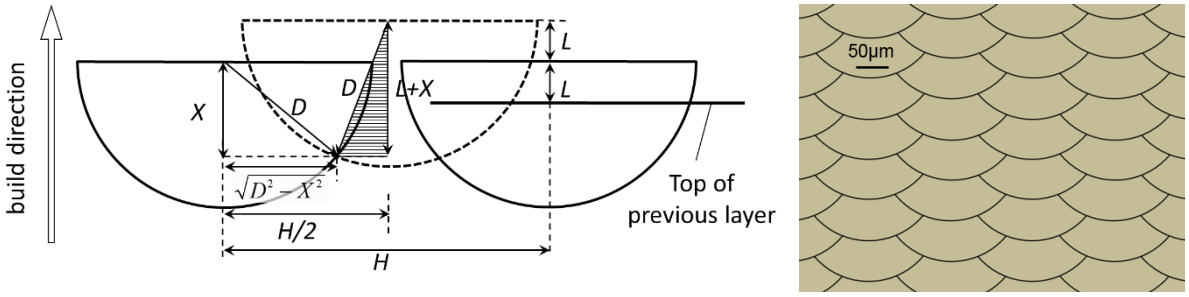

Figure 101. Schematic of geometric correlation and bead deposition pattern for zero rotation and *H*/2 as beam offset. Units are in μm: *D*=*W*/2=113, *H*=250, *L*=30. The previous criterion of Equation 12 is not satisfied: $(H/W)^2+(L/D)^2=1.32>1$.

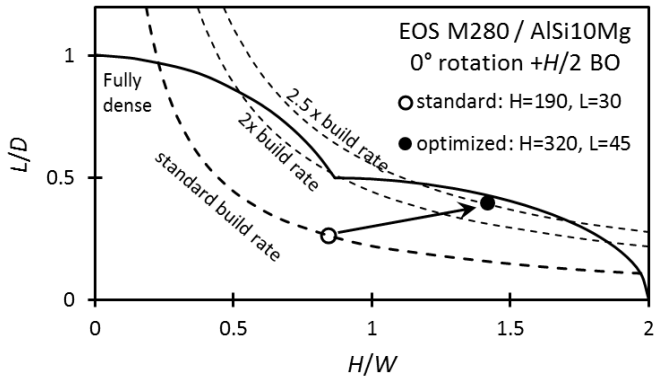

Figure 102. Processing map for zero-rotation and *H*/2 as beam offset. Units are in μm.

5 Conclusions

Hypotheses revisited

All hypotheses can be regarded as valid:

1) The Rosenthal equation from conventional welding can successfully predict the melt-pool size and local cooling rate during SLM.
2) The well-established relationship between cooling rate and length scale of solidification microstructure based on traditional aluminum-silicon alloys is applicable to the microstructures of SLM parts and gas atomized powder used for SLM.
3) Al_2O_3-containing oxide remains as isolated defects and is associated with pores in AlSi10Mg alloy parts produced by SLM.
4) The fatigue life of AlSi10Mg alloy produced by SLM is dictated by residual porosity exposed the part surface.

Microstructure

The solidification microstructure closely follows well-established relationships between cell size and solidification rate (for as-built parts) and between dendrite arm spacing and powder size (for the atomized powder). One implication is that, during part building, local control of cell spacing can be achieved directly by manipulating the local heat input.

Mechanical properties

The fatigue life of AlSi10Mg parts produced by selective laser melting (SLM), as found in this work, was similar to the earlier (limited) literature reports for parts produced by SLM of powder of this alloy, and is also comparable with that of similar aluminum alloy parts produced by conventional casting.

The relationship between fatigue life and the size of crack initiating defects followed that previously reported for similar but conventionally cast aluminum A356. What appears to be a new observation is that these defects are associated with relatively large (micron-sized or larger) oxides; these oxides likely form by oxidation of vaporized metal.

Both hatch spacing and build orientation affect the mechanical properties, and in particular the ductility (reduction in area) and fatigue resistance. Differences between the two orientations are evident both upon initial plastic flow and at final fracture in the tensile test. The *Z*-oriented samples flow at a lower imposed stress than the *XY*-oriented samples, likely because of thermal residual stress caused by the difference in the coefficients of thermal expansion of aluminum and silicon. The *Z*-oriented samples show smaller tensile ductility; for these samples, ductile fracture occurs by tearing along the softer, coarser region at the melt pool boundaries. An effect of hatch spacing indicates that porosity also affects tensile ductility.

Porosity prediction

A geometry-based simulation model has been developed to predict the volume fraction of unmelted material in parts built by power bed fusion. The input data required by the model are the shape of the melt-pool cross-section, hatch spacing, and layer thickness. Comparison with several sets of experimental data from the literature shows that the model correctly predicts process conditions beyond which lack-of-fusion porosity would be present, and the numerical value of porosity if melting is incomplete. Lack-of-fusion porosity is independent of hatch rotation angle. A specific combination of zero rotation angle and half hatch spacing as beam offset is introduced for build rate optimization.

Appendix A

Derivation of maximum melt-pool depth from Rosenthal equation

This section shows the derivation of the approximate analytical solutions for melt-pool width (W=2D) and length (L_{total}), as shown in Figure 26.

Melt-pool depth

There are two constraints when locating the position of the maximum melt-pool width: one from the initial Rosenthal equation, the other from zero slope of the contour along the edge of the melt pool (where $\partial y/\partial \xi$=0).

We start with the Rosenthal equation (Equation 16), also copied here:

$$T = T_0 + \frac{Q}{2\pi k r}\exp\left[-\frac{V(\xi + r)}{2\alpha}\right] \quad \text{Equation 16}$$

The terms of M and N are defined for simplification. M and N are positive and have the same unit of m^{-1}. For the typical SLM alloys, M is much larger than N, with AlSi10Mg as an exception.

$$M = \frac{V}{2\alpha} \quad \text{Equation 42}$$

$$N = \frac{2\pi k(T - T_0)}{Q} \quad \text{Equation 43}$$

Table 28. r (at maximum width), M/N and rM values for various materials with 100W absorbed power, 1m/s speed, no preheating (T_0=303K) and alloy properties provided in Table 12. r corresponding to maximum melt-pool width is calculated with a full numerical solution.

Material	AlSi10Mg	Maraging steel	Stainless steel	Ti64	IN625	CoCr
r (μm)	138	267	269	548	470	278
M/N (-)	2.9	91	106	257	208	113
rM (-)	1.5	32	34	95	79	35

After integrating M and N, the initial Rosenthal equation can be rearranged to:

$$\ln Nr + M(\xi + r) = 0 \qquad \text{Equation 44}$$

In solving this equation, instead of Cartesian coordinates, polar coordinates are preferred, since there is only one exact solution of r corresponding to each φ in the range from 0 to 2π, while there might be two or no ξ values for a given y. Expressing Equation 44 in polar coordinates with $\xi = r\cos\varphi$ and $y = r\sin\varphi$, as illustrated in Figure 26, we get the first governing equation:

$$\ln Nr + Mr(\cos\varphi + 1) = 0 \qquad \text{Equation 45}$$

which can also be expressed in the following form:

$$\frac{dr}{d\varphi} = \frac{r\sin\varphi}{\frac{1}{Mr} + \cos\varphi + 1} \qquad \text{Equation 46}$$

The second constraint is zero slope of the melting-pool boundary at the maximum width:

$$\frac{\partial y}{\partial \xi} = 0 \qquad \text{Equation 47}$$

from which we can get the second governing equation in the same format of $dr/d\varphi$:

$$\frac{dr}{d\varphi} = -\frac{\cos\varphi}{\sin\varphi} r \qquad \text{Equation 48}$$

Combining Equation 46 and Equation 48 allows φ at maximum depth to be expressed as a function of r and M:

$$\cos\varphi = \frac{-rM}{1 + rM} \qquad \text{Equation 49}$$

$$\sin\varphi = \frac{\sqrt{1 + 2rM}}{1 + rM} \qquad \text{Equation 50}$$

Then combining Equation 49 with Equation 45, in order to reduce the number of unknown parameters from two (r and φ) to one (r), we obtain:

$$\ln Nr + Mr(\ln Nr + 1) = 0 \qquad \text{Equation 51}$$

The term ($\ln Nr+1$) has to be near zero to satisfy this relationship, since Mr is generally much larger than $\ln Nr$ (true for all materials in Table 28 except AlSi10Mg, mainly because of its large N value due to the high thermal conductivity). The relationship $\ln Nr+1 \approx 0$ then gives:

$$r \approx \frac{1}{eN} \qquad \text{Equation 52}$$

Combining Equation 50 and Equation 52 to give the maximum melt-pool depth (approximation for sinφ is for large values of *rM*, as indicated in Table 28)

$$y_{\max} = r\sin\varphi = r\left(\frac{\sqrt{1+2rM}}{1+rM}\right) \approx r\frac{\sqrt{2rM}}{rM} = \sqrt{\frac{2}{eMN}} \qquad \text{Equation 53}$$

The final expression for maximum width and depth is as follows:

$$D = \frac{1}{2}W = y_{\max} \approx \sqrt{\frac{2Q}{e\pi\rho C\left(T-T_0\right)V}} \qquad \text{Equation 20}$$

Melt-pool length along scan direction

As can be seen from Figure 28, the tail length (ξ<0) accounts for most of the melt pool length along the scan direction. We can take ξ=-*r* (*y*=*z*=0) to get the following relationship from Equation 44:

$$L_{total} \approx r_{tail} = \frac{1}{N} = \frac{Q}{2\pi k\left(T-T_0\right)} \qquad \text{Equation 22}$$

Power required to obtain a certain melt-pool size

Equation 20 can be applied to calculate possible *Q*-*V* combinations for a given melt-pool depth. However, it is limited to the condition of non-zero scan speed. Consequently, an extra term of beam power is required to obtain the depth at zero speed, to ensure that the intercepts of melt-pool depth contour plots with the vertical axis (*Q*) are non-zero. Equation 54 below is rearranged from Equation 20, and Equation 55 is directly solved from the Rosenthal equation with *V* equal to zero.

$$Q_{V>0} \approx 0.5e\pi\rho C\left(T-T_0\right)VD^2 \qquad \text{Equation 54}$$

$$Q_{V=0} \approx 2\pi k\left(T-T_0\right)r_{V=0} = 2\pi k\left(T-T_0\right)D \qquad \text{Equation 55}$$

So the absorbed power to achieve a certain melt-pool depth is approximated as follows (for all alloys in Table 12 except AlSi10Mg):

$$Q \approx Q_{V=0} + Q_{V>0} \approx 2\pi k(T - T_0)D + 0.5e\pi\rho C(T - T_0)VD^2 \qquad \text{Equation 25}$$

In order to let the relationship work for (high-conductivity) aluminum alloys, an additional fitting factor of 0.8 is applied to improve the correspondence between the numerical result and the approximate analytical solution (bottom right graph in Figure 29):

$$Q \approx Q_{V=0} + 0.8 \times Q_{V>0} \approx 2\pi k(T - T_0)D + 0.4e\pi\rho C(T - T_0)VD^2 \qquad \text{Equation 24}$$

Appendix B

Images during the automated feature detection by 2D SEM

This section shows the 30 largest features detected by automated analysis on a polished section (area 14mm^2) of the sample built with 0.19mm hatch spacing. All backscattered electron images were taken after analysis. One thing worth noticing is that sites 4 and 26 are identical, but this single site contains multiple features and the analysis software reported pores and oxides separately. Furthermore, it is also interesting to note the morphology of the oxide particles: a few oxide particles contain internal pores, such as those sites 11 and 16 in Table 29 and one inside the pore in Figure 83. These pores might give insights into the formation mechanism of the oxides upon more in-depth study.

Table 29. Backscattered electron images of the 30 largest features for the sample built with 0.19mm hatch spacing. Arrows indicate oxide particles.

1	2	3
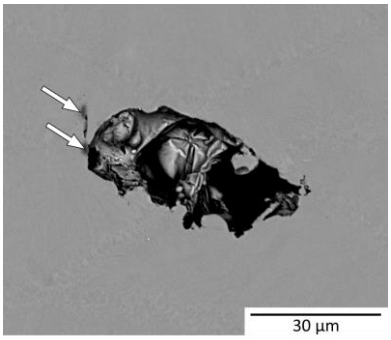	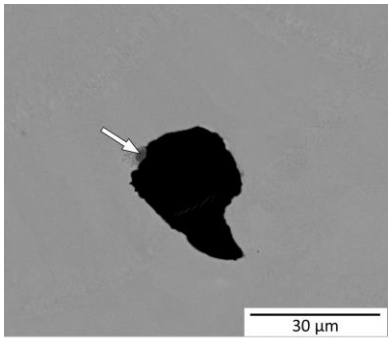	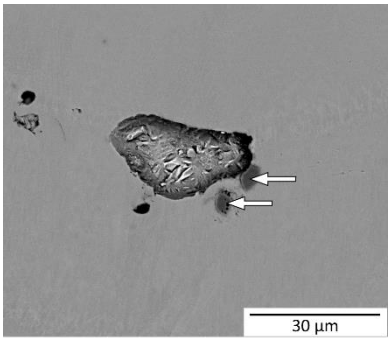
4	5	6
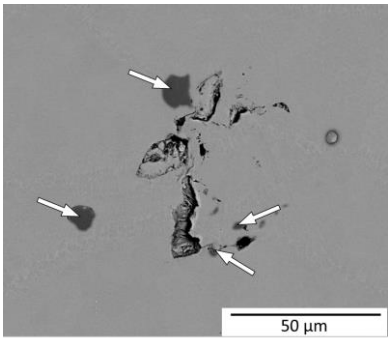	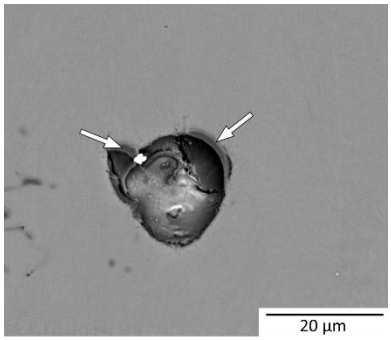	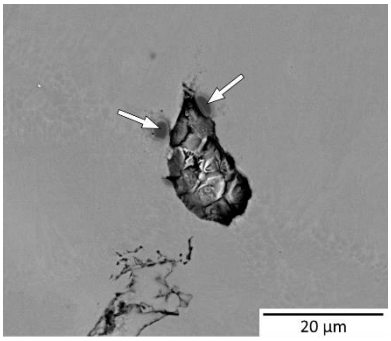
7	8	9

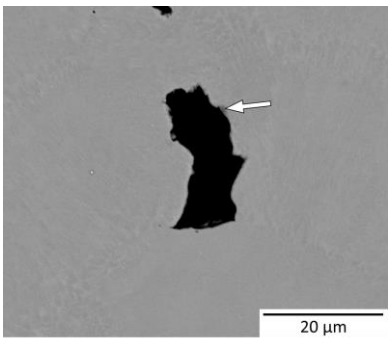

10

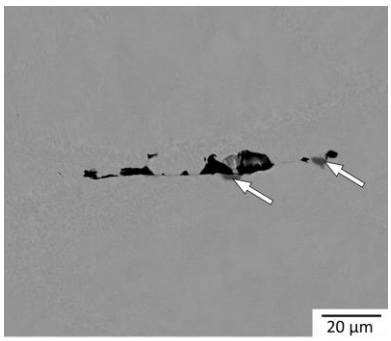

11

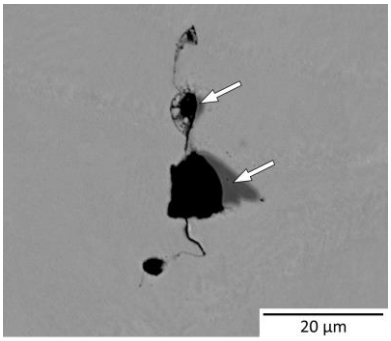

12

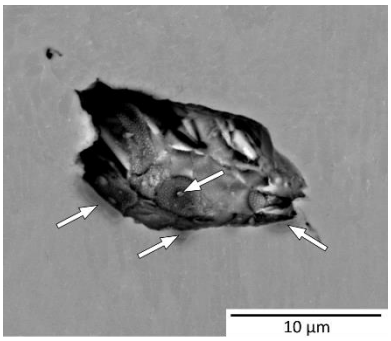

13

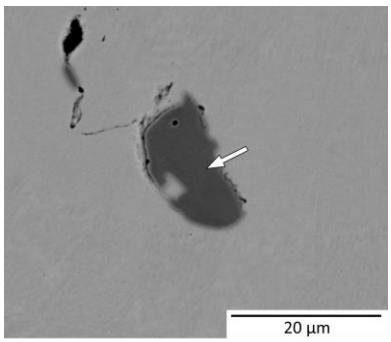

14

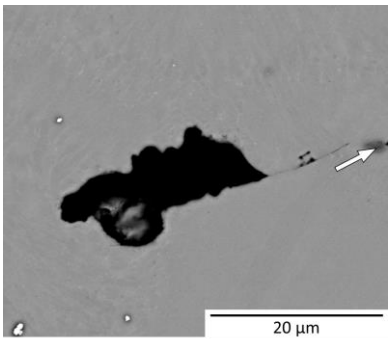

15

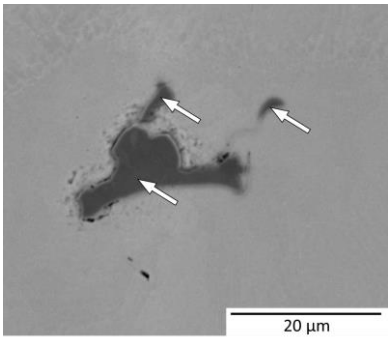

16

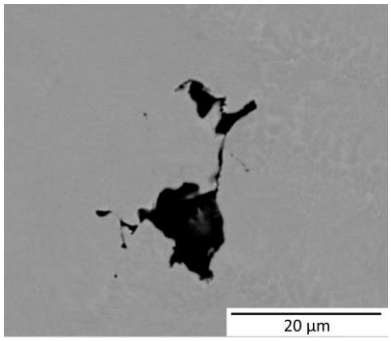

17

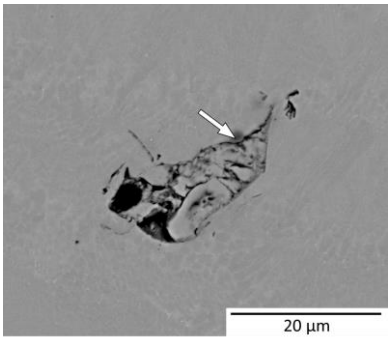

18

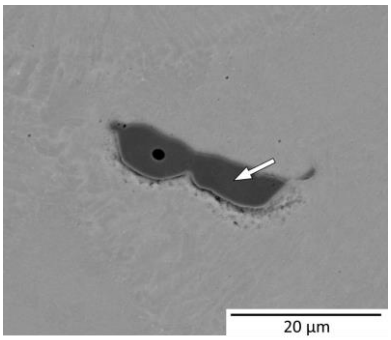

19

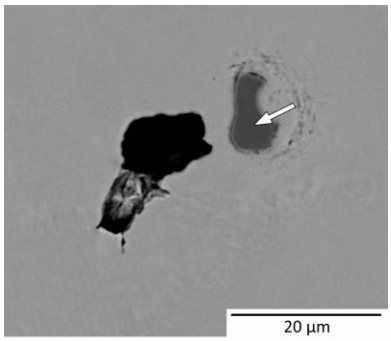

20

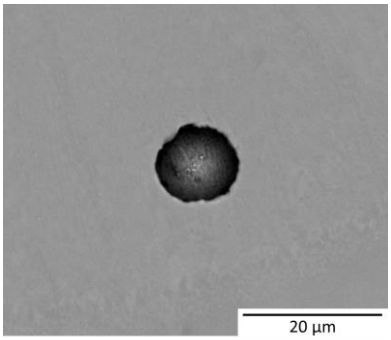

21

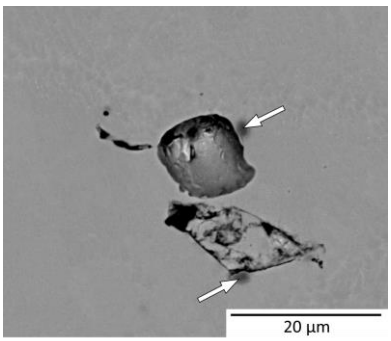

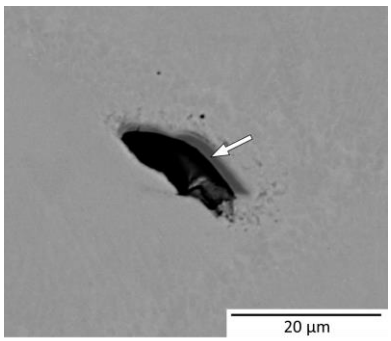

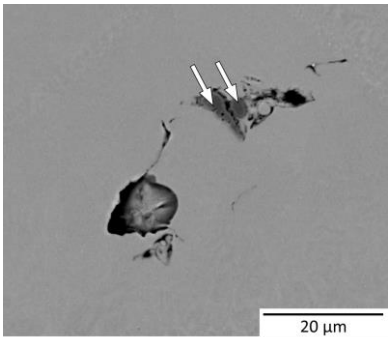

22

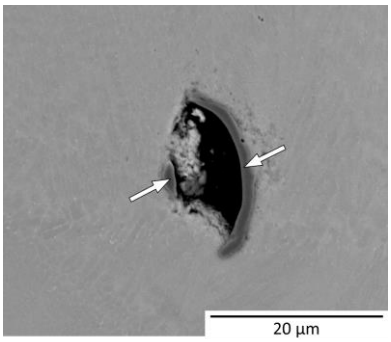

23

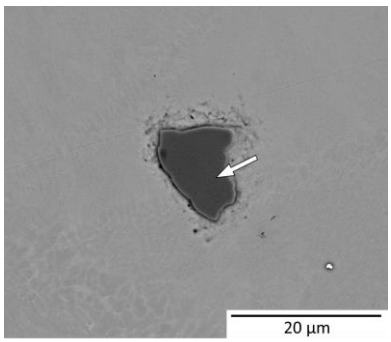

24

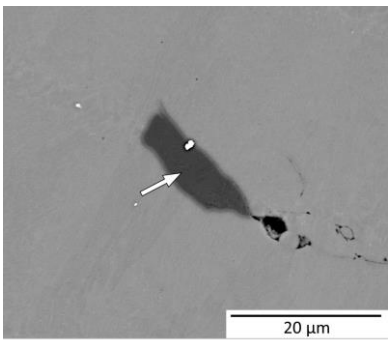

25

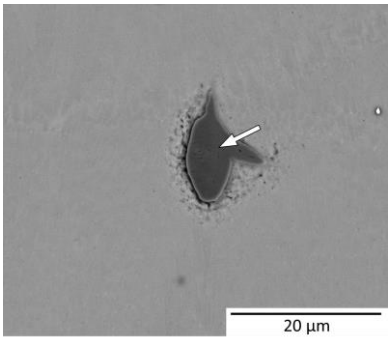

26

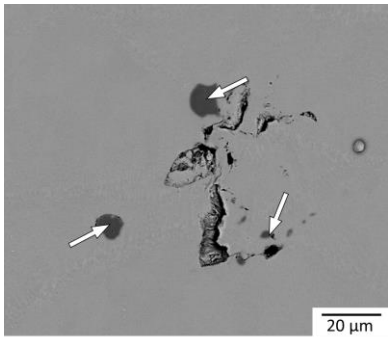

27

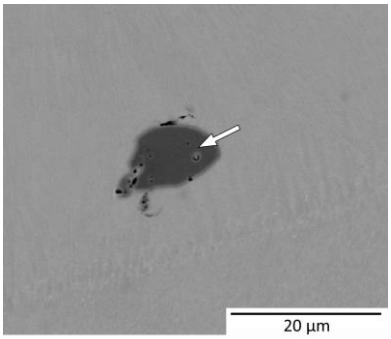

28

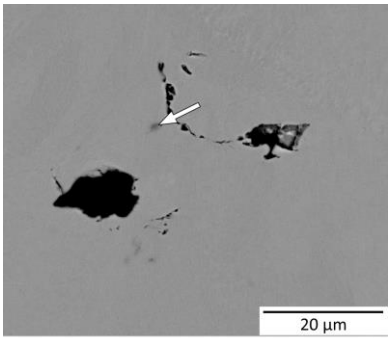

29

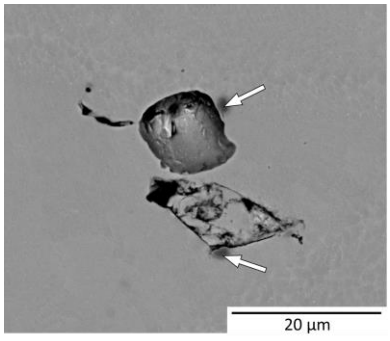

30

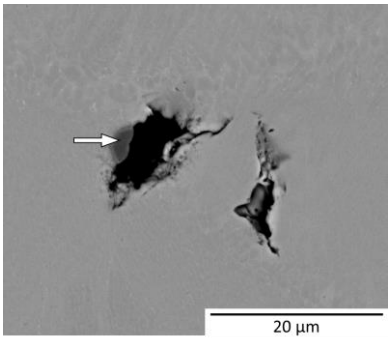

Appendix C

List of Publications and Presentations

Journal papers

M. Tang and P. C. Pistorius, "Anisotropic Mechanical Behavior of AlSi10Mg Parts Produced by Selective Laser Melting," *JOM*, vol. 69, pp. 516–522, 2017. DOI: 10.1007/s11837-016-2230-5

M. Tang, P. C. Pistorius, and J.L. Beuth, "Prediction of Lack-of-fusion Porosity for Powder Bed Fusion," *Addit. Manuf.*, vol. 14, pp. 39-48, 2017. DOI: 10.1016/j.addma.2016.12.001

M. Tang and P. C. Pistorius, "Oxide, Porosity and Fatigue performance of AlSi10Mg Parts Produced by Selective Laser Melting," *Int. J. Fatigue*, vol. 94, pp. 192-201, 2016. DOI: 10.1016/j.ijfatigue.2016.06.002

M. Tang, P. C. Pistorius, S. Narra, and J.L. Beuth, "Rapid Solidification: Selective Laser Melting of AlSi10Mg," *JOM*, vol. 68, pp. 960-966, 2016. DOI: 10.1007/s11837-015-1763-3

Conference proceedings

M. Tang, P. C. Pistorius, and J.L. Beuth, "Geometric Model to Predict Porosity of Part Produced in Powder Bed System," in *Materials Science & Technology*, Columbus, OH, 2015, pp. 129-136.

Conference Presentations

M. Tang and P. C. Pistorius, "Fatigue Life Prediction for AlSi10Mg Parts Produced by Selective Laser Melting," *RAPID + TCT Conference*, Pittsburgh, PA, May 2017.

M. Tang and P. C. Pistorius, "Anisotropic Mechanical Behavior of AlSi10Mg Parts Produced by Selective Laser Melting," *TMS*, San Diego, CA, Mar 2017.

M. Tang and P. C. Pistorius, "Relationship between Porosity Size and Fatigue Life Distributions of AlSi10Mg Parts Produced by Selective Laser Melting," *MS&T*, Salt Lake City, UT, 2016.

M. Tang, P. C. Pistorius, “Oxide, Porosity, and Fatigue Performance of AlSi10Mg Parts Produced by Selective Laser Melting,” *TMS*, Nashville, TN, 2016.

M. Tang, P. C. Pistorius, and J.L. Beuth, “Geometric Model to Predict Porosity of Part Produced in Powder Bed System,” *MS&T*, Columbus, OH, 2015.

6 References

[1] ASTM Committee F42, "ISO / ASTM 52900-15: Standard Terminology for Additive Manufacturing Technologies - General Principles - Terminology," *ASTM International*. ASTM International, 2015.

[2] ASTM Committee F42, "ISO/ASTM 52921-2013: Standard Terminology for Additive Manufacturing - Coordinate Systems and Test Methodologies," *ASTM International*. ASTM International, West Conshohocken, PA, 2013.

[3] ASTM Committee F42, "ASTM F3122-14: Standard Guide for Evaluating Mechanical Properties of Metal Materials Made via Additive Manufacturing Processes," *ASTM International*. ASTM International, 2014.

[4] ASTM Committee F42, "ASTM F3049-14: Standard Guide for Characterizing Properties of Metal Powders Used for Additive Manufacturing Processes," *ASTM International*. ASTM International, 2014.

[5] ASTM Committee F42, "ASTM F2924-14: Standard Specification for Additive Manufacturing Titanium-6 Aluminum-4 Vanadium with Powder Bed Fusion," *ASTM International*. ASTM International, 2014.

[6] W. J. Sames, F. A. List, S. Pannala, R. R. Dehoff, and S. S. Babu, "The metallurgy and processing science of metal additive manufacturing," *Int. Mater. Rev.*, vol. 61, pp. 315–360, 2016.

[7] W. E. Frazier, "Metal additive manufacturing: A review," *J. Mater. Eng. Perform.*, vol. 23, no. 6, pp. 1917–1928, 2014.

[8] D. Gu, W. Meiners, K. Wissenbach, and R. Poprawe, "Laser additive manufacturing of metallic components: materials, processes and mechanisms," *Int. Mater. Rev.*, vol. 57, no. 3, pp. 133–164, 2012.

[9] E. Herderick, "Additive manufacturing of metals: A review," in *Materials Science and Technology (MS&T)*, 2011, vol. 2, no. 176252, pp. 1413–1425.

[10] J. Kruth, M. Badrossamay, E. Yasa, J. Deckers, L. Thijs, and J. Van Humbeeck, "Part and material properties in selective laser melting of metals," in *Proceedings of the 16th international symposium on electromachining*, 2010.

[11] A. M. Beese and B. E. Carroll, "Review of Mechanical Properties of Ti-6Al-4V Made by Laser-Based Additive Manufacturing Using Powder Feedstock," *JOM*, vol. 68, no. 3, pp. 724–734, 2016.

[12] J. J. Lewandowski and M. Seifi, "Metal Additive Manufacturing: A Review of Mechanical Properties," *Annu. Rev. Mater. Res.*, vol. 46, pp. 151–186, 2016.

[13] A. I. Mertens, J. Delahaye, and J. Lecomte-Beckers, "Fusion-Based Additive Manufacturing for Processing Aluminum Alloys: State-of-the-Art and Challenges," *Adv. Eng. Mater.*, p. 1700003, 2017.

[14] I. Gibson, D. W. Rosen, and B. Stucker, *Additive manufacturing technologies*. New York: Springer, 2010.

[15] D. Gu, *Laser Additive Manufacturing of High-Performance Materials*. Springer, 2015.

[16] T. S. Srivatsan and T. S. Sudarshan, Eds., *Additive Manufacturing: Innovations, Advances,*

and Applications. CRC Press, 2015.

[17] M. Seifi, A. Salem, J. Beuth, O. Harrysson, and J. J. Lewandowski, "Overview of Materials Qualification Need for Metal Additive Manufacturing," *JOM*, vol. 68, no. 9, pp. 747–764, 2016.

[18] Consortium for Additive Manufacturing Materials (CAMM), "Strategic Roadmap for the Next Generation of Additive Manufacturing Materials," 2015.

[19] D. L. Bourell, M. C. Leu, and D. W. Rosen, "Roadmap for Additive Manufacturing: Identifying the Future of Freeform Processing," Austin, TX, 2009.

[20] C. Brown, J. Lubell, and R. Lipman, "Additive Manufacturing Technical Workshop Summary Report, NIST Technical Note 1823," Gaithersburg, MD, 2013.

[21] Y. Huang and M. C. L. March, "Frontiers of Additive Manufacturing Research and Education," Gainesville, FL, 2014.

[22] J. M. Waller, B. H. Parker, K. L. Hodges, E. R. Burke, and J. L. Walker, "Nondestructive Evaluation of Additive Manufacturing State-of-the-Discipline Report," Las Cruces, NM, 2014.

[23] D. Rosenthal, "Mathematical theory of heat distribution during welding and cutting," *Weld. J.*, vol. 20, no. 5, pp. 220–234, 1941.

[24] K. Kempen, L. Thijs, J. Van Humbeeck, and J.-P. Kruth, "Processing AlSi10Mg by selective laser melting: parameter optimisation and material characterisation," *Mater. Sci. Technol.*, vol. 31, no. 8, pp. 917–923, 2015.

[25] J. E. Hatch, "Constitution of Alloys," in *Aluminum: Properties and Physical Metallurgy*, Metals Park, Ohio: American Society for Metals, 1984, p. 48.

[26] J. F. Major and R. T. Alcan, "Aluminum and aluminum alloy castings," in *ASM Handbook Volume 15: Casting*, ASM International Handbook Committee, Ed. Metals Park, Ohio: ASM International, 2008, pp. 1059–1084.

[27] R. N. Lumley, T. B. Sercombe, and G. M. Schaffer, "Surface oxide and the role of magnesium during the sintering of aluminum," *Metall. Mater. Trans. A*, vol. 30, no. 2, pp. 457–463, 1999.

[28] L. Thijs, K. Kempen, J. P. Kruth, and J. Van Humbeeck, "Fine-structured aluminium products with controllable texture by selective laser melting of pre-alloyed AlSi10Mg powder," *Acta Mater.*, vol. 61, no. 5, pp. 1809–1819, 2013.

[29] EOS GmbH – Electro Optical Systems, "Material data sheet: EOS Aluminium AlSi10Mg (for EOS M280)," 2016. [Online]. Available: http://www.eos.info/material-m. [Accessed: 11-Oct-2016].

[30] E. Scheil, "Bemerkungen zur Schichtkristallbildung," *Zeitschrift für Met.*, vol. 34, no. 3, pp. 70–72, 1942.

[31] J. L. Murray and A. J. McAlister, "The Al-Si (Aluminum-Silicon) System," *J. Phase Equilibria*, vol. 5, no. 1, pp. 74–84, 1984.

[32] K. G. Prashanth, S. Scudino, H. J. Klauss, K. B. Surreddi, L. Löber, Z. Wang, A. K. Chaubey, U. Kühn, and J. Eckert, "Microstructure and mechanical properties of Al-12Si produced by selective laser melting: Effect of heat treatment," *Mater. Sci. Eng. A*, vol. 590, pp. 153–160, 2014.

[33] J. D. Hunt and S. Z. Lu, "Numerical modelling of cellular and dendritic array growth: spacing and structure predictions," *Mater. Sci. Eng. A*, vol. 173, no. 1–2, pp. 79–83, 1993.

[34] D. Bouchard and J. S. Kirkaldy, "Equations and Specification of Predictive Procedures," *Metall. Mater. Trans. B*, vol. 28B, no. 4, pp. 651–663, 1996.

[35] S. Kou, "Basic Solidification Concepts," in *Welding Metallurgy*, 2nd ed., John Wiley & Sons, 2003, p. 166.

[36] J. A. Dantzig and M. Rappaz, "Dendritic Growth," in *Solidification*, CRC Press, 2009, pp. 302, 327.

[37] N. J. Grant, "Rapid Solidification of Metallic Particulates," *JOM*, pp. 20–27, 1983.

[38] H. J. Hegge and J. T. M. D. Hosson, "Solidification structures during laser treatment," *Scr. Metall.*, vol. 24, pp. 593–599, 1990.

[39] J. E. Hatch, "Metallurgy of heat treatment and general principles of precipitation hardening," in *Aluminum: Properties and Physical Metallurgy*, Metals Park, Ohio: American Society for Metals, 1984, pp. 134–159.

[40] M. H. Mülazımoğlu, R. A. L. Drew, and J. E. Gruzleski, "Solution Treatment Study of Cast Al-Si Alloys by Electrical Conductivity," *Can. Metall. Q.*, vol. 28, no. 3, pp. 251–258, 1989.

[41] M. H. Mülazımoğlu, "ELECTRICAL CONDUCTIVITY STUDIES OF CAST AI-Si AND AI-Si-Mg ALLOYS," McGill University, 1988.

[42] J. K. Chen, H. Y. Hung, C. F. Wang, and N. K. Tang, "Effects of casting and heat treatment processes on the thermal conductivity of an Al-Si-Cu-Fe-Zn alloy," *Int. J. Heat Mass Transf.*, vol. 105, pp. 189–195, 2017.

[43] J. E. Hatch, "Effects of alloying elements and impurities on properties," in *Aluminum: Properties and Physical Metallurgy*, Metals Park, Ohio: American Society for Metals, 1984, pp. 204–205.

[44] W. Li, S. Li, J. Liu, A. Zhang, Y. Zhou, Q. Wei, C. Yan, and Y. Shi, "Effect of heat treatment on AlSi10Mg alloy fabricated by selective laser melting: Microstructure evolution, mechanical properties and fracture mechanism," *Mater. Sci. Eng. A*, vol. 663, pp. 116–125, 2016.

[45] E. Brandl, U. Heckenberger, V. Holzinger, and D. Buchbinder, "Additive manufactured AlSi10Mg samples using Selective Laser Melting (SLM): Microstructure, high cycle fatigue, and fracture behavior," *Mater. Des.*, vol. 34, pp. 159–169, 2012.

[46] J. Fiocchi, a. Tuissi, P. Bassani, and C. a. Biffi, "Low temperature annealing dedicated to AlSi10Mg selective laser melting products," *J. Alloys Compd.*, vol. 695, pp. 3402–3409, 2016.

[47] X. P. Li, X. J. Wang, M. Saunders, A. Suvorova, L. C. Zhang, Y. J. Liu, M. H. Fang, Z. H. Huang, and T. B. Sercombe, "A selective laser melting and solution heat treatment refined Al-12Si alloy with a controllable ultrafine eutectic microstructure and 25% tensile ductility," *Acta Mater.*, vol. 95, pp. 74–82, 2015.

[48] D. Buchbinder and W. Meiners, "Generative Fertigung von Aluminiumbauteilen für die Serienproduktion," *Förderkennzeichen 01RI0639A-D. Aachen Fraunhofer Inst. Laser Technol. ILT*, pp. 1–148, 2010.

[49] N. T. Aboulkhair, I. Maskery, I. Ashcroft, C. Tuck, and N. M. Everitt, "The role of powder properties on the processability of aluminium alloys in selective laser melting," in *22nd*

World of Photonics Congress: Lasers in Manufacturing conference, 2015.

[50] E. O. Olakanmi, R. F. Cochrane, and K. W. Dalgarno, "A review on selective laser sintering/melting (SLS/SLM) of aluminium alloy powders: Processing, microstructure, and properties," *Prog. Mater. Sci.*, vol. 74, pp. 401–477, 2015.

[51] N. T. Aboulkhair, N. M. Everitt, I. Ashcroft, and C. Tuck, "Reducing porosity in AlSi10Mg parts processed by selective laser melting," *Addit. Manuf.*, vol. 1, pp. 77–86, 2014.

[52] M. Krishnan, E. Atzeni, R. Canali, F. Calignano, D. Manfredi, E. P. Ambrosio, and L. Iuliano, "On the effect of process parameters on properties of AlSi10Mg parts produced by DMLS," *Rapid Prototyp. J.*, pp. 449–458, 2014.

[53] C. Weingarten, D. Buchbinder, N. Pirch, W. Meiners, K. Wissenbach, and R. Poprawe, "Formation and reduction of hydrogen porosity during selective laser melting of AlSi10Mg," *J. Mater. Process. Technol.*, vol. 221, pp. 112–120, 2015.

[54] I. Rosenthal, A. Stern, and N. Frage, "Microstructure and Mechanical Properties of AlSi10Mg Parts Produced by the Laser Beam Additive Manufacturing (AM) Technology," *Metallogr. Microstruct. Anal.*, vol. 3, no. 6, pp. 448–453, 2014.

[55] N. Read, W. Wang, K. Essa, and M. M. Attallah, "Selective laser melting of AlSi10Mg alloy: Process optimisation and mechanical properties development," *Mater. Des.*, vol. 65, pp. 417–424, 2015.

[56] F. Calignano, D. Manfredi, E. P. Ambrosio, L. Iuliano, and P. Fino, "Influence of process parameters on surface roughness of aluminum parts produced by DMLS," *Int. J. Adv. Manuf. Technol.*, vol. 67, no. 9–12, pp. 2743–2751, 2013.

[57] N. T. Aboulkhair, I. Maskery, C. Tuck, I. Ashcroft, and N. Everitt, "Nano-hardness and microstructure of selective laser melted AlSi10Mg scan tracks," in *Industrial Laser Applications Symposium 2015*, vol. 9657, M. Green, Ed. Kenilworth, United Kingdom: International Society for Optics and Photonics, 2015, pp. 965702-965702–7.

[58] I. Maskery, N. T. Aboulkhair, C. Tuck, R. D. Wildman, I. A. Ashcroft, N. M. Everitt, and R. J. M. Hague, "Fatigue performance enhancement of selectively laser melted aluminium alloy by heat treatment," in *Solid Freeform Fabrication Symposium*, Austin, TX, 2015, pp. 1017–1025.

[59] S. Siddique, M. Imran, E. Wycisk, C. Emmelmann, and F. Walther, "Influence of process-induced microstructure and imperfections on mechanical properties of AlSi12 processed by selective laser melting," *J. Mater. Process. Technol.*, vol. 221, pp. 205–213, 2015.

[60] D. Manfredi, F. Calignano, M. Krishnan, R. Canali, E. P. Ambrosio, and E. Atzeni, "From powders to dense metal parts: Characterization of a commercial AlSiMg alloy processed through direct metal laser sintering," *Materials.*, vol. 6, no. 3, pp. 856–869, 2013.

[61] K. Kempen, L. Thijs, J. Van Humbeeck, and J.-P. Kruth, "Mechanical Properties of AlSi10Mg Produced by Selective Laser Melting," *Phys. Procedia*, vol. 39, pp. 439–446, 2012.

[62] ASTM Committee B07, "ASTM B85/B85M-14: Standard Specification for Aluminum-Alloy Die Castings," *ASTM International*. ASTM International, 2013.

[63] A. L. Kearney, "Properties of Cast Aluminum Alloys," in *ASM Handbook Volume 2: Properties and Selection: Nonferrous Alloys and Special-Purpose Materials*, ASM handbook committee, Ed. ASM International, 1990, pp. 152–177.

[64] J. G. Kaufman, “Presentation of Fatigue Data,” in *Properties of aluminum alloys: fatigue data and the effects of temperature, product form, and processing*, Metals Park, Ohio: ASM International, 2008, p. 15.

[65] G. E. Dieter, “Mechanical Metallurgy,” 3rd ed., McGraw-Hill Book Company, 1988, pp. 231–233, 322, 400, 407–412.

[66] A. A. Benzerga, J. Besson, and A. Pineau, “Anisotropic ductile fracture: Part I: Experiments,” *Acta Mater.*, vol. 52, no. 15, pp. 4623–4638, 2004.

[67] A. A. Benzerga, J. Besson, and A. Pineau, “Anisotropic ductile fracture: Part II: Theory,” *Acta Mater.*, vol. 52, no. 15, pp. 4639–4650, 2004.

[68] T. F. Morgeneyer, M. J. Starink, and I. Sinclair, “Evolution of voids during ductile crack propagation in an aluminium alloy sheet toughness test studied by synchrotron radiation computed tomography,” *Acta Mater.*, vol. 56, no. 8, pp. 1671–1679, 2008.

[69] D. Steglich, W. Brocks, J. Heerens, and T. Pardoen, “Anisotropic ductile fracture of Al 2024 alloys,” *Eng. Fract. Mech.*, vol. 75, no. 12, pp. 3692–3706, 2008.

[70] P. J. E. Forsyth and C. A. Stubbington, “Directionality in structure-property relationship: aluminum and titanium alloys,” *Met. Technol.*, pp. 158–177, 1975.

[71] B. E. Carroll, T. A. Palmer, and A. M. Beese, “Anisotropic tensile behavior of Ti-6Al-4V components fabricated with directed energy deposition additive manufacturing,” *Acta Mater.*, vol. 87, pp. 309–320, 2015.

[72] T. Niendorf, S. Leuders, A. Riemer, H. A. Richard, T. Tröster, and D. Schwarze, “Highly anisotropic steel processed by selective laser melting,” *Metall. Mater. Trans. B*, vol. 44, no. 4, pp. 794–796, 2013.

[73] T. Vilaro, C. Colin, and J. D. Bartout, “As-fabricated and heat-treated microstructures of the Ti-6Al-4V alloy processed by selective laser melting,” *Metall. Mater. Trans. A Phys. Metall. Mater. Sci.*, vol. 42, no. 10, pp. 3190–3199, 2011.

[74] EOS GmbH – Electro Optical Systems, “Material data sheets: EOS Aluminium AlSi10Mg (for EOS M270),” 2014. [Online]. Available: http://www.eos.info/material-m. [Accessed: 17-Nov-2014].

[75] T. M. Mower and M. J. Long, “Mechanical behavior of additive manufactured, powder-bed laser-fused materials,” *Mater. Sci. Eng. A*, vol. 651, pp. 198–213, 2016.

[76] N. D. Alexopoulos and M. Tiryakioğlu, “On the uniform elongation of cast Al-7%Si-0.6%Mg (A357) alloys,” *Mater. Sci. Eng. A*, vol. 507, no. 1–2, pp. 236–240, 2009.

[77] J. Hollomon, “Tensile deformation,” *Trans. Am. Inst. Min. Metall. Eng.*, vol. 162, pp. 268–290, 1945.

[78] U. F. Kocks, “Laws for Work-Hardening and Low-Temperature Creep,” *J. Eng. Mater. Technol.*, pp. 76–85, 1976.

[79] U. F. Kocks and H. Mecking, “Physics and phenomenology of strain hardening: The FCC case,” *Prog. Mater. Sci.*, vol. 48, no. 3, pp. 171–273, 2003.

[80] H. Mecking and U. F. Kocks, “Kinetics of flow and strain-hardening,” *Acta Metall.*, vol. 29, no. 11, pp. 1865–1875, 1981.

[81] E. Voce, “The relationship between stress and strain for homogeneous deformation,” *J. Inst. Met.*, vol. 74, pp. 537–562, 1948.

[82] E. Voce, “A Practical Strain-hardening Function,” *Metallurgia*, vol. 51, pp. 219–226, 1955.

[83] Q. G. Wang, D. Apelian, and D. A. Lados, “Fatigue behavior of A356-T6 aluminum cast alloys. Part I. Effect of casting defects,” *J. Light Met.*, vol. 1, no. 1, pp. 73–84, 2001.

[84] Q. G. Wang, D. Apelian, and D. A. Lados, “Fatigue behavior of A356/357 aluminum cast alloys. Part II - Effect of microstructural constituents,” *J. Light Met.*, vol. 1, no. 1, pp. 85–97, 2001.

[85] G. Sigworth, “Understanding quality in aluminum castings,” *Int. J. Met.*, vol. 5, no. 1, pp. 7–22, 2011.

[86] Q. G. Wang, C. J. Davidson, J. R. Griffiths, and P. N. Crepeau, “Oxide films, pores and the fatigue lives of cast aluminum alloys,” *Metall. Mater. Trans. B*, vol. 37B, no. 6, pp. 887–895, 2006.

[87] M. Tiryakioğlu, “On fatigue life variability in cast Al-10%Si-Mg alloys,” *Mater. Sci. Eng. A*, vol. 527, no. 6, pp. 1560–1564, 2010.

[88] A. T. Stewart, “The influence of environment and stress ratio on fatigue crack growth at near threshold stress intensities in low-alloy steels,” *Eng. Fract. Mech.*, vol. 13, no. 3, pp. 463–478, 1980.

[89] R. S. Piascik and R. P. Gangloff, “Environmental fatigue of an Al-Li-Cu alloy: part I. Intrinsic crack propagation kinetics in hydrogenous environments,” *Metall. Trans. A*, vol. 22, no. 10, pp. 2415–2428, 1991.

[90] R. S. Piascik and R. P. Gangloff, “Environmental fatigue of an Al-Li-Cu alloy: Part II. Microscopic hydrogen cracking processes,” *Metall. Trans. A*, vol. 24, no. 12, pp. 2751–2762, 1993.

[91] ASTM Committee E08, “ASTM E466-07: Standard Practice for Conducting Force Controlled Constant Amplitude Axial Fatigue Tests of Metallic Materials,” *ASTM International*. ASTM International, West Conshohocken, PA, 2007.

[92] Y. Murakami and H. Usuki, “Quantitative Evaluation of Effects of Non-Metallic Inclusions on Fatigue-Strength of High Strength Steels .2. Fatigue Limit Evaluation Based on Statistics for Extreme Values of Inclusion Size,” *Int. J. Fatigue*, vol. 11, no. 5, pp. 299–307, 1989.

[93] Y. Murakami and M. Endo, “Effects of defects, inclusions and inhomogeneities on fatigue strength,” *Int. J. Fatigue*, vol. 16, no. 3, pp. 163–182, 1994.

[94] M. Tiryakioğlu, “Relationship between defect size and fatigue life distributions in Al-7 Pct Si-Mg alloy castings,” *Metall. Mater. Trans. A Phys. Metall. Mater. Sci.*, vol. 40, no. 7, pp. 1623–1630, 2009.

[95] A. Wormsen, B. Sjödin, G. Härkegård, and A. Fjeldstad, “Non-local stress approach for fatigue assessment based on weakest-link theory and statistics of extremes,” *Fatigue Fract. Eng. Mater. Struct.*, vol. 30, no. 12, pp. 1214–1227, 2007.

[96] B. Gnedenko, “Sur La Distribution Limite Du Terme Maximum D’Une Serie Aleatoire,” *Ann. Math.*, vol. 44, no. 3, pp. 423–453, 1943.

[97] “CumFreq.” [Online]. Available: http://www.waterlog.info/. [Accessed: 25-Mar-2017].

[98] J. Z. Yi, Y. X. Gao, P. D. Lee, H. M. Flower, and T. C. Lindley, “Scatter in fatigue life due to effects of porosity in cast A356-T6 aluminum-silicon alloys,” *Metall. Mater. Trans. A*, vol. 34, no. 9, pp. 1879–1890, 2003.

[99] J. Z. Yi, P. D. Lee, T. C. Lindley, and T. Fukui, "Statistical modeling of microstructure and defect population effects on the fatigue performance of cast A356-T6 automotive components," *Mater. Sci. Eng. A*, vol. 432, no. 1–2, pp. 59–68, 2006.

[100] Y. X. Gao, J. Z. Yi, P. D. Lee, and T. C. Lindley, "The effect of porosity on the fatigue life of cast aluminium-silicon alloys," *Fatigue Fract. Eng. Mater. Struct.*, vol. 27, no. 7, pp. 559–570, 2004.

[101] P. Paris and F. Erdogan, "A critical analysis of crack propagation laws," *Trans. AS M E*, pp. 528–534, 1963.

[102] B. Skallerud, T. Iveland, and G. Härkegård, "Fatigue life assessment of aluminum alloys with casting defects," *Eng. Fract. Mech.*, vol. 44, no. 6, pp. 857–874, 1993.

[103] S. Barter, L. Molent, N. Goldsmith, and R. Jones, "An experimental evaluation of fatigue crack growth," *Eng. Fail. Anal.*, vol. 12, no. 1, pp. 99–128, 2005.

[104] C. J. Davidson, J. R. Griffiths, and A. S. Machin, "The effect of solution heat-treatment time on the fatigue properties of an Al-Si-Mg casting alloy," *Fatigue Fract. Eng. Mater. Struct.*, vol. 25, no. 2, pp. 223–230, 2002.

[105] M. Tang, P. C. Pistorius, and J. Beuth, "Geometric Model to Predict Porosity of Part Produced in Powder Bed System," in *Materials Science & Technology Proceedings (MS&T)*, Columbus, Ohio, 2015, pp. 129–136.

[106] ASTM Committee B07, "ASTM B557-15: Standard Test Methods for Tension Testing Wrought and Cast Aluminum- and Magnesium-Alloy Products," *ASTM International*. ASTM International, 2015.

[107] I. Yadroitsev, A. Gusarov, I. Yadroitsava, and I. Smurov, "Single track formation in selective laser melting of metal powders," *J. Mater. Process. Technol.*, vol. 210, no. 12, pp. 1624–1631, 2010.

[108] G. F. Vander Voort, "Metallography: Principles and Practice," ASM International, 1999, p. 509.

[109] "DTSA-II Jupiter," 2017. [Online]. Available: http://www.cstl.nist.gov/div837/837.02/epq/dtsa2/. [Accessed: 30-Mar-2017].

[110] J. I. Goldstein, D. E. Newbury, D. C. Joy, C. E. Lyman, P. Echlin, E. Lifshin, L. Sawyer, and J. R. Michael, "Scanning Electron Microscopy and X-Ray Microanalysis," 3rd ed., New York: Springer, 2003, p. 518.

[111] A. Ünal, D. D. Leon, T. B. Gurganus, and G. J. Hildeman, "Production of Aluminum and Aluminum-Alloy Powder," in *ASM Handbook Volume 7: Powder Metal Technologies and Applications*, and H. S. P.W. Lee, Y. Trudel, R. Iacocca, R.M. German, B.L. Ferguson, W.B. Eisen, K. Moyer, D. Madan, Ed. Metals Park, Ohio, 1998, pp. 148–159.

[112] S. P. Narra and J. Beuth, "Unpublished work." Carnegie Mellon University, 2015.

[113] Y. V Murty, "Electrical and Electronic Connectors: Materials and Technology," *Encycl. Mater. Sci. Technol. (Second Ed.*, pp. 2483–2494, 2001.

[114] N. Verma, P. C. Pistorius, R. J. Fruehan, M. Potter, M. Lind, and S. Story, "Transient Inclusion Evolution During Modification of Alumina Inclusions by Calcium in Liquid Steel : Part I . Background , Experimental Techniques and Analysis Methods," *Metall. Mater. Trans. B*, vol. 42, no. August, pp. 711–719, 2011.

[115] D. Tang and P. C. Pistorius, "Unpublished work." Carnegie Mellon University, 2014.

[116] B. P. Flannery, H. W. Deckman, W. Roberge, and K. L. D'Amico, "Three-Dimensional X-ray Microtomography," *Science (80-.).*, vol. 237, pp. 1439–1444, 1987.

[117] S. R. Stock, "X-ray microtomography of materials," *Int. Mater. Rev.*, vol. 44, no. 4, pp. 141–164, 1999.

[118] S. R. Stock, "Recent advances in X-ray microtomography applied to materials," *Int. Mater. Rev.*, vol. 53, no. 3, pp. 129–181, 2008.

[119] R. Cunningham, S. P. Narra, C. Montgomery, J. Beuth, and A. D. Rollett, "Synchrotron-Based X-Ray Microtomography Characterization of the Effect of Processing Variables on Porosity Formation in Laser Power-Bed Additive Manufacturing of Ti-6Al-4V," *Jom*, vol. 69, no. 3, pp. 2–7, 2017.

[120] R. Cunningham, S. P. Narra, T. Ozturk, J. Beuth, and A. D. Rollett, "Evaluating the Effect of Processing Parameters on Porosity in Electron Beam Melted Ti-6Al-4V via Synchrotron X-ray Microtomography," *JOM*, vol. 68, no. 3, pp. 765–771, 2016.

[121] S. Rao, R. Cunningham, R. Ozturk, and A. D. Rollett, "Measurement and Analysis of Porosity in Al-10Si-1Mg Components Additively Manufactured by Selective Laser Melting," *Mater. Perform. Charact.*, vol. 5, no. 5, pp. 701–716, 2016.

[122] D. Gürsoy, F. De Carlo, X. Xiao, and C. Jacobsen, "TomoPy: A framework for the analysis of synchrotron tomographic data," *J. Synchrotron Radiat.*, vol. 21, no. 5, pp. 1188–1193, 2014.

[123] S. M. Miresmaeili, S. G. Shabestari, and S. M. A. Boutorabi, "Effect of melt filtration on porosity formation in Sr-modified A356 aluminium alloy," *Int. J. Cast Met. Res.*, vol. 16, no. January, pp. 541–548, 2003.

[124] J. Campbell, "An overview of the effects of bifilms on the structure and properties of cast alloys," *Metall. Mater. Trans. B Process Metall. Mater. Process. Sci.*, vol. 37, no. 6, pp. 857–863, 2006.

[125] EOS GmbH – Electro Optical Systems, "Material data sheets Aluminium AlSi10Mg, MaragingSteel MS1, StainlessSteel GP1, StainlessSteel PH1." [Online]. Available: http://www.eos.info/material-m. [Accessed: 10-Mar-2016].

[126] K. C. Mills, *Recommended values of thermophysical properties for selected commercial alloys*. Woodhead Publishing, 2002.

[127] W. E. King, A. T. Anderson, R. M. Ferencz, N. E. Hodge, C. Kamath, S. A. Khairallah, and A. M. Rubenchik, "Laser powder bed fusion additive manufacturing of metals; physics, computational, and materials challenges," *Appl. Phys. Rev.*, vol. 2, no. 4, pp. 41304-1-41304–26, 2015.

[128] R. Rai, J. W. Elmer, T. a Palmer, and T. DebRoy, "Heat transfer and fluid flow during keyhole mode laser welding of tantalum, Ti–6Al–4V, 304L stainless steel and vanadium," *J. Phys. D. Appl. Phys.*, vol. 40, no. 18, pp. 5753–5766, 2007.

[129] A. V. Gusarov, I. Yadroitsev, P. Bertrand, and I. Smurov, "Model of Radiation and Heat Transfer in Laser-Powder Interaction Zone at Selective Laser Melting," *J. Heat Transfer*, vol. 131, no. 7, pp. 72101-1-72101–10, 2009.

[130] A. Masmoudi, R. Bolot, and C. Coddet, "Investigation of the laser–powder–atmosphere interaction zone during the selective laser melting process," *J. Mater. Process. Technol.*, vol. 225, pp. 122–132, 2015.

[131] J. P. Kruth, X. Wang, T. Laoui, and L. Froyen, “Lasers and materials in selective laser sintering,” *Assem. Autom.*, vol. 23, no. 4, pp. 357–371, 2003.

[132] S. A. Khairallah and A. Anderson, “Mesoscopic simulation model of selective laser melting of stainless steel powder,” *J. Mater. Process. Technol.*, vol. 214, no. 11, pp. 2627–2636, 2014.

[133] W. E. King, H. D. Barth, V. M. Castillo, G. F. Gallegos, J. W. Gibbs, D. E. Hahn, C. Kamath, and A. M. Rubenchik, “Observation of keyhole-mode laser melting in laser powder-bed fusion additive manufacturing,” *J. Mater. Process. Technol.*, vol. 214, no. 12, pp. 2915–2925, 2014.

[134] F. Verhaeghe, T. Craeghs, J. Heulens, and L. Pandelaers, “A pragmatic model for selective laser melting with evaporation,” *Acta Mater.*, vol. 57, no. 20, pp. 6006–6012, 2009.

[135] H. Zhao, D. R. White, and T. DebRoy, “Current issues and problems in laser welding of automotive aluminium alloys,” *Int. Mater. Rev.*, vol. 44, no. 6, pp. 238–266, 1999.

[136] C. Montgomery, J. Beuth, L. Sheridan, and N. Klingbeil, “Process Mapping of Inconel 625 in Laser Powder Bed Additive Manufacturing,” in *Solid Freeform Fabrication Symposium*, Austin, TX, 2015, pp. 1195–1204.

[137] H. Gong, D. Christiansen, J. Beuth, and J. J. Lewandowski, “Melt Pool Characterization for Selective Laser Melting of Ti-6Al-4V Pre-alloyed Powder,” in *Solid Freeform Fabrication Symposium*, Austin, TX, 2014, pp. 256–267.

[138] C. Kamath, B. El-Dasher, G. F. Gallegos, W. E. King, and A. Sisto, “Density of additively-manufactured, 316L SS parts using laser powder-bed fusion at powers up to 400 W,” *Int. J. Adv. Manuf. Technol.*, vol. 74, no. 1–4, pp. 65–78, 2014.

[139] S. Kou, “Heat Flow in Welding,” in *Welding Metallurgy*, 2nd ed., John Wiley & Sons, 2003, pp. 48–51.

[140] M. Tang, P. C. Pistorius, S. Narra, and J. Beuth, “Rapid Solidification : Selective Laser Melting of AlSi10Mg,” *JOM*, vol. 68, no. 3, pp. 960–966, 2016.

[141] E. Yasa, J. Deckers, and J.-P. Kruth, “The investigation of the influence of laser re-melting on density, surface quality and microstructure of selective laser melting parts,” *Rapid Prototyp. J.*, vol. 17, no. 5, pp. 312–327, 2011.

[142] D. Manfredi, F. Calignano, M. Krishnan, R. Canali, E. P. Ambrosio, S. Biamino, D. Ugues, M. Pavese, and P. Fino, “Additive Manufacturing of Al Alloys and Aluminium Matrix Composites (AMCs),” in *Light Metal Alloys Applications*, W. A. Monteiro, Ed. InTech, 2014, pp. 3–34.

[143] T. Debroy and S. A. David, “Physical processes in fusion welding,” *Rev. Mod. Phys.*, vol. 67, no. 1, pp. 85–112, 1995.

[144] H. Matyja, B. C. Giessen, and N. J. Grant, “The Effect of Cooling Rate on the Dendrite Spacing in Splat-cooled Aluminum Alloys,” *J. Inst. Met.*, vol. 96, pp. 30–32, 1968.

[145] R. E. Spear, “Dendrite Cell Size,” *AFS Trans.*, vol. 43, pp. 209–215, 1963.

[146] V. S. Zolotorevsky, N. A. Belov, and M. V. Glazoff, “Microstructure of Cast Aluminum Alloys,” in *Casting Aluminum Alloys*, Elsevier, 2010, pp. 154–155.

[147] A. M. Mullis, L. Farrell, R. F. Cochrane, and N. J. Adkins, “Estimation of cooling rates during close-coupled gas atomization using secondary dendrite arm spacing measurement,” *Metall. Mater. Trans. B*, vol. 44, no. 4, pp. 992–999, 2013.

[148] D. Dubé, R. Angers, and A. Adnot, “Cooling Rates of REP Al-4.5% Cu Particles,” *Powder Metall. Int.*, vol. 23, no. 1, pp. 22–25, 1991.

[149] R. M. German, “Microstructure Control in Powders,” in *Powder Metallurgy Science*, 2nd ed., Princeton, NJ: Metal Powder Industries Federation, 1984, p. 138.

[150] J. Beuth, J. Fox, J. Gockel, C. Montgomery, R. Yang, H. Qiao, E. Soylemez, P. Reeseewatt, A. Anvari, S. Narra, and N. Klingbeil, “Process Mapping for Qualification Across Multiple Direct Metal Additive Manufacturing Processes Jack,” in *Solid Freeform Fabrication Symposium*, Austin, TX, 2013, pp. 655–665.

[151] R. Trivedi, F. Jin, and I. E. Anderson, “Dynamical evolution of microstructure in finely atomized droplets of Al-Si alloys,” *Acta Mater.*, vol. 51, no. 2, pp. 289–300, 2003.

[152] G. R. Armstrong and H. Jones, “Effect of decreased section thickness on the formation, structure and properties of a chill-cast aluminium-silicon alloy,” in *Proc. Conf on Solidification and Casting of Metals*, Sheffield, England, 1979, pp. 454–459.

[153] H. A. H. Steent and A. Hellawell, “Structure and properties of aluminium-silicon eutectic alloys,” *Acta Metall.*, vol. 20, pp. 363–370, 1972.

[154] O. A. Atasoy, F. Yilmaz, and R. Elliott, “This paper contains coupled zone figure, as original resource,” *J. Cryst. Growth*, vol. 66, pp. 137–146, 1984.

[155] M. M. Makhlouf and H. V. Guthy, “The aluminum-silicon eutectic reaction: Mechanisms and crystallography,” *J. Light Met.*, vol. 1, no. 4, pp. 199–218, 2001.

[156] G. E. Lloyd, “Atomic number and crystallographic contrast images with the SEM : a review of backscattered electron techniques,” *Mineral. Mag.*, vol. 51, pp. 3–19, 1987.

[157] G. J. Davies and J. G. Garland, “Solidification Structures and Properties of Fusion Welds,” *Int. Mater. Rev.*, vol. 20, no. 1, pp. 83–108, 1975.

[158] N. T. Aboulkhair, I. Maskery, C. Tuck, I. Ashcroft, and N. M. Everitt, “On the formation of AlSi10Mg single tracks and layers in selective laser melting: Microstructure and nano-mechanical properties,” *J. Mater. Process. Technol.*, vol. 230, pp. 88–98, 2016.

[159] N. T. Aboulkhair, C. Tuck, I. Ashcroft, I. Maskery, and N. M. Everitt, “On the Precipitation Hardening of Selective Laser Melted AlSi10Mg,” *Metall. Mater. Trans. A Phys. Metall. Mater. Sci.*, vol. 46, no. 8, pp. 3337–3341, 2015.

[160] J. Wu, X. Q. Wang, W. Wang, M. M. Attallah, and M. H. Loretto, “Microstructure and strength of selectively laser melted AlSi10Mg,” *Acta Mater.*, vol. 117, pp. 311–320, 2016.

[161] K. Gokuldoss Prashanth, S. Scudino, and J. Eckert, “Tensile Properties of Al-12Si Fabricated via Selective Laser Melting (SLM) at Different Temperatures,” *Technologies*, vol. 4, no. 4, p. 38, 2016.

[162] ASTM Committee E04, “ASTM Standard E112-13: Standard Test Methods for Determining Average Grain Size.” ASTM International, 2013.

[163] ASTM Committee E28, “ASTM E646-16: Standard Test Method for Tensile Strain-Hardening Exponents (n-Values) of Metallic Sheet Materials,” vol. 3. ASTM International, pp. 1–8, 2000.

[164] M. Tang and P. C. Pistorius, “Anisotropic Mechanical Behavior of AlSi10Mg Parts Produced by Selective Laser Melting,” *JOM*, vol. 69, no. 3, 2017.

[165] M. Tang and P. C. Pistorius, “Oxide, porosity and fatigue performance of AlSi10Mg parts

produced by selective laser melting," *Int. J. Fatigue*, vol. 94, pp. 192–201, 2016.

[166] G. Purcek, O. Saray, and O. Kul, "Microstructural evolution and mechanical properties of severely deformed Al-12Si casting alloy by equal-channel angular extrusion," *Met. Mater. Int.*, vol. 16, no. 1, pp. 145–154, 2010.

[167] N. T. Aboulkhair, I. Maskery, C. Tuck, I. Ashcroft, and N. M. Everitt, "Improving the fatigue behaviour of a selectively laser melted aluminium alloy: Influence of heat treatment and surface quality," *Mater. Des.*, vol. 104, pp. 174–182, 2016.

[168] I. Rosenthal, A. Stern, and N. Frage, "Strain rate sensitivity and fracture mechanism of AlSi10Mg parts produced by Selective Laser Melting," *Mater. Sci. Eng. A*, vol. 682, no. June 2016, pp. 509–517, 2017.

[169] Y. Flom and R. J. Arsenault, "Deformation of SiC/Al Composites," *JOM*, no. 38, pp. 31–34, 1986.

[170] ASM Handbook Committee, *ASM Handbook, Volume 2: Properties and Selection: Nonferrous Alloys and Special-Purpose Materials*. ASM International, 1990.

[171] W. F. Gale and T. C. . Totemeier, Eds., *Smithells Metals Reference Book*, 8th ed. Elsevier Butterworth-Heinemann, 2004.

[172] A. J. Klinter, G. Mendoza-Suarez, and R. A. L. Drew, "Wetting of pure aluminum and selected alloys on polycrystalline alumina and sapphire," *Mater. Sci. Eng. A*, vol. 495, no. 1–2, pp. 147–152, 2008.

[173] E. Louvis, P. Fox, and C. J. Sutcliffe, "Selective laser melting of aluminium components," *J. Mater. Process. Technol.*, vol. 211, no. 2, pp. 275–284, 2011.

[174] H. Gong, K. Rafi, H. Gu, T. Starr, and B. Stucker, "Analysis of defect generation in Ti-6Al-4V parts made using powder bed fusion additive manufacturing processes," *Addit. Manuf.*, vol. 1, pp. 87–98, 2014.

[175] Q. Wang, "Microstructural Effects on the Tensile and Fracture Behavior of Aluminum Casting Alloys A356 / 357," *Metall. Mater. Trans. A*, vol. 34, no. December, pp. 2887–2899, 2003.

[176] K. Tanaka and S. Matsuoka, "A tentative explanation for two parameters, C and m, in Paris equation of fatigue crack growth," *Int. J. Fract.*, vol. 13, no. 5, pp. 563–583, 1977.

[177] J. P. Benson and D. V Edmonds, "Microstructural Effects on Fatigue at Intermediate and High Crack Growth Rates in a L o w Alloy Steel," *Mater. Sci. Eng.*, vol. 38, pp. 179–186, 1979.

[178] J. Z. Yi, Y. X. Gao, P. D. Lee, and T. C. Lindley, "Microstructure-based fatigue life prediction for cast A356-T6 aluminum-silicon alloys," *Metall. Mater. Trans. B Process Metall. Mater. Process. Sci.*, vol. 37, no. 2, pp. 301–311, 2006.

[179] M. Tang, P. C. Pistorius, and J. Beuth, "Prediction of lack-of-fusion porosity for powder bed fusion," *Addit. Manuf.*, vol. 14, pp. 39–48, 2017.

[180] H. Gu, H. Gong, D. Pal, K. Rafi, and B. Stucker, "Influences of Energy Density on Porosity and Microstructure of Selective Laser Melted 17- 4PH Stainless Steel," in *Solid Freeform Fabrication Symposium*, Austin, TX, 2013, pp. 474–489.

[181] T. Kimura and T. Nakamoto, "Microstructures and mechanical properties of A356 (AlSi7Mg0.3) aluminum alloy fabricated by selective laser melting," *Mater. Des.*, vol. 89, pp. 1294–1301, 2016.

[182] AWS A2 Committee, “AWS A3.0M/A3.0-2010: Standard Welding Terms and Definitions - Including Terms for Adhesive Bonding, Brazing, Soldering, Thermal Cutting, and Thermal Spraying,” *ASTM International*. American Welding Society, 2010.

[183] E. Jones, E. Oliphant, P. Peterson, and E. Al., “SciPy: Open Source Scientific Tools for Python,” 2001. [Online]. Available: http://www.scipy.org/. [Accessed: 10-Mar-2016].

[184] J. Romano, L. Ladani, J. Razmi, and M. Sadowski, “Temperature distribution and melt geometry in laser and electron-beam melting processes – A comparison among common materials,” *Addit. Manuf.*, vol. 8, pp. 1–11, 2015.

[185] M. Badrossamay, E. Yasa, J. VAN Vaerenbergh, and J. P. Kruth, “Improving Productivity Rate in SLM of Commercial Steel Powders,” in *RAPID 2009 Conference & Exposition*, no. TP09PUB17, Schaumburg, IL, USA: Society of Manufacturing Engineers, 2009, pp. 1–13.

[186] C. Qiu, C. Panwisawas, M. Ward, H. C. Basoalto, J. W. Brooks, and M. M. Attallah, “On the role of melt flow into the surface structure and porosity development during selective laser melting,” *Acta Mater.*, vol. 96, pp. 72–79, 2015.

[187] C. Qiu, N. J. E. Adkins, and M. M. Attallah, “Microstructure and tensile properties of selectively laser-melted and of HIPed laser-melted Ti-6Al-4V,” *Mater. Sci. Eng. A*, vol. 578, pp. 230–239, 2013.

[188] F. Calignano, “Design optimization of supports for overhanging structures in aluminum and titanium alloys by selective laser melting,” *Mater. Des.*, vol. 64, pp. 203–213, 2014.

[189] M. Dimter, R. Mayer, L. Hümmeler, R. Salzberger, J. Kotila, and T. Syvänen, “Method and device for manufacturing a three-dimensional object,” US 8034279 B2, 2011.

[190] K. Guan, Z. Wang, M. Gao, X. Li, and X. Zeng, “Effects of processing parameters on tensile properties of selective laser melted 304 stainless steel,” *Mater. Des.*, vol. 50, pp. 581–586, 2013.